NANOPARTICLE TRANSPORT VIA HOLOGRAPHIC PHOTOPOLYMERIZATION

BY

JOHN DAVID BUSBEE

DISSERTATION

Submitted in partial fulfillment of the requirements
for the degree of Doctor of Philosophy in Materials Science and Engineering
in the Graduate College of the
University of Illinois at Urbana-Champaign, 2009

Urbana, Illinois

Doctoral Committee:

Professor Paul Braun, Chair
Professor Pierre Wiltzius
Professor Kenneth Suslick
Associate Professor Moonsub Shim
Doctor Richard Vaia, Air Force Research Laboratory

ABSTRACT

This thesis studies methods of engineering the placement of nanoparticle with sub-micron resolution over macroscopic size scales. Such control holds great promise as an inexpensive methodology for manufacturing devices, such as optical elements, with enhanced functionality and properties. Specifically, we have examined the addition of silica nanoparticles into holographic photopolymerization systems for the purpose of controlling the location of the nanoparticle within the periodic structure based upon control of the surface chemistry of the nanoparticle.

Herein we report the successful sequestration of methacrylate functionalized, silica nanoparticles into the polymeric domain of phase separated, liquid crystal—acrylate composite structures with regular, submicron periodicities. TEM analysis of the resultant Bragg gratings indicated that the nanoparticles were fully dispersed within the polymer. Optical characterization of the grating structures indicated that the particles did not negatively impact the optical properties of the grating, and enhanced the switching properties of the liquid crystal structure due to the roughly lamellar morphology of the liquid crystal droplets when the nanoparticle are present in the formulation. The successful functionalization of the nanoparticle surface was confirmed using NMR analysis.

It was noted experimentally that at large, excess concentrations of the nanoparticle functionalization agent, a hybrid organic—siloxane corona was physisorbed onto the nanoparticle surface, imparting liquid-like properties to the nanoparticles without the presence of solvents. It was then demonstrated using

SAXS analysis that one could achieve FCC structures with these highly viscous liquids containing up to 60% inorganic content. Because the corona is polymerizable, the structure can then be fixed in place.

Excellent dispersion and isolation in the polymer domain was also demonstrated for high loadings (up to 20 wt%) of the same reactive silica nanoparticles in holographic syrups containing thiol-ene monomers. Because thiol-ene polymers have significant advantages over acrylates for these systems due to the step-growth polymerization mechanism, this system was chosen for further development as a method to create defined nanoparticle polymer hybrid structures. To guide future development efforts, real-time monitoring of grating development was conducted to increase knowledge of system variability. It was noted here that the addition of nanoparticles delays grating formation in a fashion linear with nanoparticle loading.

In order to help understand the mechanism by which nanoparticles delay grating formation, the step-growth, holographic process was modeled using a reaction diffusion system that treats component diffusion as following Stokes-Einstein driven by pure concentration gradients. Ignoring the thermodynamic interactions proved to be an inadequate assumption, so the model was re-accomplished using Flory-Huggins Polymer—Solution Theory to account for free energy using an experimentally derived χ between the polymer and liquid crystal and by assuming that the nanoparticle could be treated as a polymer with a radius of gyration equal the nanoparticle radius. This model qualitatively matched the

experimental observations and roughly predicted that the delay in grating formation was due to reactive incorporation of the nanoparticle into the polymer, which greatly slowed polymer diffusion. It was then speculated that this increased viscosity delayed phase separation, although phase separation was not treated directly with this model.

ACKNOWLEDGMENTS

As with any large undertaking, this was not just my effort, but that of many. There are many persons to thanks for their hard work, ideas, conversations, mentorship, suggestions, love and support.

First, I would like to thank the members of my committee, but especially my advisor, Professor Paul Braun, for their guidance and suggestions over the course of this process. I offer a special thanks to Paul for his encouragement and patience with my busy life. Professors Schweizer and Rogers contributed significantly to my understanding in the field of materials science. Professor Wiltzius has provided advice and encouragement over the course of many meetings. I would like to offer a special thanks to Abby Juhl for all of her support and ideas over the course of our shared projects over the last 4 years. Thanks, Abby for being a good partner and a good friend. I would also like to acknowledge the fruitful lab conversations held with Robert Shimmin and Dara Gough in the Braun Group.

I received a significant amount of support for this effort at Wright-Patterson AFB and I would above all like to thank Richard Vaia for his support and guidance. Thank you to Tim Bunning for the opportunity to do a significant amount of work in his labs and for his stimulating ideas about the way forward. I would like to offer special thanks as well to Lalguldi Natarajan and Vincent Tondiglia for their project support, ideas and friendship. Thanks, Nat, for your overall project guidance and specialized knowledge of liquid crystals and photochemistry. Vince, I couldn't have done this with out you. You are the glue that holds the lab together. Tim White

provided invaluable insight and advice into thiol-ene polymers and RTIR spectroscopy. Professor Allan Guymon at the University of Iowa allowed me to visit his labs and utilize his RTIR spectrometer. I owe him a debt of gratitude.

Thank you to Rachel Jakubiak for her advice on photochemistry. Peter Mirau offered a significant amount of work and a not insignificant amount of advice when it came to NMR efforts. Thanks, Peter! Thanks to Hilmar Koerner for his efforts an advice on SAXS experiments. I also gratefully appreciate the efforts of Folusho Oyerokun with has assistance on the mechanics of the modeling process and his wiliness to help at the odd hours that programming requires.

Of course, the work does not get done on a long project like this without the support of your friends and loved ones. Thanks to all of my friends at Illinois who helped support me during my travels. Brandon Howe and Amit Patel have made special efforts to keep up with me—their friendship is greatly appreciated. Of course, I would not currently be sane without the support of my family, especially the support of my Mother and Father, through their continued prayers, phone calls and encouragement. Thank you.

Above all, I want to thank my lovely wife, Michelle, and son, Travis, for the support and special sacrifices it took to get me through this process. It wasn't easy to live with a person who was commuting 500 miles a week. I definitely couldn't have done this without you. I love you, both!

TABLE OF CONTENTS

CHAPTER 1

INTRODUCTION

There have been multiple examples of the advantages of adding nanoparticles into polymeric systems *[1-6]*. These early examples begin to show the potential of hybrid materials with nanoscale constituents. Much of the perceived potential, however, cannot be realized without some level of control as to the dispersement and relative placement of the particles within the polymeric system *[7]*. In several instances of early incorporation of nanoscale particulates, agglomeration limited both the level of loading and the achieved physical properties of the hybrid system *[8]*. Because many of the length scales of a system's physical properties of interest are within the achievable length scales of many nanoparticulate systems, the ability to control the relative placement of near monodisperse nanoparticles with designed diameters within a structure can achieve unique properties. For example, the assembly of colloidal particles into regular, repeating structures can create materials with a specified optical band gap. For these designed hybrid structures to be adopted into practical devices, it will be necessary to develop techniques which can reliably and quickly create these structures in an economic fashion over macroscopic scales with reasonable defect densities *[9]*. The research presented in this thesis pursues background research necessary to pursue the development of efficacious techniques to solve some of these issues, along with understanding of the associated processing and handling tasks, and provides several proof-of-concept demonstrations.

Holographic methods have been chosen as the primary techniques for nanoparticle patterning in this thesis because they have the potential to meet all of the requirements for successful adoption of hybrid device manufacturing, such as the potential to disperse and sequester sub-micron scale nanoparticulates as device templates, as well as the potential for meeting more specific goals of improving performance or adding additional functionality to holographic polymer dispersed liquid crystal (HPDLC) optical devices *[9]*.

The remainder of this chapter provides an introduction to the holographic techniques used to create HPDLCs, surveys the relevant prior research in the area and covers other background topics germane to understanding the research presented in the following chapters.

1.1 Holographic Polymer Dispersed Liquid Crystals

Holographic polymer dispersed liquid crystals are phase separated structures of polymer and liquid crystal. The structures are formed by polymerizing the monomer via exposure to a holographic interference pattern until phase separation occurs, leading to a periodic structure with features derived from the interference pattern. Given an adequate number of interfering beams and positions, any arbitrary holographic pattern can be created, opening the door to complex, engineered optical structures *[10]*. The orientation and order of the liquid crystal domains can be modulated via electromagnetic fields, yielding structures whose optical properties are switchable. Because of the many potential useful devices that

can be created using HPDLCs, there has been a significant body of research in the field over the last 15 years *[11-22]*.

When exposed to a periodic interference pattern created by the holographic system, the polymerization is initiated at a rate that is correlated to the intensity of the laser light in the interference pattern. Considering the exposure of the holographic syrup to a simple sinusoidal variation in intensity from the interference of two monochromatic light beams, one would expect significant initiation in the peak regions (high light intensity) and very little in the valleys (low light intensity regions). This leads to a monomer concentration gradient as monomer is consumed much more rapidly in the peak regions than in the valley regions. This gradient leads to diffusion of the monomers from the low intensity regions towards the high intensity region and a corresponding counter-diffusion of the polar liquid crystal molecules from the high intensity regions to the low intensity regions. When it is energetically favorable, phase separation occurs, yielding, from a simplistic perspective, periodic stripes of polymer-rich regions and liquid crystal regions *[19]*.

While interference patterns can be designed to an arbitrary degree of complexity, as mentioned previously, most of the body of research has centered on simple geometries, such as 2-beam interference patterns to create a stripe periodicity such as found in either reflection or transmission gratings. A typical experiment is configured with the holographic syrup confined between two glass plates at a defined separation distance. Manufacturing a cell with a defined gap and subsequently using capillarity to fill with the holographic liquid, or by adding glass spacers of defined diameter to the holographic liquid prior to sandwiching between

two glass plates and sealing with epoxy, can control this distance *[14]*. All experiments presented in this dissertation conform to the latter process. A typical 2-beam holographic setup is presented in Figure 1.1. In both cases, a spatial filter is used on each beam to remove high frequency aberrations from the beam to ensure as uniform of beam-front as possible. As can be seen in the figure, in the case of a transmission grating, both beams enter the front of the cell with the periodicity of the beam varying inversely proportional to the included angle between the beams, with the periodic structure oriented perpendicular

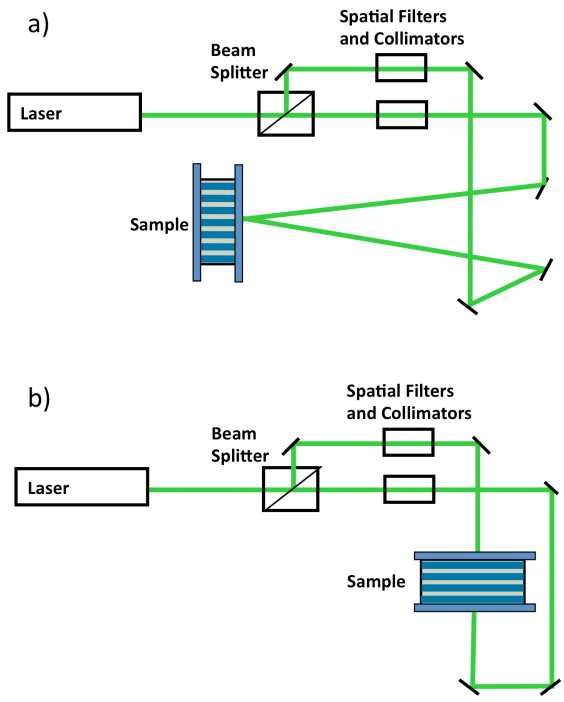

Figure 1.1 Schematic representation of holographic setup for creating a) Bragg transmission gratings and b) Bragg reflection gratings

to the glass plates with a typical period from 1-5 microns. In the case of a reflection grating, laser beams enter the front and rear glass plates to create a periodicity whose planes are parallel to the glass, with a normal orientation producing the smallest possible pitch. Typical pitches for the reflection geometry vary from approximately 100 to 350 nm.

Because the liquid crystal phase separates from the polymer to separate domains with regular alternating spacing, the two materials creates a regular refractive index difference, Δn, which forms an optical grating in the Bragg regime. The liquid crystal can be chosen so that the index of refraction of the ordinary axis closely matches that of the polymer system, so that when the liquid crystal is aligned, the differences in the index of refraction along the light propagation axis are effectively removed, thus turning "off" the grating. A schematic for an electrically switched HPDLC reflection grating is shown in Figure 1.2. As can be seen in the figure, for a fully formed acrylate HPDLC reflection grating, the liquid crystal is typically disordered without the presence of an electrical or magnetic field, with an average index of refraction, n_{ave}, of 1.64. When contrasted with the polymer index, we can see that the Δn of the system is approximately 0.03. For HPDLC systems, the liquid crystal can be aligned using either a magnetic or electrical field, but the magnetic field necessary to induce alignment is large, making electrical switching the preferred technique in typical situations *[10]*.

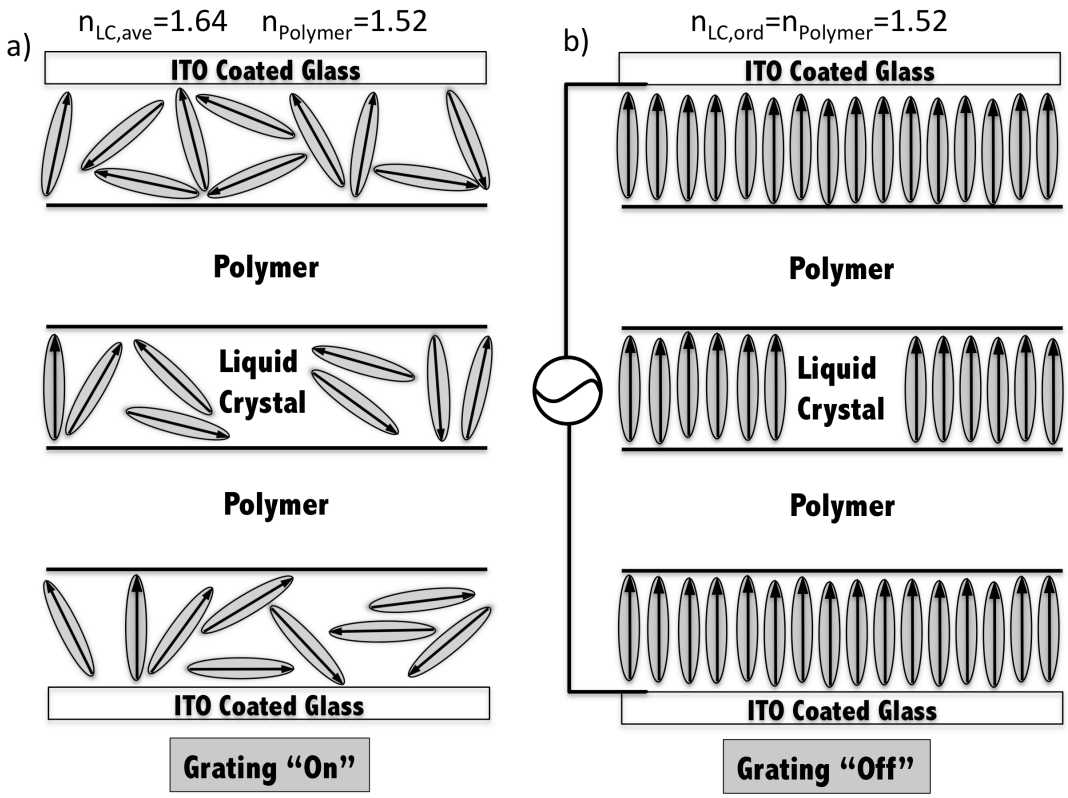

Figure 1.2 Schematic of a HPDLC Bragg reflection grating sandwiched between optically clear conducting electrodes. a) Grating without an applied electrical field has randomly ordered liquid crystal and a corresponding Δn. b) Grating with sufficient applied voltage field will align the liquid crystals along the propagation axis, removing Δn.

As seen in Figure 1.2, a voltage is applied to transparent electrodes, typically indium tin oxide (ITO), across the cell. This creates an electric potential across the cell with field lines perpendicular to the glass that will align the liquid crystal to a nematic phase, given sufficient field strength. The voltage necessary to cause alignment varies based on liquid crystal droplet morphology, droplet size, HPDLC chemistry and grating pitch, but a typical acrylate reflection grating has been found to switch at field strengths of ~ 20 to 30 volts per micron of spacing across the cell.

When aligned with the electric field, the index of refraction of the liquid crystal with respect to the propagation of light through the cell (normal direction), n_o is approximately equal to 1.52, thus removing the periodic Δn and effectively switching the grating from "on" to "off."

1.1.1 Acrylate HPDLC Systems

A significant portion of the early research conducted on HPDLC's has used an acrylate polymeric system with an acetylated, decarboxylated Rose Bengal derivative (RBAX, $C_{21}H_6Cl_4I_4O_4$) as the photo-initiator.

This system was first used by Sutherland for Bragg gratings via HPDLC *[14]*, although RBAX was developed as a Rose Bengal alternative that was more soluble in non-polar solvents by Neckers in 1992 *[23]*. A typical recipe for this chemical system is given in Table 1.1. Research has shown that an excited triplet state of RBAX undergoes an electron transfer reaction in which N-phenyl glycine (NPG) acts as an electron donor, yielding an NPG radical, which initiates the free-radical polymerization process *[23]*. The absorption spectrum of RBAX is quite broad in the visible and can be initiated with laser lines from 488 to 532 nm. Acrylate HPDLC systems also frequently utilize a UV laser in conjunction with Darocur 4265, which is a mixture of 2,4,6-Trimethylbenzoyl-diphenyl-phosphineoxide and 2-Hydroxy-2-methyl-1-phenyll-propan-1-one, as the free-radical initiator in place of RBAX and NPG.

Table 1.1 Typical Formulation of HPDLC mixture with acrylates using green light for holographic exposure

Chemical	**Weight %**	**Function**
EMD E7	32	Liquid Crystal
Rose Bengal derivative, RBAX	.5	Photo-Initiator
N-phenylglycine (NPG)	2.5	Co-Initiator
N-vinyl pyrrolidinone (NVP)	10	Solublizer, Chain Extender
Octanoic acid	5	Surfactant
Dipentaerythritol penta/hexa acrylate	50	Monomer

Looking more closely, because the polymerization of the acrylate system is based on a free radical, addition reaction, the molecular weight of the polymer in the high intensity region builds rapidly. Additionally, the typical monomer used in acrylate HPDLC systems is multifunctional, leading to a cross-linked system. The result of these two facts is that the system reaches the gelation point very early in the conversion process, with the typical result being that gelation occurs either before or simultaneously with phase separation *[15]*. This leads to a large amount of trapped liquid crystal in the polymeric regions that can only continue to separate via liquid-gel demixing, leading to slowed diffusion and a significant amount of liquid crystal remaining trapped in the final grating due to kinetic considerations *[24]*. As the liquid crystal droplets continue to expand as the liquid-gel de-mixing progresses, the high degree of cross-linking in the acrylate polymer yields

anisotropic stresses that mechanically deform the droplets, resulting in a morphology that while periodic, has irregularly shaped liquid crystal regions. Because of characteristic volume differences between monomers and polymers, corresponding shrinkage causes the pitch of the periodic structures to be reduced from that of the interference pattern by 2-3%, typically *[15]*. Change in processing conditions and syrup composition can also yield different levels of liquid crystal phase separation, with the amount of liquid crystal trapped in the polymeric domain varying from values of 30% to 60% *[24]*. A typical morphology of a Bragg reflection grating with the acrylate chemistry specified in Table 1.1 and created by 2-beam interference is shown in Figure 1.3

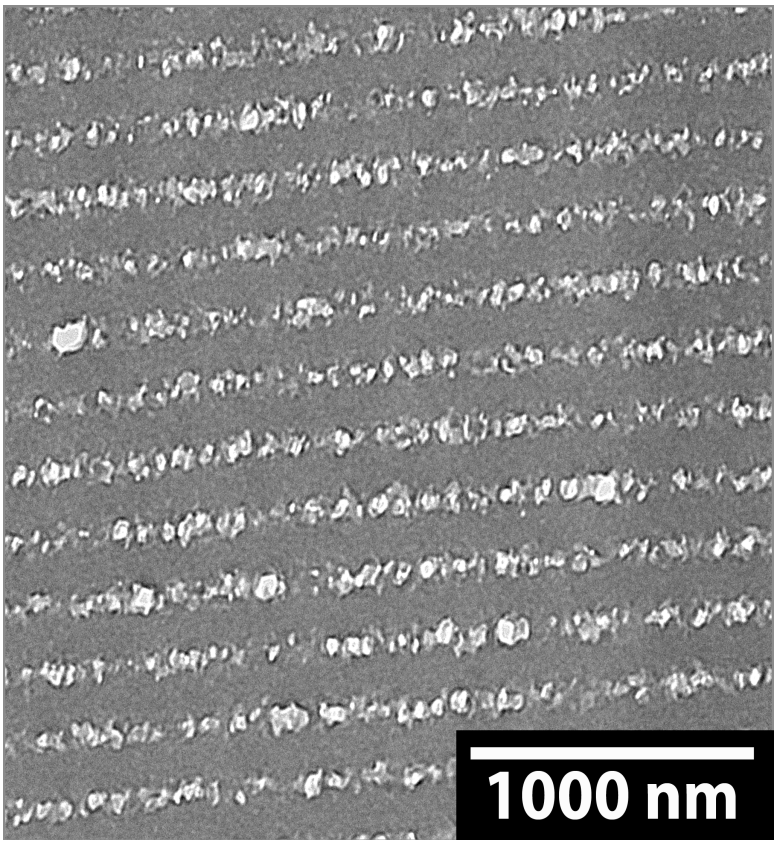

Figure 1.3 TEM micrograph of an 75nm microtomed cross-section of an HPDLC reflection grating created with a syrup whose formulation is given Table 1.1.

1.1.2 Thiol-ene Based Holographic Polymer Dispersed Liquid Crystals

Acrylate-based HPDLC systems have several perceived deficiencies *[20]*. Gelation at relatively low percent monomer conversion leads to low levels of liquid crystal phase separation. The resulting high viscosities yield kinetic hindrances to monomer transport leading to incomplete polymerization. Residual monomer leads to poor grating stability as the monomer slowly diffuses and polymerizes. Acrylate systems have a high level of cure shrinkage after gelation, causing mechanical stresses within the grating that lead to anisotropic, irregular-shaped polymer

droplets with correspondingly large switching voltages. Over the past several years there has been considerable research conducted into polymer systems that can rectify many of these shortcomings. One of the most prominently studied class of replacement systems are polymers based upon the thiol-ene reaction *[25]*.

Thiol-ene systems have several potential advantages. The initiation mechanism for polymerization remains a free-radical reaction, but the propagation mechanism, instead of an addition reaction as for acrylates, is a step-growth, condensation reaction. Because the molecular weight evolution is much slower for condensation reactions than for addition reactions, gelation occurs at a much higher percent monomer conversion. This delayed gelation point allows the primary de-mixing mechanism to be liquid-liquid, which leads to round liquid crystal droplets upon macroscopic phase separation. Additionally, because much more of the polymer is formed before the matrix is fully formed (before gelation), stress buildup due to cure shrinkage is greatly reduced *[15]*.

There are many different thiol molecules with varying functionalities that are use in thiol-ene polymerizations. Similarly, many molecules with varying functionality are used as the "-ene" in the reaction *[26]*. Common molecules and their structures are shown in Figure 1.4

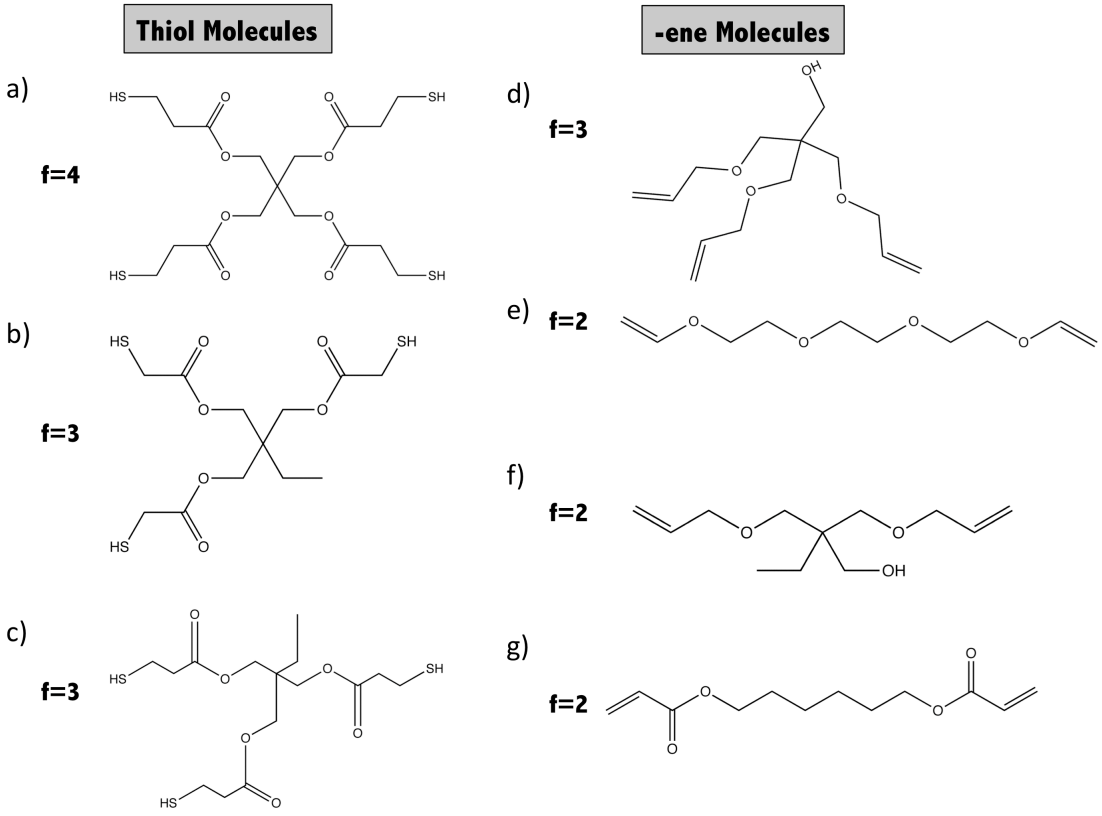

Figure 1.4 Molecular structures of common monomers used for the thiol-ene reaction. a) Pentylerythritol tetrakis(3-mercaptopropionate), b) Trimethylolpropane tris(2-mercaptoacetate), c) Trimethylolpropane tris(mercaptoproprionate), d) Pentaerythritol trivinyl ether, e) Triethylene divinyl ether, f) trimethylolpropane diallyl ether, and g) hexadecyl diacrylate.

Much of the research into thiol-ene polymers for holographic polymer dispersed liquid crystals has utilized a commercial formulation, Norland Optical Adhesive No. 65 *[27, 28]*. The exact composition of the formulation is proprietary, but is reported to contain a tetra-functional thiol molecule and a tri-functional allyl ether as the "–ene" molecule, along with an unknown weak UV photo-initiator and stabilizer *[25]*. While it is generally preferable not to use unknown commercial formulations as the basis for research, NOA 65 is used as the primary material for

thiol-ene research in this thesis, because a) there is a large body of experimental data as the basis for comparison, and b) while thiol-ene formulations, in general, are not very stable, the proprietary stabilizer used in this formulation has proven to be extremely so over the course of this research.

When compared to similar acrylate based systems, HPDLC gratings created with NOA 65 have been found not to exhibit any significant levels of voltage creep, since monomer conversion levels can be driven to close to 100%. Additionally, grating index contrast is better due to the slightly higher index of refraction of NOA 65, allowing similar diffraction efficiencies (DE) to be obtained with fewer layers and thus thinner overall films. Figure 1.5 shows the morphology of a typical thiol-ene based, Bragg reflection grating

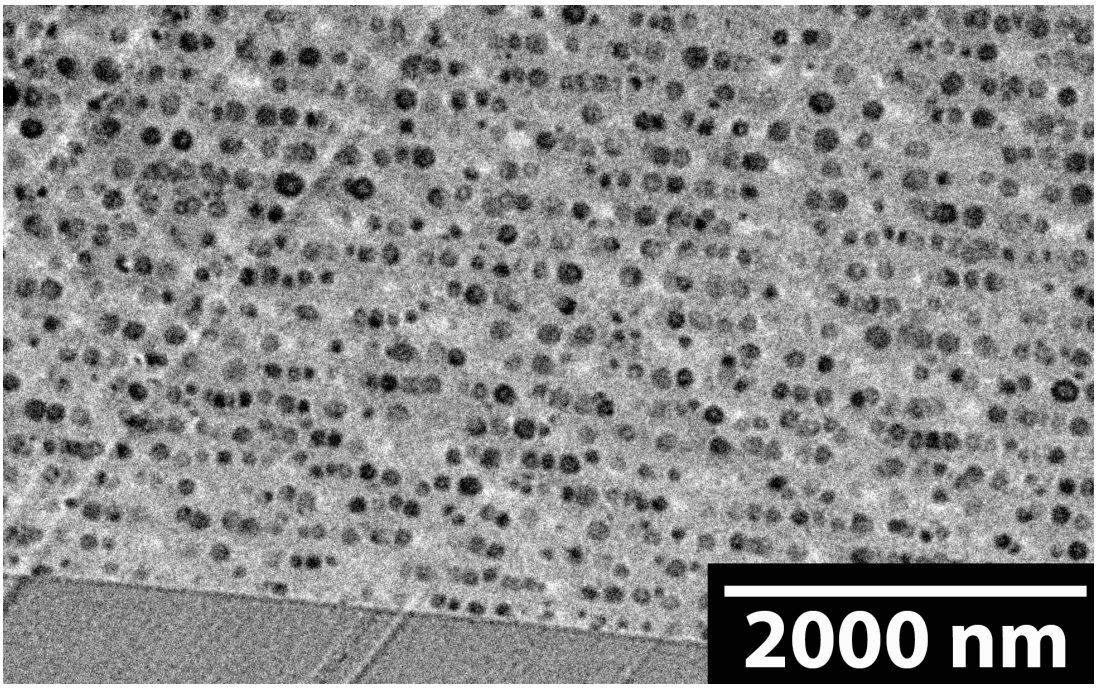

Figure 1.5 TEM Micrograph of a thiol-ene Bragg reflection grating created using NOA 65 as the monomer mixture, Darocur 4265 as the photo-initiator and EMD BL-038 as the liquid crystal.

1.2 Silica Nanoparticle Synthesis and Functionalization

Silica nanoparticles were chosen for this investigation for a number of reasons. First, the synthesis method is fairly uncomplicated and easy to accomplish. Silica nanoparticles were among the first nanoparticles to be mass-manufactured and have been well characterized *[29]*. They can be synthesized in a variety of different sizes while achieving a narrow polydispersity that approaches unity *[30]*. Additionally, because of the electronics semiconductor industry, silicon chemistry has been exhaustively studied, thus easing the task of functionalizing the nanoparticles for compatibility with different mediums *[31]*. For the purposes of HPDLC films, the nanoparticle index of refraction is sufficiently similar to the polymer and liquid crystals such that the index contrast at high loadings can be enhanced without losing the ability of the structure to completely switch states (index matched).

For this study, silica nanoparticles are synthesized using a modified Stöber reaction. In this reaction, as shown in Figure 1.6, tetraethoxysilane (TEOS) is hydrolyzed by the presence of water and then condensed to form a siloxane. Under appropriate pH conditions (in this case basic), during the condensation reaction, the charge stabilization of the siloxane molecules hinders aggregation or gelation, thus promoting solid nanoparticle formation *[32]*. At small sizes, these particles are irregular, roughly shaped spheroids. While exact growth mechanisms are complex and dependent on factors such as relative reactant concentrations, pH, and

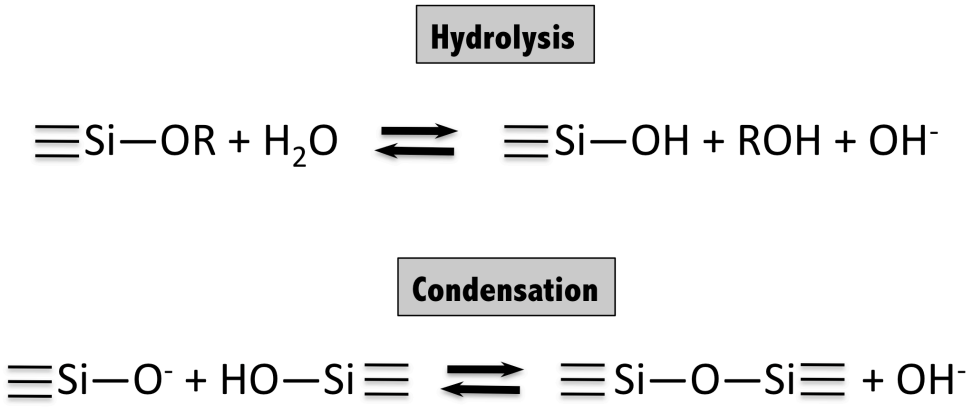

Figure 1.6 General hydrolysis and condensation reaction equations for the formation of silica nanoparticles from multi-functional silicon alkoxides

temperature, it is generally believed that for larger particles, growth mechanisms are a combination of nucleation, followed by aggregation, then by pure molecular addition as particle concentration falls below critical values *[33]*.

For the investigations presented herein, smaller particles are desired to avoid deleterious light scattering and to maximize diffusive transport, so particles with average diameters of 20-30 nm were typically used. Silica nanoparticles (28 nm diameter) were synthesized in ethanol using a modified Stöber recipe, with each constituent and its associated quantity given in Table 1.2 *[30]*.

Table 1.2 Modified Stöber synthesis recipe for silica nanoparticles with a diameter of 28 nm.

Chemical	Volume
Tetraethoxysilane	3 mL
Ammonium Hydroxide (28%)	3 mL
Water, distilled, de-ionized	1.5 mL
Ethanol, 200 Proof	120 mL

All chemicals used during nanoparticle synthesis were used as received. Synthesis procedures are as follows: Using the volumes specified in Table 1.2, add into a 250 ml flask both the de-ionized water and the 28% ammonium hydroxide solution, along with the absolute ethanol and stir vigorously for 30 minutes at room temperature using a magnetic stir bar. Tetraethoxysilane (TEOS, Geleste) is then added via pipette as quickly as possible. The resultant solution is then purged with dry nitrogen and stirred for 12 hours. Figure 1.7 illustrates typical results of this recipe via the TEM micrograph of a drop of the nanoparticle containing ethanol dried onto a holey carbon grid.

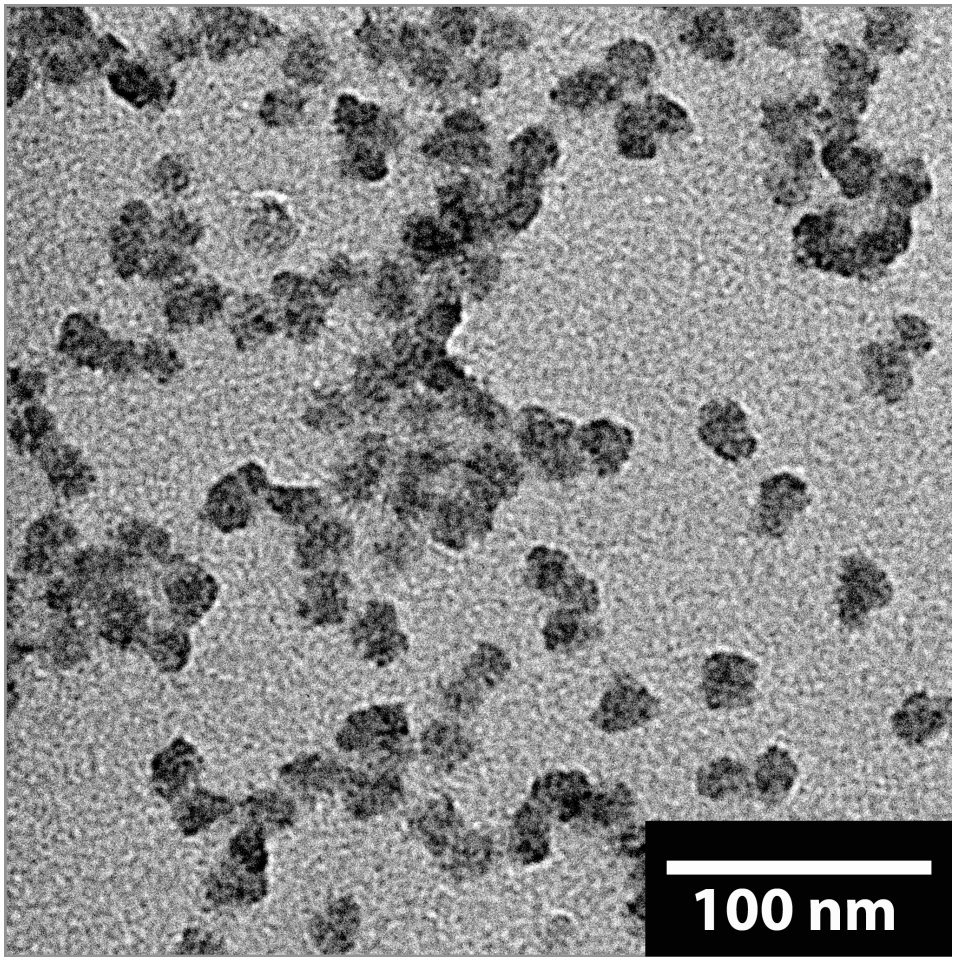

Figure 1.7 TEM micrograph of silica nanoparticles produced using the modified Stöber recipe given in Table 1.2.

Other synthesis methods, such as the micro-emulsion procedure detailed in *[34]*, produce more monodisperse particles that are much closer to perfect spheres. Particles of 50 nm diameter synthesized using this micro-emulsion method were utilized in early investigations. However, it was found that nanoparticles made using micro-emulsion methodologies were difficult to adequately functionalize—most likely due to steric hinderances from residual surfactant from the emulsion remaining adsorbed on the particle surface.

In order to achieve the primary goals of this thesis, it is necessary to be able to successfully functionalize the particles to ensure compatibility with various polymeric mediums. The schema followed uses common silane coupling agents as the basis for functionalization, as illustrated in Figure 1.8. Covalent bonding of the functionalizing agent insures a robust linkage that is not easily removed as the nanoparticles are transferred from solvent to polymeric mediums.

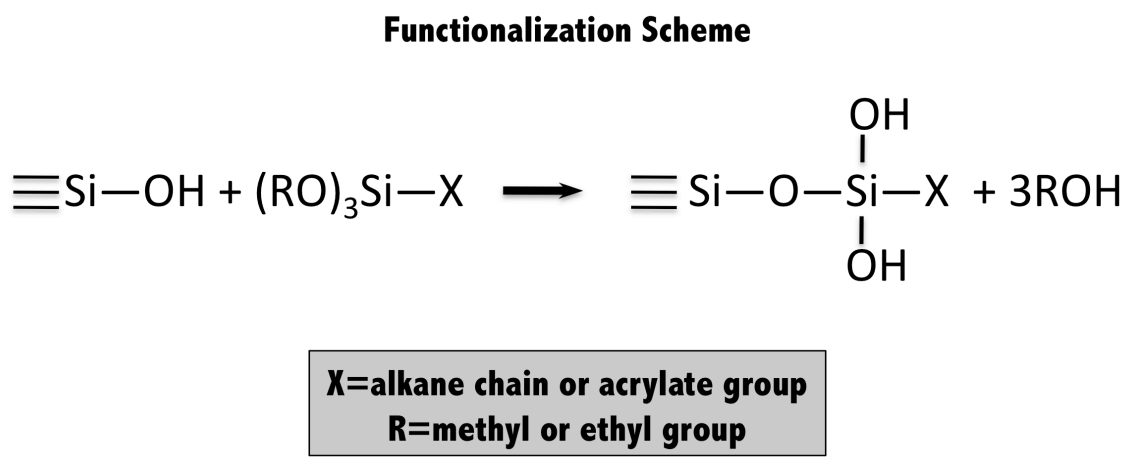

Figure 1.8 General scheme used for functionalizing silica nanoparticles for research presented herein.

1.3 Thesis Structure

The remainder of the research presented in this dissertation is organized as follows. Chapter 2 presents efforts to add silica particles in a controlled fashion into acrylate HPDLC systems. It covers the effect of surface functionalization upon dispersion and particle sequestration into a specified domain within the periodic structure. Chapter 3 expands the HPDLC work into the thiol-ene system and

explores the effects of functionalized silica nanoparticles upon the reaction kinetics during grating formation. Chapter 4 explores the ability to take advantage of the excellent dispersion of methacrylate-functionalized nanoparticles to create nanocomposites with high loadings of dispersed nanoparticles. Chapter 5 further explores the kinetics of the thiol-ene system in HPDLC systems by creating a simple model to capture relevant processing parameter in the hopes of guiding experimental research to maximized the transport of nanoparticles in the system. Chapter 6 provides a synopsis of the topics covered in this dissertation and summarizes relevant results with indications of what the natural research progression might be to continue to advance the state-of-the-art in these areas.

1.4 References

[1] S. Dash, S. Mishra, S. Patel, B. K. Mishra, *Advances in Colloid and Interface Science* **2008**, *140*, 77.

[2] S. M. Ilett, A. Orrock, W. C. K. Poon, P. N. Pusey, *Physical Review E* **1995**, *51*, 1344.

[3] G. Oshanin, M. Moreau, S. Burlatsky, *Advances in Colloid and Interface Science* **1994**, *49*, 1.

[4] T. Y. Lee, C. N. Bowman, *Polymer* **2006**, *47*, 6057.

[5] M. J. E. C. S·nchez, C. van†Heesch, C.†W.†M. Bastiaansen, D.†J. Broer, J. Loos, R. Nussbaumer,, *Advanced Functional Materials* **2005**, *15*, 1623.

[6] L. M. Goldenberg, O. V. Sakhno, T. N. Smirnova, P. Helliwell, V. Chechik, J. Stumpe, *Chemistry of Materials* **2008**, *20*, 4619.

[7] C. L. D. R. A. Vaia, L. V. Natarajan, V. P. Tondiglia, D. W. Tomlin, T. J. Bunning,, *Advanced Materials* **2001**, *13*, 1570.

[8] F. Hou, W. Wang, H. Guo, *Applied Surface Science* **2006**, *252*, 3812.

[9] R. Jakubiak, D. P. Brown, F. Vatansever, V. P. Tondiglia, L. V. Natarajan, D. W. Tomlin, T. J. Bunning, R. A. Vaia, "Holographic photopolymerization for fabrication of electrically switchable inorganic-organic hybrid photonic structures", presented at *Organic Photonic Materials and Devices V*, San Jose, CA, USA, **2003**.

[10] J. W. Rinne, P. Witzius, *Opt. Express* **2006**, *14*.

[11] T. J. White, L. V. Natarajan, V. P. Tondiglia, P. F. Lloyd, T. J. Bunning, C. A. Guymon, *Polymer* **2007**, *48*, 5979.

[12] A. Urbas, V. Tondiglia, L. Natarajan, R. Sutherland, H. Yu, J.-H. Li, T. Bunning, *Journal of the American Chemical Society* **2004**, *126*, 13580.
[13] V. P. Tondiglia, R. L. Sutherland, L. V. Natarajan, P. F. Lloyd, T. J. Bunning, *Opt. Lett.* **2008**, *33*, 1890.
[14] R. L. Sutherland, L. V. Natarajan, V. P. Tondiglia, T. J. Bunning, *Chemistry of Materials* **1993**, *5*, 1533.
[15] L. V. Natarajan, C. K. Shepherd, D. M. Brandelik, R. L. Sutherland, S. Chandra, V. P. Tondiglia, D. Tomlin, T. J. Bunning, *Chemistry of Materials* **2003**, *15*, 2477.
[16] L. Natarajan, J. Klosterman, V. P. Tondiglia, R. L. Sutherland, P. F. Lloyd, T. J. Bunning, "Effect of adding a multifunctional acrylate on the electro-optical properties of reflection gratings formed by thiol-ene photopolymerization", presented at *Optical Materials in Defence Systems Technology*, London, United Kingdom, **2004**.
[17] J. Klosterman, L. V. Natarajan, V. P. Tondiglia, R. L. Sutherland, T. J. White, C. A. Guymon, T. J. Bunning, *Polymer* **2004**, *45*, 7213.
[18] R. S. Justice, D. W. Schaefer, R. A. Vaia, D. W. Tomlin, T. J. Bunning, *Polymer* **2005**, *46*, 4465.
[19] J. D. Busbee, A. T. Juhl, L. V. Natarajan, V. P. Tondiglia, T. J. Bunning, R. A. Vaia, P. V. Braun, *Advanced Materials* **2009**, *21*, 3659.
[20] T. J. Bunning, L. Natarajan, V. P. Tondiglia, R. L. Sutherland, "Effect of gel-point versus conversion on the real-time dynamics of holographic polymer-dispersed liquid crystal (HPDLC) formation", USA, **2003**.
[21] R. Caputo, L. De Sio, A. Veltri, C. Umeton, A. V. Sukhov, *Opt. Lett.* **2004**, *29*, 1261.
[22] C. C. Bowley, G. P. Crawford, *Applied Physics Letters* **2000**, *76*, 2235.
[23] Y. Bi, D. C. Neckers, (Ed: O. o. N. Research), Washington, D.C. **1994**.
[24] R. T. Pogue, R. L. Sutherland, M. G. Schmitt, L. V. Natarajan, S. A. Siwecki, V. P. Tondiglia, T. J. Bunning, *Applied Spectroscopy* **2000**, *54*, 12A.
[25] T. J. White, L. V. Natarajan, V. P. Tondiglia, T. J. Bunning, C. A. Guymon, *Macromolecules* **2007**, *40*, 1112.
[26] T. J. White, L. V. Natarajan, V. P. Tondiglia, P. F. Lloyd, T. J. Bunning, C. A. Guymon, *Macromolecules* **2007**, *40*, 1121.
[27] R. Bhargava, S.-Q. Wang, J. L. Koenig, *Macromolecules* **1999**, *32*, 8982.
[28] N. A. Vaz, G. W. Smith, G. P. Montgomery, *Molecular Crystals and Liquid Crystals* **1987**, *146*, 1.
[29] R. K. Iler, *United States Patent 2,974,105*, **1961**.
[30] A. Van Blaaderen, J. Van Geest, A. Vrij, *Journal of Colloid and Interface Science* **1992**, *154*, 481.
[31] M. Yamaguchi, Y. Nakamura, T. Iida, *Polymers and Polymer Composites* **1998**, *6*, 85.
[32] C. J. Brinker, G. W. Scherer, *Sol-Gel Science: The Physics and Chemistry of Sol-Gel Processing*, Academic Press, Inc., San Diego **1990**.
[33] H. Okudera, A. Hozumi, *Thin Solid Films* **2003**, *434*, 62.
[34] X. Zhao, R. P. Bagwe, W. Tan, *Advanced Materials* **2004**, *16*, 173.

CHAPTER 2

SIO_2 NANOPARTICLE SEQUESTRATION VIA REACTIVE FUNCTIONALIZATION IN HOLOGRAPHIC POLYMER DISPERSED LIQUID CRYSTALS

Published as: Busbee ,John D.; Juhl, Abigail T.; Natarajan, Lalguldi V.; Tongdilia, Vincent P.; Bunning, Timothy J.; Vaia Richard A.; Braun, Paul V. SiO_2 Nanoparticle Sequestration via Reactive Functionalization in Holographic Polymer-Dispersed Liquid Crystals, Adv. Mater. **2009**, 21, 3659–3662

2.1 Introduction

Holographic polymer dispersed liquid crystals (HPDLCs) have great promise for the facile fabrication of large area electrically responsive optical elements *[1-3]*. Through careful selection and design of the components, the liquid crystal, monomer, initiator, and other organic additives, the switching speed and other optical properties can be optimized for a given application. There are a number of limitations however to an all-organic system. For example, the refractive index contrast between a typical liquid crystal and the polymer constituents of a PDLC is generally small *[4]*. To circumvent this difficulty, it may be desirable to add inorganic materials, which can span a much larger range of refractive indices to tailor the periodic refractive index profile. One of the simplest methodologies of introducing an inorganic material into the HPDLC system is through the controlled addition of nanoparticles. Nanoparticles of many materials can be synthesized in sizes small enough to avoid the addition of deleterious light scattering, and numerous surface functionalization techniques are available to control the chemical interaction of the nanoparticles with the HPDLC system. Previous research has

demonstrated that under holographic exposure of liquid crystal free systems containing monomers and very low volume fractions of nanoparticles, the nanoparticles tend to counter-diffuse away from the polymerizing regions, and are sequestered into the low intensity regions. This has been demonstrated for Au, ZnO, SiO_2, and TiO_2 nanoparticles *[5-8]*. In the case of oxide particles, sequestration in this domain is consistent with the presence of charged surface hydroxyls causing the particles to be organophobic. However, for holographic photopolymerization to be of use as a generic manufacturing technique for holographic optical elements (as well as other uses), it is necessary to be able to select and control where within the periodic structure that the majority of the nanoparticles will reside. In particular, for optical applications, it is important that the nanoparticles not be sequestered into the liquid crystal phase, as they generally negatively impact the switching behavior. Here we demonstrate the incorporation of high volume fractions of chemically functionalized silica nanoparticles into electrically switchable HPDLCs with sub-micron lattice constants, and show the importance of the nature of the chemical functionalization. SiO_2 nanoparticles were selected primarily as a model system. Because the refractive index and low frequency dielectric constant of silica is similar to the polymer matrix we do not expect dramatic changes in switching behavior or optical properties due to the fundamental optical constants of the nanoparticles; we do, however, find they change the phase separation behavior and morphology of the phase separated droplets, which does have a strong effect on the optical behavior. The general approach utilized here is illustrated schematically in Figure 2.1.

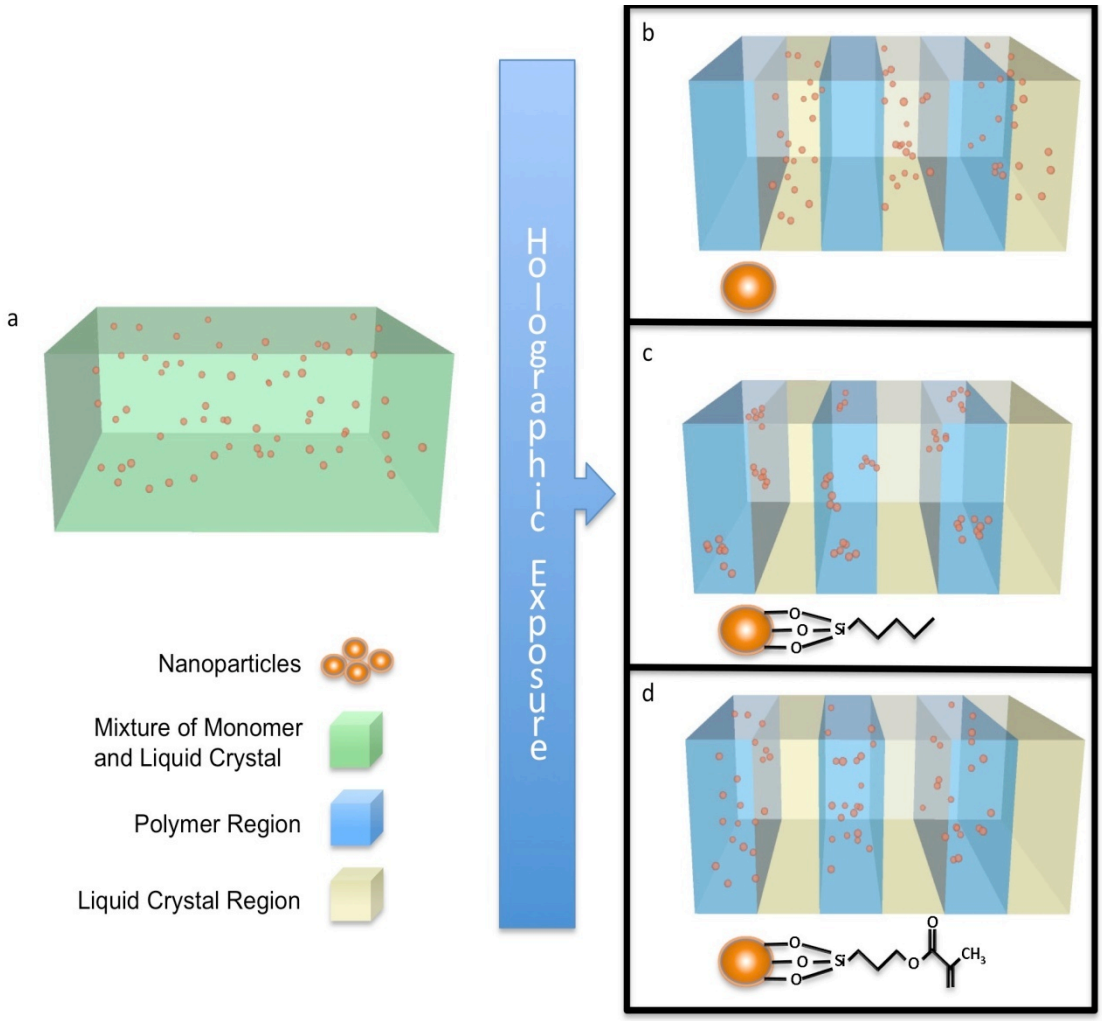

Figure 2.1. Schematic representation of the holographic sequestration of SiO_2 nanoparticles within a HPDLC system. a) Starting mixture of nanoparticles, monomer and liquid crystal (minor components not shown). b) Bare silica nanoparticles sequester into the liquid crystal phase. c) Hydrophobic PTES functionalized nanoparticles aggregate and generally reside in the polymer region. d) Reactive MPTMS functionalized nanoparticles disperse uniformly in the polymer region.

When unfunctionalized silica is added to a holographic system, it is expected the particles, in a manner analogous to the previous works *[5-8]*, will counter-diffuse away from the polymerizing regions. As represented in Figure 2.1b, upon

macroscopic phase separation of the liquid crystal and polymer, the particles will co-reside with the liquid crystal in the low intensity regions of the holographic pattern. In Figure 2.1c, the nanoparticles are functionalized with pentyltriethoxysilane (PTES). The presence of the alkyl chains renders the nanoparticles hydrophobic, which should result in the particles being sequestered within the polymeric domain. However, we observe that the particles aggregate, probably because nanoparticle-polymer interactions are unfavorable with respect to polymer-polymer interactions. The entropy of mixing of polymeric and nanoparticle systems is generally quite small, and thus even small unfavorable polymer-nanoparticle interactions can lead to nanoparticle aggregation into structures large enough to scatter light. In Figure 2.1d the nanoparticles are functionalized with methacryloxypropyl trimethoxysilane (MPTMS), which will covalently copolymerize with the acrylate monomer as the monomer undergoes a photo-initiated free radial polymerization. Now the nanoparticles become covalently trapped in the polymer matrix and do not aggregate.

2.2 Results and Discussion

To test the efficacy of the model system, 20 nm SiO_2 nanoparticles created via a Stöber process with the previously discussed functionalizations were added to holographic syrups containing an acrylate monomer. Initial formulations adhered to the constituents listed in Table 1.1, but while this formulation worked well for syrups without nanoparticles, it was found to yield inconsistent results upon the addition of nanoparticles, whether functionalized or not. After significant amount of

experimentation, it was determined that the photoinitiator system was the primary cause of the inconsistent results based on batch variations in the RBAX as revealed by gel chromatography. The exact cause of the inconsistent results is unknown, however, the addition of the nanoparticles could have changed the solubility of the photoinitiator system, or could have caused a secondary photochemical reaction between impurities in the RBAX and the nanoparticles.

2.2.1 Photo-Initiator System

Several sensitizers/dyes were examined as potential photoinitiators for the system, such as Rhodamine 6G and Diidofluorescein. Diidofluoroscein (DDFL) was selected for further research because it is a Xanthene derivative similar in structure to RBAX and has an absorbance λ_{max} of 532 nm, as shown in the absorption spectra in Figure 2.2. Since the primary system laser used in the research presented in this dissertation is a Nd:YAG doubled to 532 nm, it is expected that the close overlap between the laser line and λ_{max} will help maximize the overall quantum yield of the photoinitiator system. Also, since the bleaching kinetics of Xanthene dyes and their derivatives are relatively fast (on the order of 20 seconds), they are a good choice for HPDLC systems such as optical reflection gratings, since grating efficiency, in general, is enhanced with fast polymerization, which is driven in part by the availability of free radical initiators created by the bleaching process.

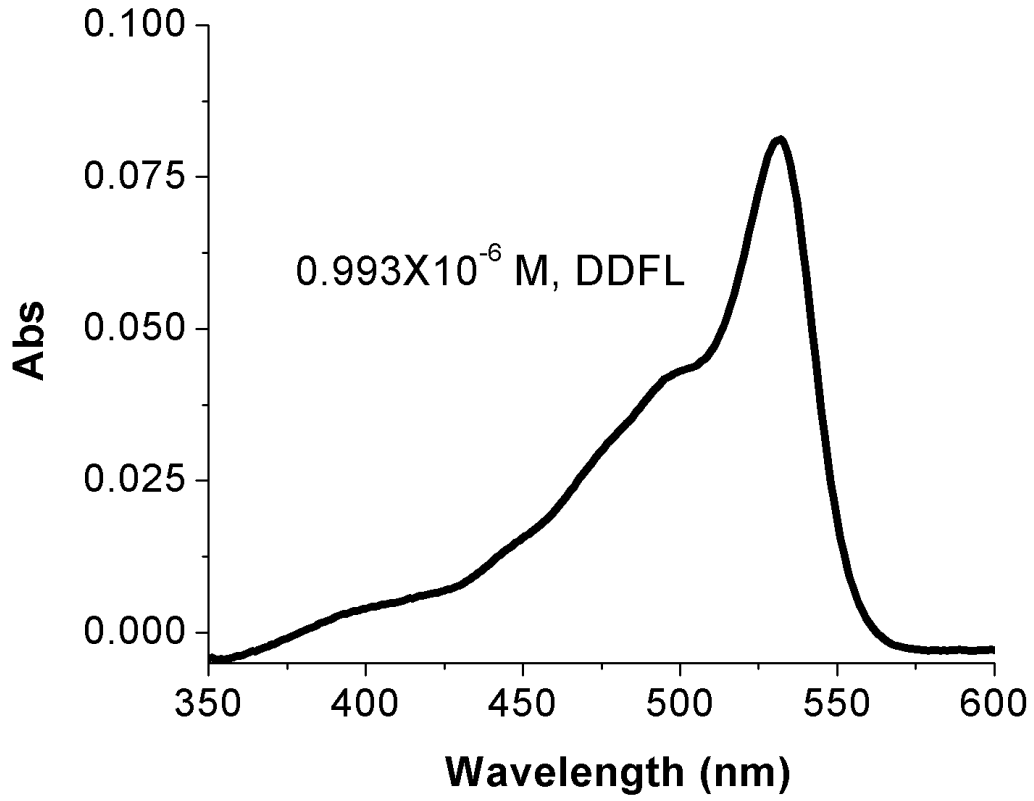

Figure 2.2 Absorption spectra of DDFL in an ethanol solution

NPG, a solid amine, was also replaced by a different co-initiator due to solubility issues, which appeared upon the addition of nanoparticles. It is well known that Xanthene systems, in general, are excited to a singlet state upon irradiation with light of an appropriate wavelength. This state is often converted to a more stable, longer-lived, triplet state through an inter-system crossing. Amines have been shown to be good electron donors to triplet state Xanthenes, with aromatic amines yielding the highest overall quenching of the triplet state for a similar system *[9].* For the above stated reasons, N-N'-dimethylamino-2,6-diisopropylaniline (DIDMA) was chosen for investigation, as it is an aromatic amine that is in the liquid state at

room temperature. To maximize the quantum efficiency of the selected DDFL/DIDMA system, a brief photoluminescent study of the system fluorescence was conducted at different molar ratios of DDFL to DIDMA, as shown in Figure 2.3. A complete photochemical study would be necessary to completely understand the mechanisms of radical formation for DDFL/DIDMA system, which to our knowledge has never before been used as a photo-initiator system. However, because other Xanthene/amine systems used to polymerize methacrylates have shown interaction

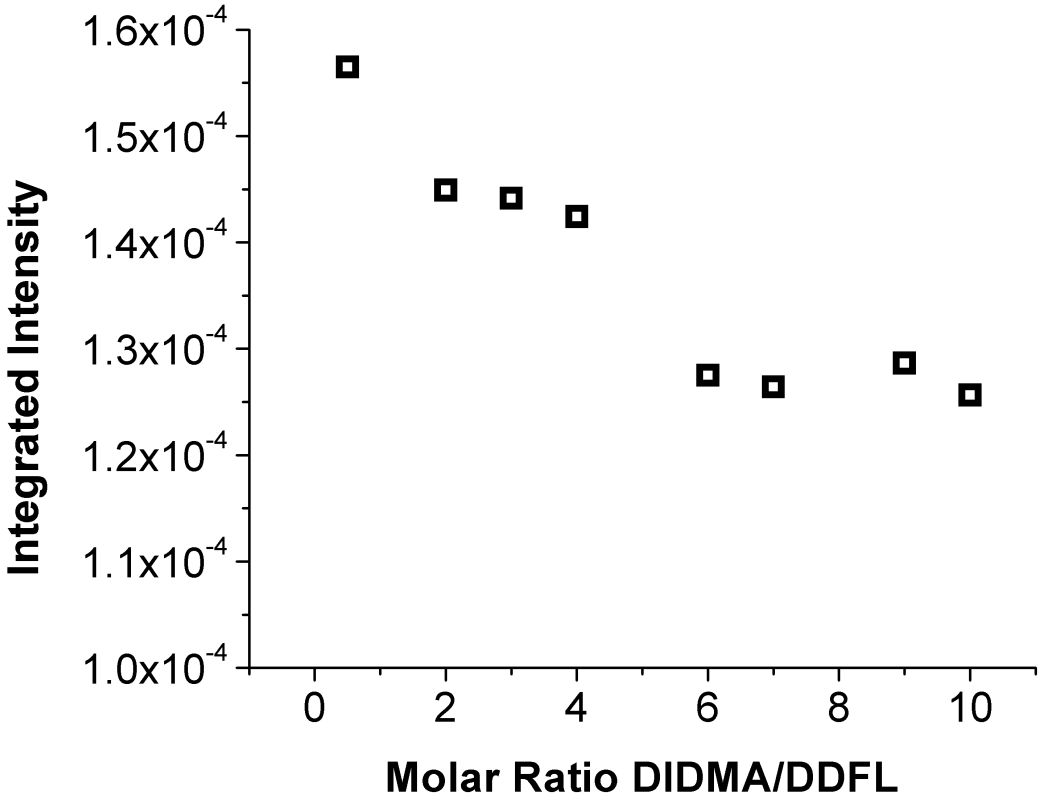

Figure 2.3 Photoluminescent study of fluorescence of new photoinitiator system. The variation of the integrated peak intensity of the fluorescence as the molar ratio of DIDMA to DDFL provides an indication of the optimal ratio as evidenced by maximizing the quenching of the fluorescence.

with the single state dyes leads to inhibition of polymerization, the good results of the photo-initiator in our system provides evidence that interaction of the DIDMA with the triplet-state of the DDFL is the most likely mechanism for bleaching and subsequent free radical generation*[10]*. Based upon Figure 2.3, the molar ratio of DDFL/DIDMA was set to 7 in subsequent recipes, with good results.

2.2.2 Nanoparticle Sequestration and Dispersion

New syrups based upon replacing the RBAX/NPG system with the DDFL/DIDMA photoinitiator system were then used to create reflection Bragg gratings using a 2-beam holographic system in a 180° configuration as illustrated schematically in Figure 1.1 b. The resultant grating's optical and electrical switching properties were characterized before microtoming sample cross-sections for TEM analysis. A control syrup without nanoparticles was created as a baseline for comparison purposes. A cross-sectional TEM micrograph of a grating without particles is shown in Figure 2.4a. The morphology displayed in the image is typical of acrylate-based HPDLC gratings, with irregular shaped liquid crystal droplets arranged in a periodic linear array *[11]*. The remaining syrups were identical in composition with the control syrup; with the exception that 10 wt% of the monomer was replaced by an equal weight of the respective nanoparticles. Despite the presence of 10 wt% of unfunctionalized nanoparticles in the starting syrup, the sample shown in Figure 2.4b appears to have few nanoparticles present, with the exception of an occasional small agglomeration of particles in the polymer-rich domain as shown in the inset. This lack of particles is strongly indicative of the

particles residing in the liquid crystal domains of the sample; the liquid crystal is removed prior to TEM analysis. The sample containing PTES-functionalized nanoparticles (Figure 2.4c) displays a significantly larger fraction of particles in the polymer rich domain, but the nanoparticles are agglomerated. As seen in the TEM image, this undesirable agglomeration appears to significantly disrupt the periodic structure of the grating in areas localized around the particle agglomerations. For the gratings containing the MPTMS functionalized nanoparticles, the cross-section shown in Figure 2.4d exhibits particles that are well dispersed throughout the polymer domain. Overall, when looking at the progression of liquid crystal droplet morphology in the images in Figure 2.4, the presence of particles in the samples changes the structure from an irregular droplet structure to a more continuous lamellar structure. The precise mechanism of this evolution is unclear without further research.

2.2.3 Optical and Electric Switching Characterization

Evaluating the optical and electrical switching characteristics of these same samples, as shown in Figure 2.5, yields an indication of the overall effect of adding high loadings of nanoparticles on the optical response of the HPDLC to an applied field. In Figure 2.5a, it can be seen that the diffraction efficiency of the control sample, as measured by the depth of the reflection notch, is 81%. The diffraction efficiency of the other films displayed in the figure, except for the film containing the PTES functionalized nanoparticles, is the same within observed experimental variation, as expected because of the similarity between the refractive index of the

silica and the polymer. An optical refractometer was used to check the refractive index of the homogeneous holographic syrups, and the addition of nanoparticles only caused a change in refractive index of $\Delta n=.005$, confirming that there should be little change diffraction efficiency due to the enhancement of index contrast. However, the film containing PTES functionalized nanoparticles exhibited markedly degraded diffraction efficiency, indicating that observed distortion of the periodic structure is a macroscopic effect across the sample. It should be additionally noted that the background scattering is not significantly changed from the control sample to the samples containing the functionalized nanoparticles. The background falloff in the blue region of the sample is attributed to scattering from the liquid crystal and is present in all samples. Therefore, the addition of dispersed SiO_2 nanoparticles into the HPDLC system has little to no measurable effect on optical scattering, which is not surprising, given the small refractive index difference between the nanoparticles and the polymer matrix. While the MPTMS functionalized nanoparticles are shown to be well dispersed in the polymer rich domain in Figure 2.4d, the absence of the liquid crystal in the TEM image (it flows out of the cross section upon microtoming, leaving vacancies in the TEM cross-sections) prohibits the conclusion that the nanoparticles are sequestered in the polymer-rich domain using only TEM analysis. However, the ability of the liquid crystal to orient in an electric field can provide strong evidence as to the presence of particles in the liquid crystals. Upon alignment with the electric field, the index contrast between the liquid crystal and polymer changes from 0.115 (for disordered LC) to approximately zero, effectively switching the grating state from on to off. If the order of the liquid

crystal is frustrated by the presence of nanoparticles, this should be evidenced by the lack of switching under the presence of the electric field. Figure 2.5b shows the repeatable result that the sample with unfunctionalized particles does not switch, strongly indicating the presence of nanoparticles in the liquid crystal. Conversely, the remainder of the samples switch as expected, providing evidence that nanoparticles are not present in the liquid crystal, and are sequestered in the polymer domain. Closer examination of Figure 2.5b yields the interesting, and potentially technologically important result that this sequestration drastically reduces the voltage necessary to switch the state of the grating, although further investigation is necessary to determine the precise mechanism by which this occurs.

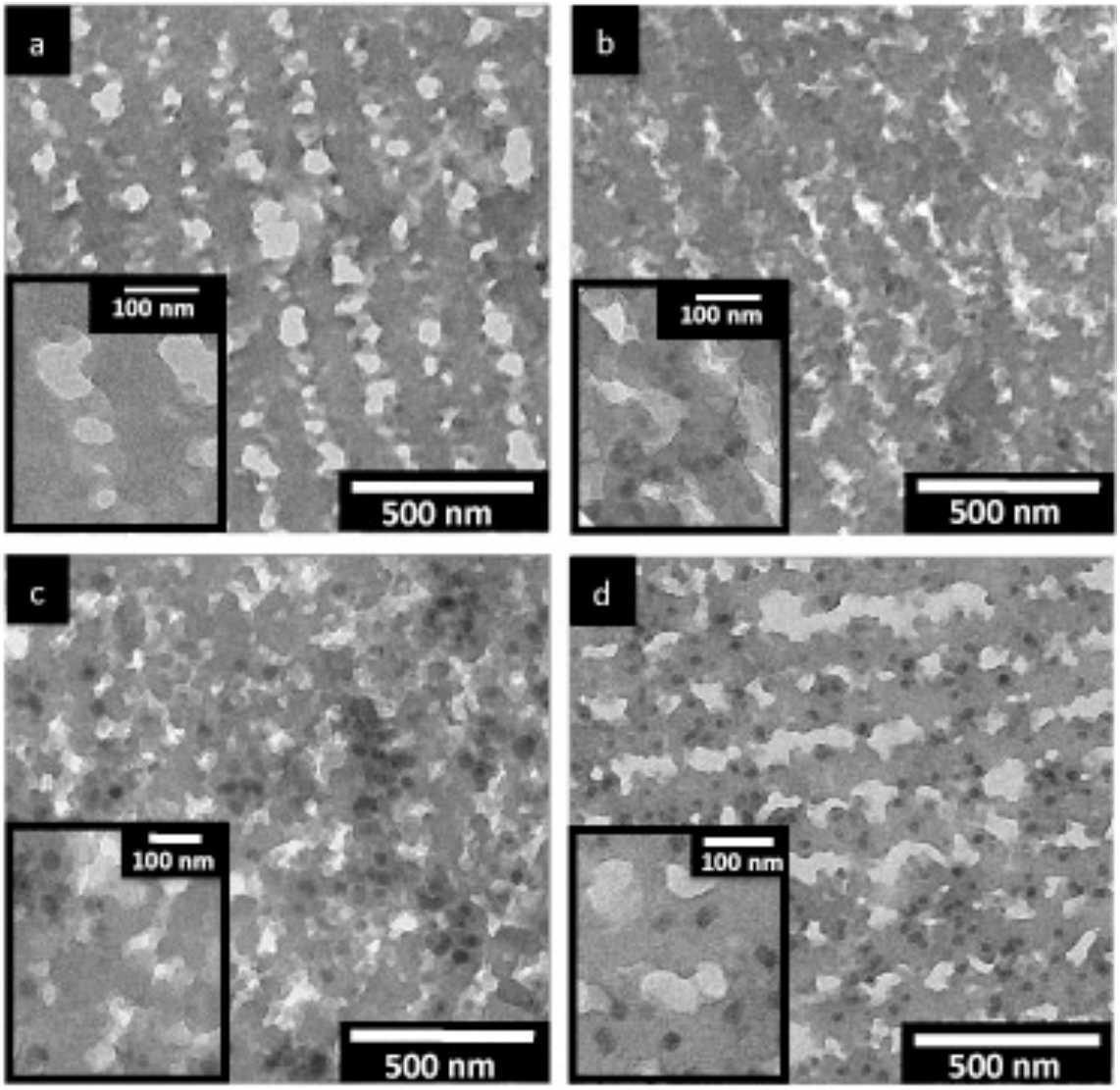

Figure 2.4 TEM micrographs of 75 nm thick microtomed cross-sections of HPDLCs created through 2-beam exposure. All samples contain the same acrylate based polymer matrix and liquid crystal. a) Without nanoparticles, b) with 10 wt% unfunctionalized 20 nm diameter SiO_2 nanoparticles, c) with 10 wt% SiO_2 nanoparticles functionalized with PTES, and d) with 10 wt% SiO_2 nanoparticles functionalized with MPTMS.

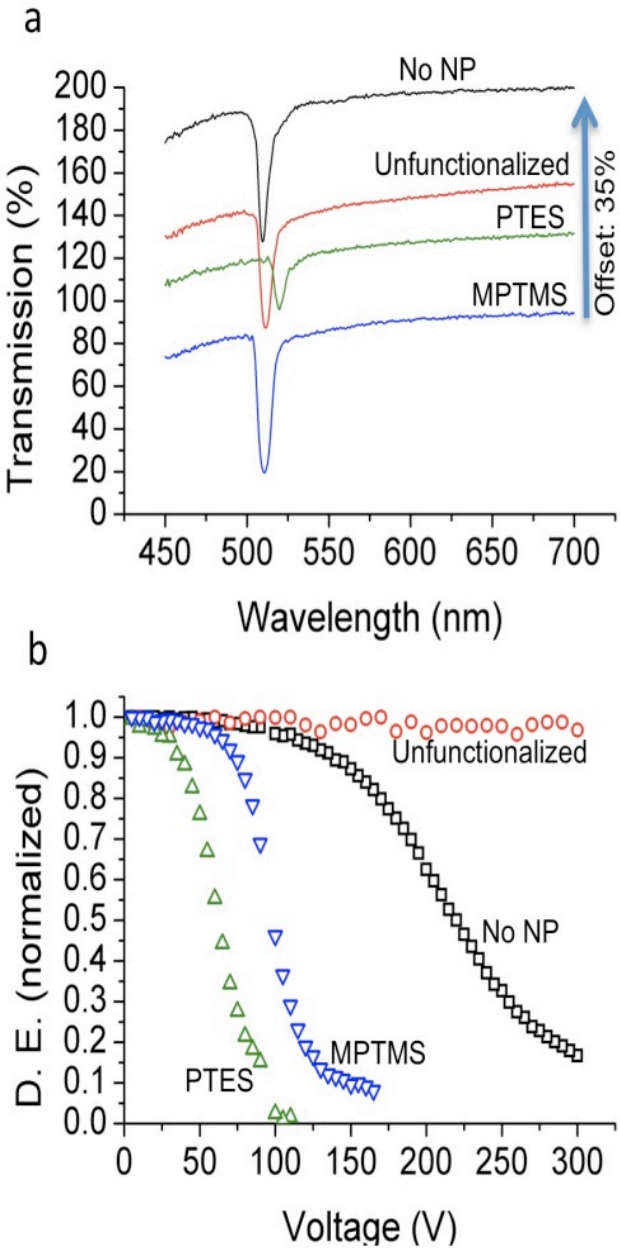

Figure 2.5 a) White light transmission spectra and b) electrical switching characterization for reflection Bragg gratings created by HPDLC. The four samples displayed in the graphs are the same samples shown in the TEM images in Figure 2, and are all the same thickness.

2.2.4 NMR Surface Functionalization Analysis

While this work demonstrates that through proper reactive surface coupling that nanoparticles can be sequestered within the polymer domain, further work was necessary to understand the mechanism. Before we can conclusively state that the dispersion of the MPTMS functionalized nanoparticles, and agglomeration of the PTES functionalized nanoparticles was due to interactions between the polymeric matrix and the nanoparticles, it was necessary to ensure that the nanoparticles were indeed similarly functionalized. Both PTES and MPTMS react with a silica surface through similar hydrolysis and condensation reactions. Using NMR, the degree of surface coverage can then be qualitatively compared by monitoring the change in hydroxyl groups on the silica nanoparticles via the Q^3 peak in ^{29}Si solid-state NMR using a Techmag 500 MHz spectrometer with measurements at 99.3 MHz. Saturation recovery was used to measure the T_1 relaxation time for all samples. Spectra were measured using a 1-pulse sequence and corrected for unrelaxed intensity to yield quantitative data, which is presented in graphical form in Figure 2.6 and numerically quantified in Table 2.1. As seen in the Table, the Q^3:Q^4 ratio changed from 35:65 for unfunctionalized particles to 24:76 and 26:74 for the PTES and MPTMS functionalized particles, respectively. The similar change in Q^3:Q^4 ratios for both the PTES and MPTMS functionalized particles suggests that a similar fraction of the hydroxyl groups on the surface of the particles have been replaced by the chemisorbed molecules, and thus that the PTES and MPTMS surface coverage is the same within experimental error. The number of hydroxyl groups within the nanoparticles is not known, and thus the NMR data cannot be used to quantitatively

determine the degree of surface functionalization. Therefore, it is not unreasonable to assume that the PTES functionalized particles agglomerate due to unfavorable polymer-nanoparticle interactions and that the MPTMS functionalized particles disperse due to reactions between the matrix and the functionalized nanoparticle. See Chapter 5 for more detailed treatment of these NMR studies.

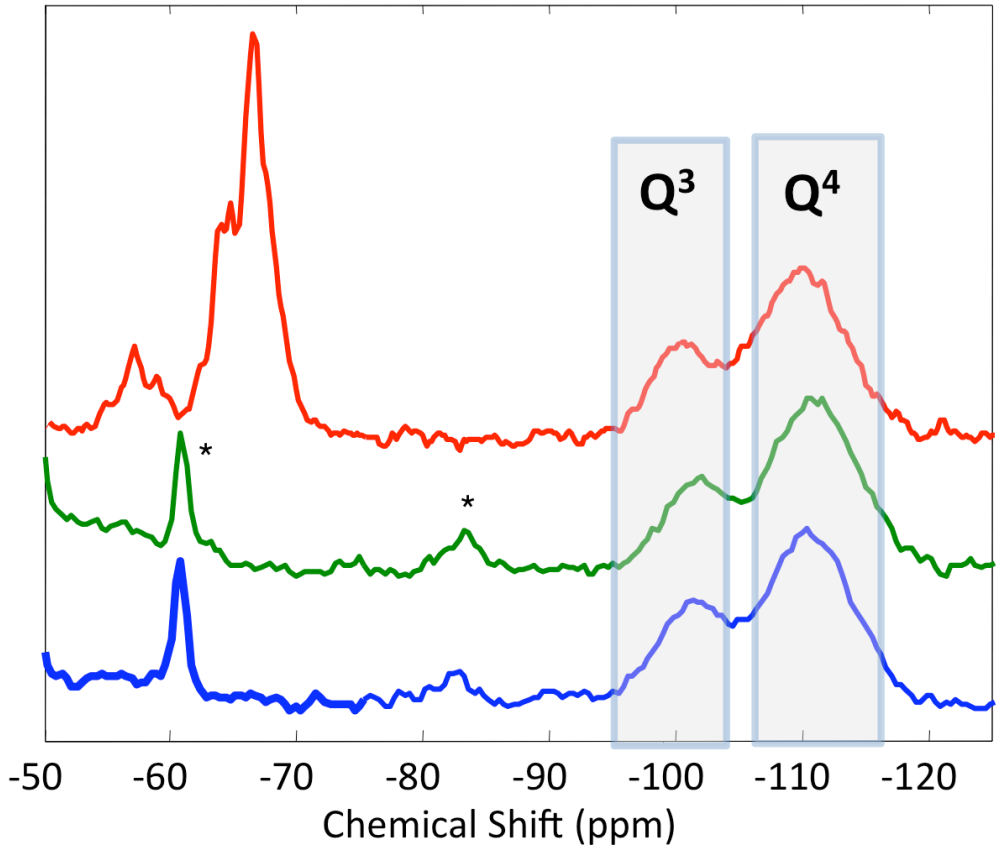

Figure 2.6 The quantitative 99 MHz silicon NMR spectra of (a) unfunctionalized silica nanoparticles, (b) PTES functionalized silica nanoparticles and (c) MPTMS functionalized silica nanoparticles. The marked peaks (*) are from background signals in the probe.

Table 2.1 Quantitative 99 MHz silicon NMR data. The ratio of the integrated Intensity of the Q^3 and Q^4 peaks for unfunctionalized, PTES functionalized and MPTMS functionalized silica nanoparticle samples as well as the corresponding T_1(s) relaxation times. For the experimental setup used, samples with relaxation times under 400 seconds can be treated quantitatively. The data is tabulated from the same experiments as presented in Figure 2.6.

Sample	Q^3:Q^4	T_1 (s)		
		T^3	Q^3	Q^4
Unfunctionalized	35:65		61	315
PTES-functionalized	24:76		53	379
MPTMS-functionalized	26:74	17.1	33.2	46.6

2.2.5 Grating Morphology

A second unexplored area is the effect of nanoparticles on the morphology of the resultant holographic structures. A complete model will require a careful study of diffusion, gelation and polymerization kinetics as a function of nanoparticle volume fraction and surface coverage. We can however postulate that in the case of MPTMS functionalized particles, that because the number of MPTMS on a given nanoparticle is large, that the probability of an given methacrylate group on the surface of the nanoparticle reacting with the polymerizing matrix is high, and that

given the large number of reactive sites per nanoparticle that the nanoparticle thus acts as highly functional cross-linking agent. Previous works have shown an increasing degree of liquid crystal phase separation when the degree of monomer functionality is increased *[11, 12]*. It is speculated that in analogy to the previous cited works, the increase in cross-linking due to the reactive nanoparticle correspondingly increases the liquid crystal volume fraction in the low intensity region, resulting in the lamellar-like morphology. Analysis of the liquid crystal morphological changes in the TEM images (using the NIH ImageJ software package) in Figure 2.4 indicates that the areal fraction of liquid crystal in the grating increases from 24.8% in the control sample to 30.6% for the sample containing MPTMS functionalized nanoparticles, supporting this conclusion. We can additionally posit that this lamellar morphology is responsible the reduction in switching voltage for films containing nanoparticles sequestered in the polymer domain. Because the reduction appears to be independent of the degree of nanoparticle dispersion, it is likely that the effect is due to the change in liquid crystal droplet morphology rather than because of some inherent property of the nanoparticles themselves. The lamellar morphology, as observed in Figure 2.4d, has a lower surface to volume ratio, thus reducing the necessary field strength necessary to overcome effects such as liquid crystal surface anchoring.

2.2.6 Nanoparticle Alignment

Here, we have primarily used small particles to avoid light scattering, but in the case of silica particles, which have a similar refractive index as the HPDLC components, larger particles can be used. As the particle size approaches the order of the periodicity, an interesting particle alignment is observed. As the particle size approaches the order of the periodicity, an interesting particle alignment is observed (Figure 2.7). Although more research needs to be performed to investigate the details and limitations of the alignment, the transmission grating made with 200 nm particles displayed in Figure 2.7 provides a tantalizing glimpse of the potential for directing the assembly of colloidal materials.

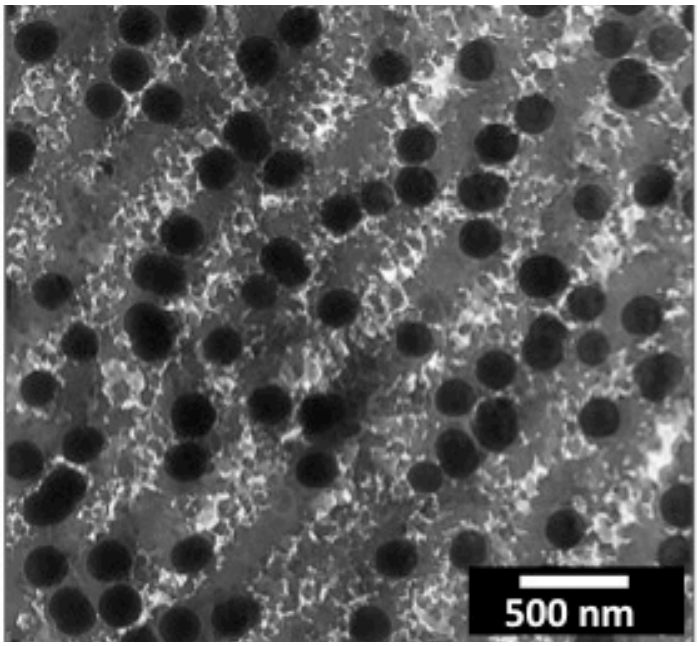

Figure 2.7 TEM micrograph of a 90 nm thick microtomed cross-section of a HPDLCs created through 2-beam exposure. The sample contain the same acrylate based polymer matrix and liquid crystal as the nanoparticle containing systems; here the nanoparticles have been replaced with 10 wt% of 200 nm diameter MPTMS functionalized SiO_2 colloids.

2.3 Experimental Procedures:

Silica nanoparticles (20 nm diameter) were synthesized in ethanol using the modified Stöber recipe presented in Chapter 1 *[13]*. All chemicals used to synthesize nanoparticles were used as received. In a 250 ml flask, 1.5 ml of de-ionized water and 3 ml of a 28% ammonium hydroxide solution (Aldrich) was added to 120 ml of absolute ethanol and stirred vigorously for 30 minutes at room temperature using a magnetic stir bar. 3 ml of tetraethoxysilane (TEOS, Gelest) was added via pipette as quickly as possible. The resultant solution was then purged with dry nitrogen and stirred for 12 hours. The same chemicals and procedures were used to produce 200 nm particles, with the volumes changed to 6.9 ml of TEOS, 3.5 ml of ammonium hydroxide solution and 8.5 ml of H_2O. A functionalizing agent, either [1 ml of methacryloxypropyl-trimethoxysilane (MPTMS, Gelest) or 1.1 ml of pentyl-triethoxysilane (PTES, Gelest), was added without modification to the unchanged basic Stöber solution, then stirred at room temperature for 24 hours. The resultant functionalized particles were cleaned four times via dialysis exchange in absolute ethanol. A holographic syrup consisting of a photo initiator, diiodofluoroscein, DDFL, (1 wt%, Aldrich); co-initiator, N-N'-dimethylamino-2,6-diisopropylaniline, DIDMA, (2.5 wt%, Aldrich); solubilizer, N-vinyl pyrrolidinone (10 wt%, Aldrich); surfactant for switching voltage reduction, octanoic acid (5 wt%, Aldrich); liquid crystal, TL213 (29 wt%, EMD Chemicals); multi-functional monomer, penta-erithitol penta/hex-acrylate, (35 wt%, Aldrich), 10 wt % of the synthesized silica nanoparticles; stabilizer, 4-Methoxyphenol, MEHQ (.04 wt%, Aldrich); and a thiol-ene co-monomer added for system stabilization (2.5 wt %,

Norland optical adhesive No. 65). An additional 5 wt% of 10 μm, non-reactive glass spheres are added for the purposes of dictating holographic cell thickness. The holographic syrup components were added in the order listed and mixed with a rotary vortexer between each addition. Prior to use, the nanoparticle/ethanol solution was added to the acrylate monomer, along with the stabilizer, ultrasonicated for one-half hour to ensure adequate dispersion of the nanoparticles, and then distilled with a rotary evaporator to remove the ethanol.

To create the holographic cell, the syrup was sandwiched between glass slides coated with a thin layer of indium tin oxide (ITO) and sealed at the edges with an epoxy adhesive. Bragg reflection gratings were created using a 2-beam holographic system with the laser beams incident a normal to the front and back cell surfaces. The laser used is a diode pumped solid-state Nd:YAG laser doubled to 532 nm (Coherent Verdi). For all experiments, the laser power was 50 mW at the sample. The samples were exposed for 60 seconds, followed by post cures of 2 minutes each under a UV lamp and intense white light. After optical and electrical switching characterization, the samples were microtomed in 75 nm sections using a Leica ultramicrotome. TEM characterization was accomplished on a Philips CM200. Analysis of liquid crystal areal fraction was accomplished by thresholding the image so that liquid crystal vacancies were white and the remainder of the image was black, then taking the ratio of white to black pixels.

2.4 Conclusions

The combination of the TEM image and the switching data strongly indicates that appropriate chemical functionalization enables control over where the nanoparticles reside within a HPDLC. The functionalized particles are sequestered in the polymer rich domain while the majority of the unfunctionalized particles are present in the liquid crystal domain. These results suggest the feasibility of a more general schema for directing the assembly of nanoparticles via externally applied optical fields. Although the work here only utilized a simple grating structure, a strength of this technique is that it can be used for arbitrarily complex 3-D structures as long as the structure can be created using holographic interferograms, and thus the technique can be generalized to a powerful tool for assembly of different types of particles into complex, designed structures on the sub-micron scale.

2.5 References

[1] R. L. Sutherland, V. P. Tondiglia, L. V. Natarajan, J. M. Wofford, S. A. Siwecki, G. Cook, D. R. Evans, P. F. Lloyd, T. J. Bunning, "Liquid crystal Bragg gratings: dynamic optical elements for spatial light modulators", presented at *Emerging Liquid Crystal Technologies II*, San Jose, CA, USA, **2007**.

[2] R. L. Sutherland, L. V. Natarajan, V. P. Tondiglia, T. J. Bunning, "Holographic polymer-dispersed liquid crystals in display applications", presented at *Liquid Crystal Materials, Devices, and Applications IX*, Santa Clara, CA, USA, **2003**.

[3] J. K. A. Urbas, V. Tondiglia, L. Natarajan, R. Sutherland, O. Tsutsumi, T. Ikeda, T. Bunning,, *Advanced Materials* **2004**, *16*, 1453.

[4] O. V. Yaroshchuk, L. O. Dolgov, *Optical Materials* **2007**, *29*, 1097.

[5] N. Suzuki, Y. Tomita, *Appl. Opt.* **2004**, *43*, 2125.

[6] C. L. D. R. A. Vaia, L. V. Natarajan, V. P. Tondiglia, D. W. Tomlin, T. J. Bunning,, *Advanced Materials* **2001**, *13*, 1570.

[7] R. Jakubiak, D. P. Brown, F. Vatansever, V. P. Tondiglia, L. V. Natarajan, D. W. Tomlin, T. J. Bunning, R. A. Vaia, "Holographic photopolymerization for fabrication of electrically switchable inorganic-organic hybrid photonic structures", presented at *Organic Photonic Materials and Devices V*, San Jose, CA, USA, **2003**.
[8] M. J. E. C. S·nchez, C. van†Heesch, C.†W.†M. Bastiaansen, D.†J. Broer, J. Loos, R. Nussbaumer,, *Advanced Functional Materials* **2005**, *15*, 1623.
[9] C. Valderas, S. Bertolotti, C. M. Previtali, *Journal of Polymer Science Part A: Polymer Chemistry* **2002**, *40*, 2888.
[10] M. L. Gomez, V. Avila, H. A. Montejano, C. M. Previtali, *Polymer* **2003**, *44*, 2875.
[11] R. T. Pogue, R. L. Sutherland, M. G. Schmitt, L. V. Natarajan, S. A. Siwecki, V. P. Tondiglia, T. J. Bunning, *Applied Spectroscopy* **2000**, *54*, 12A.
[12] L. V. N. T. J. Bunning, V. P. Tondiglia, G. Dougherty, R. L. Sutherland,, *Journal of Polymer Science Part B: Polymer Physics* **1997**, *35*, 2825.
[13] A. Van Blaaderen, J. Van Geest, A. Vrij, *Journal of Colloid and Interface Science* **1992**, *154*, 481.

CHAPTER 3

ADDITION OF NANOPARTICLES TO THIOL-ENE H-PDLC SYSTEMS WITH INVESTIGATIONS ON THE IMPACT TO POLYMERIZATION KINETICS AND GRATING FORMATION

3.1 Introduction

As mentioned in Chapter 1, there are numerous advantages to using thiol-ene based polymers in HPDLC systems, the polymers have a higher index of refraction than acrylate-based systems, allowing higher diffraction efficiencies for gratings of the same thickness *[1]*. The polymerization mechanism for thiol-ene polymers is a free-radical initiated, step-growth reaction. As compared to acrylate systems, the system gel-point is delayed a higher degree of conversion (>50% vs. <5%). The later gel-point allows a much higher degree of cure shrinkage to occur while the system is still in a liquid state, thus avoiding the high cure stresses of acrylate-based systems*[2]*. In most thiol-ene based HPDLC systems, the gel-point occurs well after phase separation has begun, allowing the primary de-mixing mechanism to be liquid-liquid de-mixing, whereas in acrylate systems, phase separation occurs primarily during liquid-gel de-mixing *[3]*. Another effect of the phase separation occurring prior to gelation is that the liquid crystal droplet morphology is largely spherical, which reduces random scattering present in acrylate HPDLCs due to distorted, non-spherical liquid crystal droplet morphologies*[4]*. Thiol-ene systems are not inhibited by oxygen, as are acrylate systems, which eases some of the processing steps necessary for preparation of the HPDLC syrups *[5]*. For most thiol-

ene formulations using Norland resins, the only addition (beyond the liquid crystal) is a photo-initiator. This is contrasted to acrylate formulations, which sometimes have 4-5 additions beyond the liquid crystal. One last advantage of thiol-ene systems over the acrylate system is the stability of gratings created in the thiol-ene system. Thiol-ene systems can be driven to close to 100% conversion during the holographic process, whereas significant portions of unreacted monomer remains kinetically trapped in the acrylate polymer due to the early gelation in acrylate systems. This trapped monomer can slowly diffuse and react over time, bridging some of the liquid crystal domains and causing an upward creep in the voltage necessary to switch the state of the liquid crystal *[6]*. For this work, the slowed evolution of viscosity and the subsequent delay in gelation in step-growth polymerizations should allow longer diffusion times for nanoparticles in the system.

Because of the listed advantages, there have been an increasing number of studies of HPDLC systems utilizing thiol-ene polymers *[3, 4, 6-9]*. Thiol-ene polymers have been increasingly studied in other uses as well *[10-15]*. Early thiol-ene, HPDLC efforts have focused on a commercial Norland thiol-ene resin, Norland Optical Adhesive Number 65 (NOA 65), which is reportedly a mixture of a tri-functional thiol monomer and a tetra-functional polyurethane allyl ether *[1]*. However, more recent papers have examined other commonly used thiol and ‘’-ene” monomers, such as those presented in Figure 1.4. Several papers have explored the effects of various monomers, in both stoichiometric and non-stoichiometric ratios, upon polymerization kinetics *[1, 14]*.

3.2 Nanoparticle Addition to Thiol-ene HPDLC Formulations

All experimental formulations presented in this chapter have relied upon NOA 65, both as a basis of comparison to prior efforts and, more importantly, because efforts to use other, non-commercial thiol-ene formulations in conjunction with nanoparticles have only met with modest success. Because the C=C bond in methacrylate groups can be reactively incorporated into the thiol-ene reaction as an '-ene', the silica nanoparticles functionalized with MPTMS, as described in previous chapters, are used here without further modification. Thiols are weakly photo-reactive, and the NOA 65 formulation contains a photo-initiator, but previous efforts have reported the need for an additional photo-initiator to successfully reach high diffraction efficiencies by the holographic process *[6]*. The formulation used in all experiments in this chapter, prior to the addition of nanoparticles, was 70 wt% NOA 65, 2 wt% Darocur 4265 (a commercial UV photoinitiator, which is a mixture of 50 % 2,4,6-Trimethylbenzoyl-diphenyl-phosphineoxide and 50 % 2-Hydroxy-2-methyl-1-phenyl-propan-1-one), and 30 wt% EMD BL-038 (a low molecular weight, nematic liquid crystal).

Holography was performed using a system configured in a 2-beam normal incidence, such as illustrated schematically in Figure 1.1. An Ar^+ laser at 363.8 nm was utilized with the laser intensity set to irradiate the sample with 150 mW/cm^2, unless otherwise noted. Upon addition on nanoparticles, the weight fractions of both monomer and liquid crystal were reduced equally to maintain the monomer-

liquid crystal balance in the formulation. Figures 3.1 and 3.2 display TEM micrographs of a series of formulations with increasing loading of MPTMS-functionalized silica nanoparticle, thus illustrating typical results of addition of nanoparticle into NOA 65 syrups. In Figure 3.1a the formulation was prepared without the addition of nanoparticles as a reference. Figure 3.1 b, Figure 3.2a, and Figure 3.2b display TEM micrographs of formulations containing 5, 10 and 20 wt% nanoparticles, respectively. While the sample in Figure 3.1 b) was microtomed in an area without local grating structure (the overall sample diffraction efficiency was the highest of any sample shown in the figures), the emphasis here is that the nanoparticles display excellent dispersion throughout the polymer domain and remain sequestered outside the liquid crystal. The latter result, in contrast to the acrylate gratings discussed in Chapter 2, is unambiguous, as the liquid crystal still resides in the structure after microtoming, due to the discrete droplet morphology. In Figure 3.2 we see that nanoparticle dispersion is maintained even at very high loadings. It does appear that as the nanoparticle volume fraction increases, the number of liquid crystal droplets begins to decrease. From an optical analysis of the TEM micrographs presented, there is a 3.4x reduction in the areal density of liquid crystal droplets between the control sample and the sample containing 20 wt% nanoparticles. In Figure 3.3, we examine the effects of nanoparticle loading upon the optical and switching performance of the same 4 samples used in Figures 3.1-2. Examining the value of diffraction efficiency prior to the application of voltage (0 Volts), we see that up to a 10% loading the diffraction efficiency is unchanged within observed experimental variation. At 20 wt%, the diffraction efficiency begins to fall

off, most probably due to a reduced in Δn of the grating due to a reduced number of liquid crystal droplets, as the total liquid crystal volume fraction remains unchanged. The reasons for reduced liquid crystal droplet nucleation require further investigation.

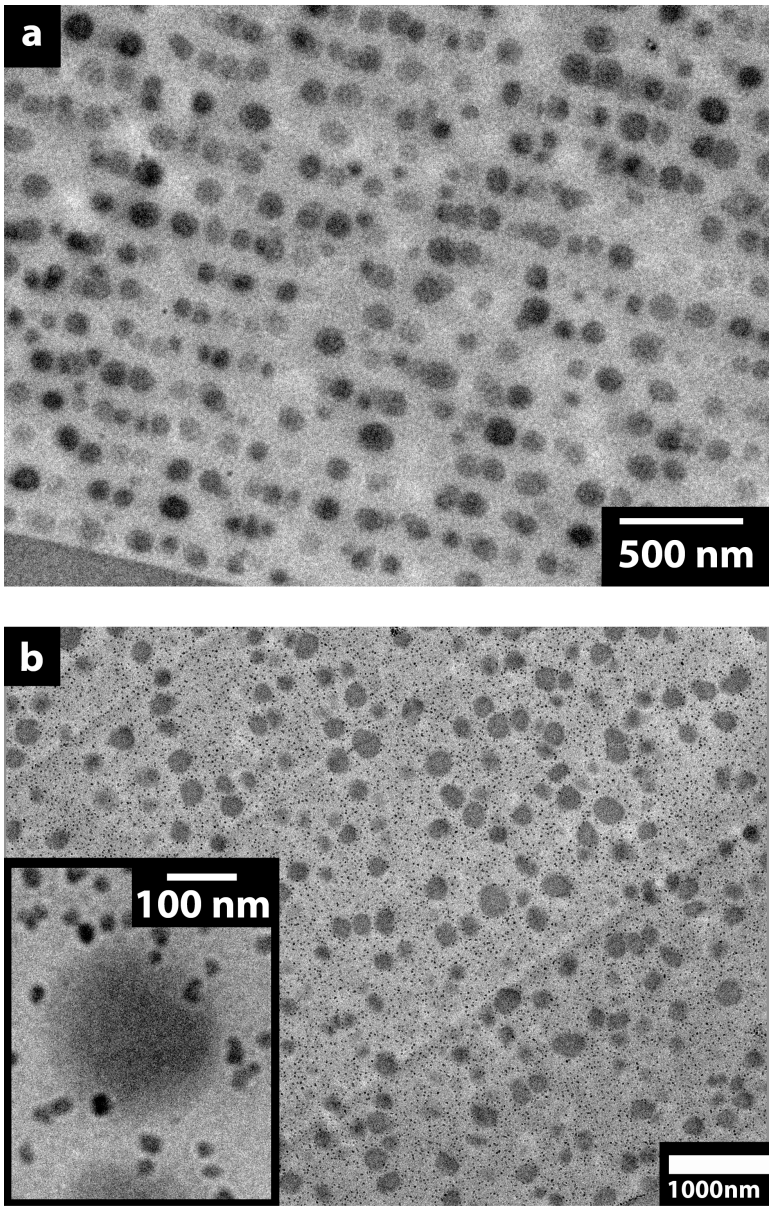

Figure 3.1 TEM micrographs of thiol-ene reflection gratings created using NOA 65 with BL-038 liquid crystal. Samples were microtomed in 75 nm slices prior to observation in TEM. The sample in a) contains no nanoparticles, while b) is loaded with 10 wt% of MPTMS-functionalized SiO2 nanoparticles with a mean radius of 28 nm.

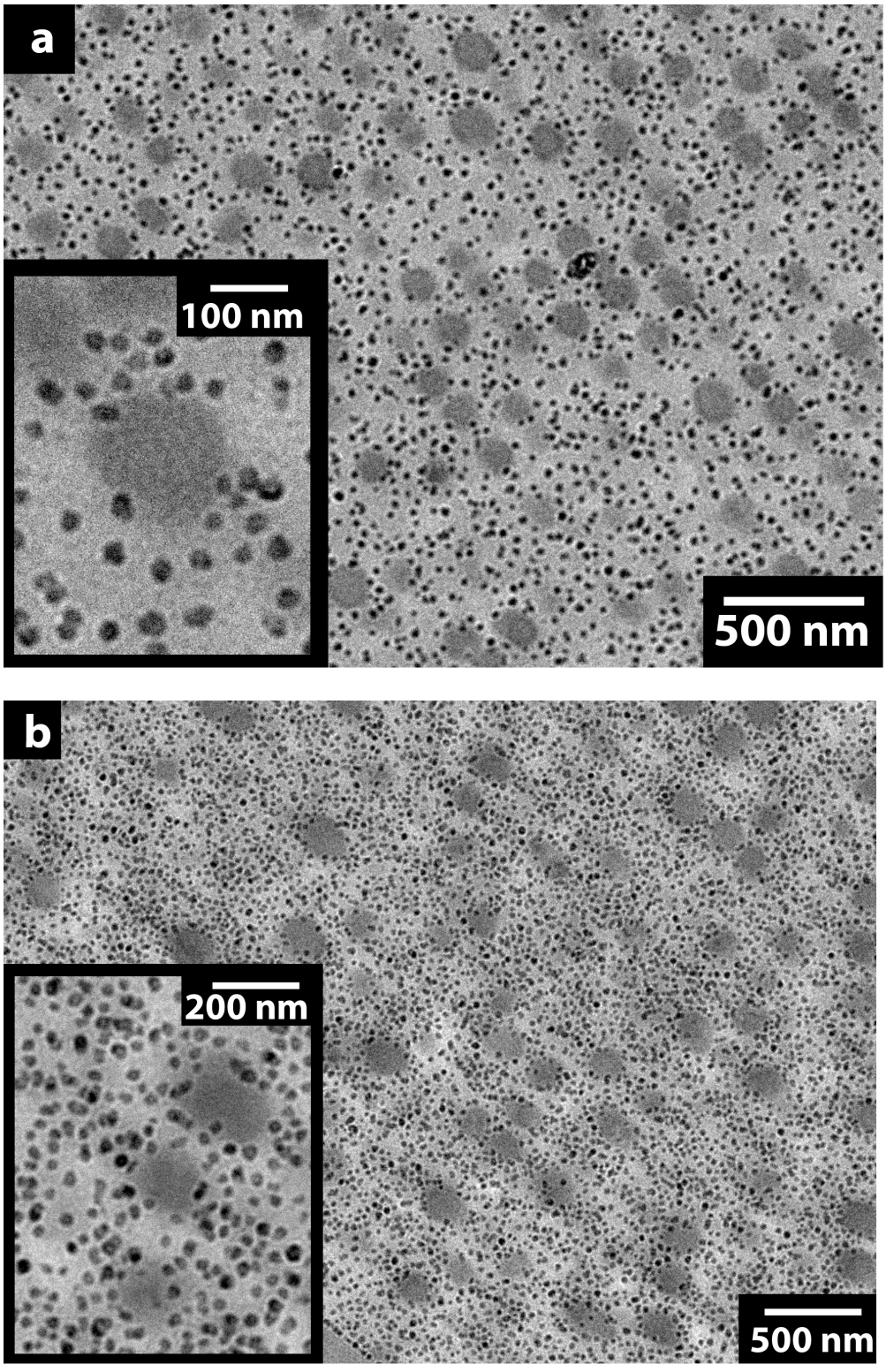

Figure 3.2 TEM micrographs of thiol-ene reflection gratings created using NOA 65 with BL-038 liquid crystal. Samples were microtomed in 75 nm slices prior to observation in TEM. The samples contain MPTMS-functionalized SiO_2 nanoparticles with a mean radius of 28 nm, at loadings of a) 10wt% and b) 20 wt%.

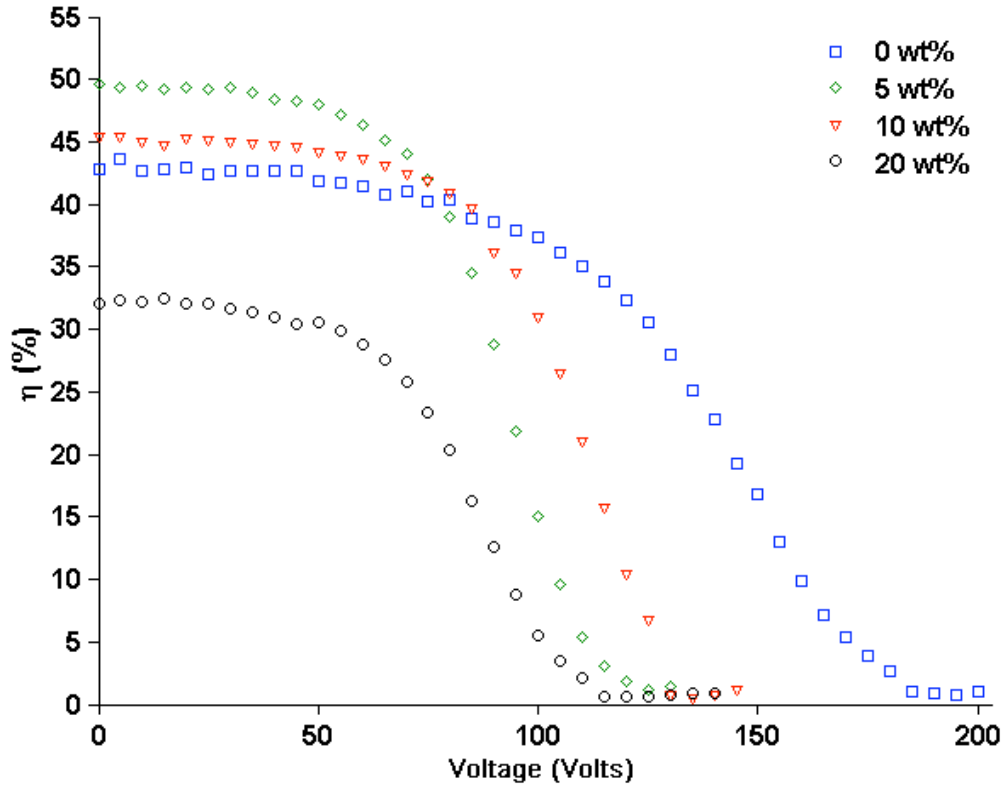

Figure 3.3 Diffraction efficiency versus voltage for the same thiol-ene reflection grating samples displayed in Figures 3.1 and Figure 3.2. Curves display the effect of varying the loading of MPMS-functionalized SiO_2 nanoparticles upon initial diffraction efficiencies and subsequent switching characteristics. All sample thicknesses are 10µm.

The areal density of droplets is reduced from the level of the control by .17x, in Figure 3.2a, but this does not appear to affect the diffraction efficiency. A plausible explanation can be gleaned by looking at the switching performance in Figure 3.3. For all samples containing nanoparticles, the gratings are completely switched to the transmissive state by 130 volts as opposed to 185 volts for the sample without nanoparticles. Constant initial diffraction efficiency combined with reduced switching voltage in this case implies larger liquid crystal droplets as confirmed by TEM analysis that the volume fraction of liquid crystal is unchanged. The decrease

in diffraction efficiency at higher loading is due to the definition of diffraction efficiency used in this case (the distance from the scattered baseline to the depth of the reflection notch). As the nanoparticle loading is increased, the baseline transmission decreases due to scattering from the nanoparticles.

3.3 Investigation of Real-Time Polymerization Kinetics and Grating Formation

3.3.1 Previous Efforts

In order to continue to improve the properties of optical gratings and to enhance the regularity of the periodic structures in HPDLC systems, it is necessary to understand the evolution of the chemical system during the grating formation. This evolution can yield greater understanding of the polymerization mechanisms and help to understand how reaction, diffusion and kinetic effects interplay during the creation of the periodic, phase-separated structures to affect items such as liquid crystal droplet morphology, gel point, and degree of phase separation.

A large body of work has been undertaken to understand these effects in acrylate and, more recently, in thiol-ene systems. In 1989, Carre *[16]* used real time studies of holographic systems to study reaction rates. It was noted that, in general, there were 3 regimes during grating formation: 1) an induction period due to oxygen inhibition, 2) a rapid photoinitiation which rapidly increased reaction rates and bleaching rates and 3) a plateau region in the reaction rate after significant bleaching of the photoinitiator molecules. In 1993, Sutherland et al, confirmed the same general regimes for acrylate HPDLC system *[17]*. In 2003, Bunning completed real-time experiments on thiol-ene H-PDLC system and compared the results with

multi-functional acrylates *[9]*. Lee et. al. used thiol-functionalized silica nanoparticles in a thiol-ene nanocomposite and studied the effect of the nanoparticles upon the polymerization kinetics *[15]*. In this work, a slight decrease in polymerization rates were noted with increasing loading, until bridging between particles was probable, at which point, polymerization was significantly increased, which was attributed to higher measured viscosities inhibiting termination.

3.3.2 Investigation of Polymerization Rate with Real-Time Infrared Spectroscopy

To investigate the effect of functionalized, reactive nanoparticles upon the polymerization rate of thiol-ene H-PDLC formulations, real-time infrared spectroscopy (RTIR) was performed. Experiments were conducted upon a Thermo Electron Nexus 670 Fourier-transform infrared spectrometer equipped with a MCT detector. Without specific facilities, it is not possible to simultaneously conduct H-PDLC and RTIR experiments on the same sample. To achieve conditions that were as close as possible to holographic experimental conditions, H-PDLC formulations were exposed using a high-pressure Hg arc lamp (Exfo Acticure 4000) using 365 nm light with a standard intensity of 3.5 mW/cm^2, to create polymer dispersed liquid crystal (PDLC) structures. While valuable information can be gleaned from this typed of experiment, it is important to note that light intensities are drastically lower than are typically used for thiol-ene H-PDLC experiments. Additionally, PDLC sample morphologies can have characteristic lengths that are an order of magnitude larger

than H-PDLC samples, requiring much larger diffusion lengths before phase separation can occur.

Holographic syrups with varying nanoparticle content were prepared using the same methodologies as used in the previous section. Experiments were performed on 5 different samples, containing 0, 1, 3, 5 and 7 wt% of MPTMS-functionalized SiO_2 nanoparticles. Monitoring the absorption peak at 2575 cm^{-1}, which is assigned to the S-H stretch vibrational mode, allowed monitoring of the polymerization rate for the sample. Spectra were taken twice per second, and custom software was used to curve-fit maximum intensities over time. Normalizing this curve yields the fraction of remaining reactive groups versus time, which can be numerically differentiated to yield quantitative polymerization rates versus time for the specific exposure intensity. Figure 3.4 displays the results for all of the samples. In a similar fashion to the results found by Lee et. al. for reactive nanoparticle-filled thiol-ene nanocomposites, the photopolymerization rate was essentially unchanged for low volume fractions (0-3 wt%) and showed a slight enhancement for weight fractions of 5 and 7%. Because the polymerization rate does not diminish from the increased viscosity due to the presence of the nanoparticles, we can infer that, for all of the formulations tested, the reactive groups in the system is not diffusion-limited at the exposure intensity used.

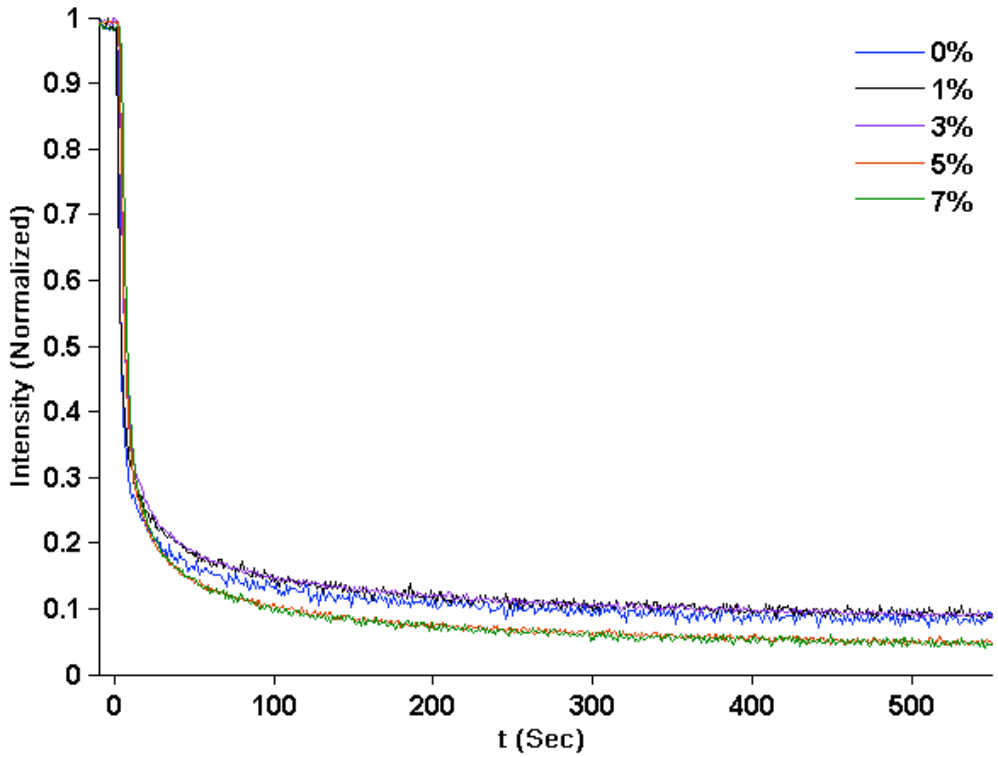

Figure 3.4 Real-time infrared spectroscopy results for NOA 65 HPDLC formulations with varying weight fractions of MPTMS-functionalized silica nanoparticles (28 nm), as listed in the legend. Spectra were taken twice per second. The peak at 2575 cm^{-1}, which is assigned to the S-H stretching mode, was curve-fit. The maximum of this peak is then plotted versus time.

3.3.3 Real-Time evolution of Diffraction Efficiency for Thiol-ene HPDLCs

To monitor the real-time evolution of diffraction efficiency of a Bragg grating during formation in the holographic process, a system was constructed to allow white light illumination of the sample during the grating writing process. By monitoring the white-light reflection, grating formation can be captured in real-time. A simplified schematic of the setup used is shown in Figure 3.5. The system is a single-beam setup, which uses a self-reflection from a prism to form the interference pattern.

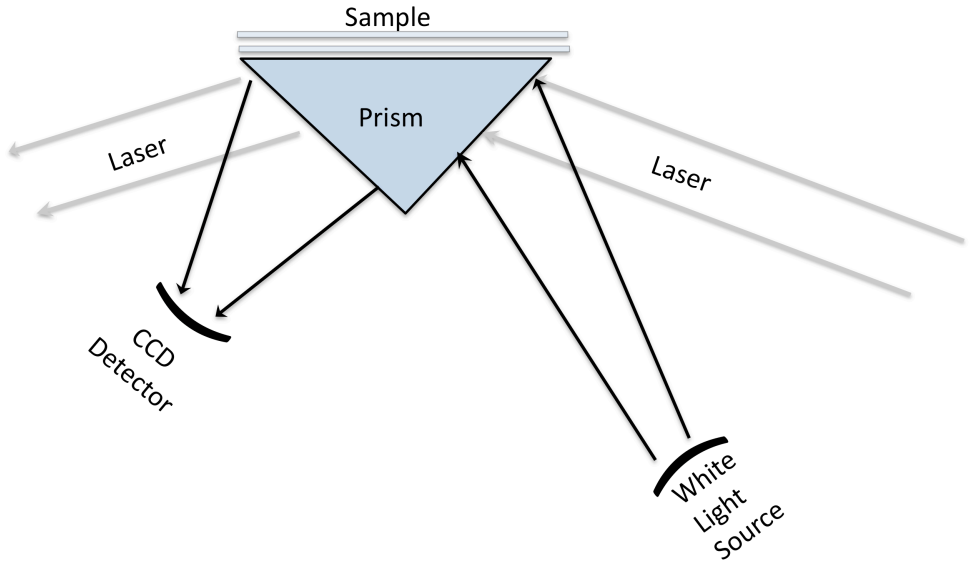

Figure 3.5 Schematic of the white light probe beam configuration used to monitor the development of the Bragg grating in real-time.

The beam incident angle is tuned so that the reflection peak is far enough into the red portion of the spectrum so that a low-pass, band-edge filter can be used to ensure that the probe beam does not contribute to the photo-initiation reaction. In order to develop a complete a picture as possible, the same formulations used for the RTIR experiments were repeated to assist in understanding the dynamics of grating development. All experiments were run at 150 mW/cm^2 at the sample. In this setup, the computer simultaneously un-shutters the holography laser and initiates recording of the white-light spectra every 3 milliseconds. This spectrum is then curve fit to find both the maximum intensity and the frequency at maximum intensity. Figure 3.6 plots the evolution of the normalized maximum intensity over

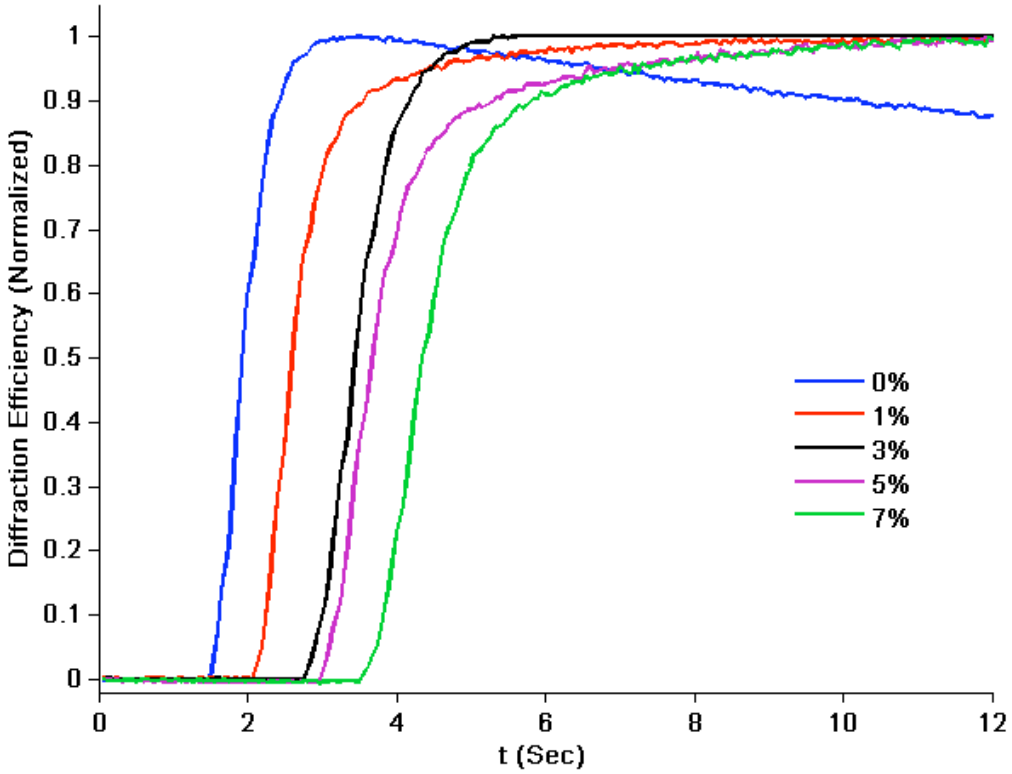

Figure 3.6 Evolution of reflection grating diffraction efficiency over time for thiol-ene formulations containing MPTMS-functionalized SiO_2 nanoparticle weight fractions of 0, 1, 3, 5 and 7. Data is normalized by the maximim diffraction efficiency (71%) so that consistent comparisons between the data are made.

time for syrups containing the same 0, 1, 3, 5 and 7 wt% of functionalized nanoparticles. As shown in Figure 3.6, a surprising result is that onset of grating formation is delayed in a linear fashion. For acrylate systems, we would first suspect oxygen inhibition, but thiol-ene systems are not inhibited by oxygen *[5]*. We now assert that this could be explained by two different physical mechanisms. The first is that the increased loadings of nanoparticles increase viscosity, slows diffusion and hence delays the time to phase separation. The second is that the high loadings of nanoparticles lead to confinement effects that change the phase diagram of the system and lead to increased solubility. Also note on graph that the diffraction efficiency of the control syrup shows a rapid rise to a maximum and then begins to slowly decline. This has been observed in the literature as a condition of

overexposure, where the effects of the reaction rate are larger than the effects of the diffusion rate*[18]*. When this occurs, the polymer distribution becomes increasingly non-sinusoidal due to build up of the reacted polymer that has not yet diffused. Then at longer times, diffraction efficiency decreases due to development of scatter and the reduction in refractive index differences due to continued slow diffusion of the polymer into the dark regions. Figure 3.7 illustrates the change in peak position at maximum intensity for the same data set.

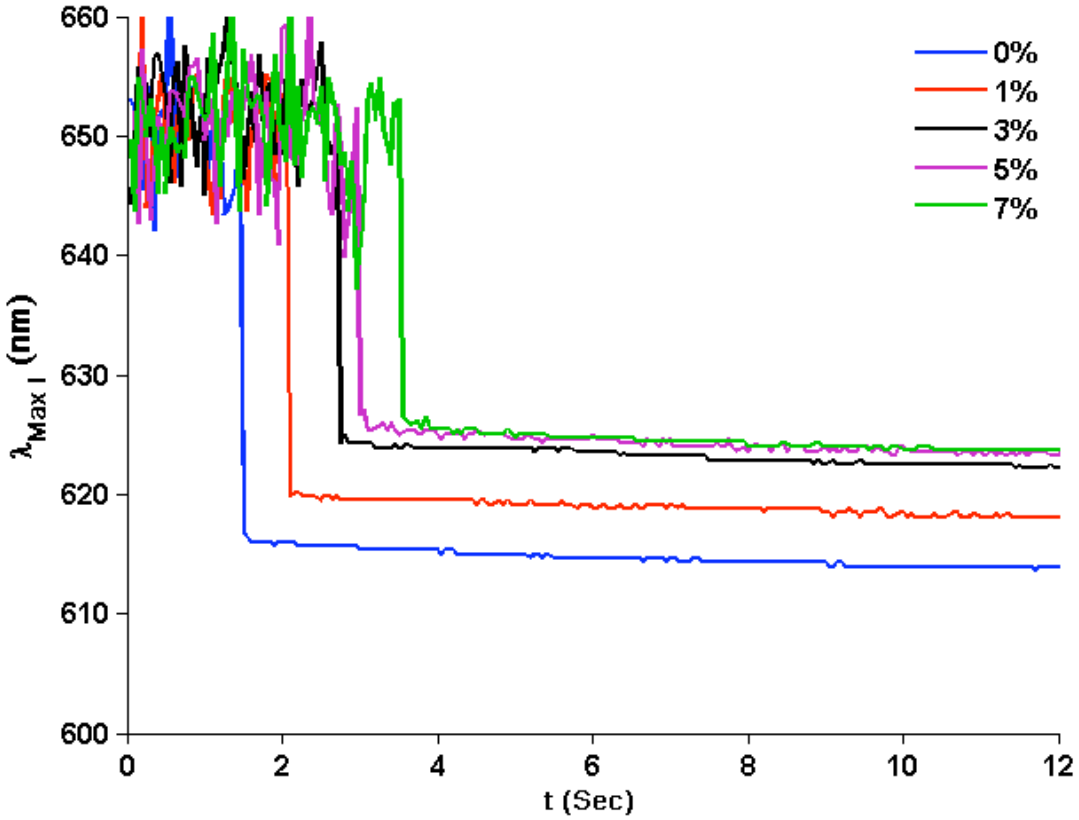

Figure 3.7 Evolution in the peak position of the reflection peak maximum over time during formation of a Bragg reflection grating. The noisy data at early times is due to output of curve-fit algorithms before the appearance of the reflection grating.

The relative flatness of the data presented in Figure 3.7 illustrates that the majority of cure shrinkage occurs before grating formation, which we are assuming occurs primarily at phase separation. In this fashion, most shrinkage occurs in the liquid state and no significant stresses are built up in the system. Also, for 1-3 wt% loadings of nanoparticles the exhibit less blue shift, which indicates that the total level of cure shrinkage is reduced by the addition of nanoparticle. We theorize that a mechanical structure is developed which resists compression. As this structure becomes more robust, additional loading of nanoparticles has little added effect.

3.4 Chapter Summary

Thiol-ene polymers have multiple advantages of multi-functional acrylates for use in HPDLC formulations. For the purpose of enhancing the transport of nanoparticles, delayed gelation due to the step-growth polymerization mechanism is expected to maximize diffusion time for nanoparticle transport. MPTMS-functionalized SiO_2 nanoparticles were added into NOA 65 formulations and maintained good dispersion and segregation in the polymer domain at loadings up to 20 wt% (for this system, this equals 15 vol% in the polymer domain). HPDLC grating diffraction efficiencies were maintained up to 10 wt% loadings an ~30% reduction in switching voltage was noted as well.

In attempt to begin to understand system parameters, RTIR was used to quantify polymerization rates for HPDLC NOA 65 formulations. Addition of nanoparticle did not exhibit the expected reduction in polymerization rate, and the rate even was slightly accelerated for volume nanoparticle loadings higher than 5

wt%. This indicated that for the given exposure conditions, that the system was not diffusion limited.

Lastly, real-time evolution of grating efficiencies was monitored during growth by adding a white light probe to the holographic process. Here, an increase in nanoparticle loading caused a delay in grating formation. This was attributed to either an increase in viscosity delaying phase separation, or confinement due to the nanoparticle changing the phase diagram such that solubility was increased. Peak position measurements during holography also indicated that the amount of cure shrinkage was decreased by the addition of reactive nanoparticle up to 5 wt%. Above this level, increasing nanoparticle loading had little effect.

3.5 References

[1] T. J. White, L. V. Natarajan, V. P. Tondiglia, P. F. Lloyd, T. J. Bunning, C. A. Guymon, *Macromolecules* **2007**, *40*, 1121.

[2] L. Natarajan, J. Klosterman, V. P. Tondiglia, R. L. Sutherland, P. F. Lloyd, T. J. Bunning, "Effect of adding a multifunctional acrylate on the electro-optical properties of reflection gratings formed by thiol-ene photopolymerization", presented at *Optical Materials in Defence Systems Technology*, London, United Kingdom, **2004**.

[3] L. V. N. T. J. Bunning, V. P. Tondiglia, G. Dougherty, R. L. Sutherland,, *Journal of Polymer Science Part B: Polymer Physics* **1997**, *35*, 2825.

[4] R. L. Sutherland, V. P. Tondiglia, L. V. Natarajan, P. F. Lloyd, T. J. Bunning, *Journal of Applied Physics* **2006**, *99*, 123104.

[5] B.-S. Chiou, R. J. English, S. A. Khan, *Macromolecules* **1996**, *29*, 5368.

[6] L. V. Natarajan, C. K. Shepherd, D. M. Brandelik, R. L. Sutherland, S. Chandra, V. P. Tondiglia, D. Tomlin, T. J. Bunning, *Chemistry of Materials* **2003**, *15*, 2477.

[7] V. P. Tondiglia, R. L. Sutherland, L. V. Natarajan, P. F. Lloyd, T. J. Bunning, *Opt. Lett.* **2008**, *33*, 1890.

[8] R. L. Sutherland, V. P. Tondiglia, L. V. Natarajan, J. M. Wofford, S. A. Siwecki, G. Cook, D. R. Evans, P. F. Lloyd, T. J. Bunning, "Liquid crystal Bragg gratings: dynamic optical elements for spatial light modulators", presented at *Emerging Liquid Crystal Technologies II*, San Jose, CA, USA, **2007**.

[9] T. J. Bunning, L. Natarajan, V. P. Tondiglia, R. L. Sutherland, "Effect of gel-point versus conversion on the real-time dynamics of holographic polymer-dispersed liquid crystal (HPDLC) formation", USA, **2003**.
[10] Q. Li, H. Zhou, D. A. Wicks, C. E. Hoyle, *Journal of Polymer Science Part A: Polymer Chemistry* **2007**, *45*, 5103.
[11] A. F. Senyurt, H. Wei, B. Phillips, M. Cole, S. Nazarenko, C. E. Hoyle, S. G. Piland, T. E. Gould, *Macromolecules* **2006**, *39*, 6315.
[12] S. K. Reddy, N. B. Cramer, M. Kalvaitas, T. Y. Lee, C. N. Bowman, *Australian Journal of Chemistry* **2006**, *59*, 586.
[13] T. Y. Lee, Z. Smith, S. K. Reddy, N. B. Cramer, C. N. Bowman, *Macromolecules* **2007**, *40*, 1466.
[14] T. Y. Lee, J. Carioscia, Z. Smith, C. N. Bowman, *Macromolecules* **2007**, *40*, 1473.
[15] T. Y. Lee, C. N. Bowman, *Polymer* **2006**, *47*, 6057.
[16] C. Carre, D. J. Lougnot, J. P. Fouassier, *Macromolecules* **2002**, *22*, 791.
[17] R. L. Sutherland, L. V. Natarajan, V. P. Tondiglia, T. J. Bunning, *Chemistry of Materials* **1993**, *5*, 1533.
[18] V. L. Colvin, R. G. Larson, A. L. Harris, M. L. Schilling, *Journal of Applied Physics* **1997**, *81*, 5913.

CHAPTER 4

CHARACTERIZATION OF FUNCTIONALIZED SILICA NANOPARTICLES AND THE IMPLICATIONS FOR HANDLING AND USE IN NANOCOMPOSITES

4.1 Introduction

Over the course of synthesis and characterization of Methacryloxypropyl-trimethoxysilane (MPTMS) functionalized silica nanoparticles, it was experimentally observed that when a high concentration of MPMTS was used in the functionalization process, the resultant functionalized particles maintained a liquid-like state upon drying at room temperature, essentially forming a solventless nanofluid. The question that arises from this observation is whether it is a one-component or two-component fluid. If the corona of the functionalized particle has continued to grow from a hydrolysis and condensation reaction, then the covalently bound corona, through an unknown mechanism, imparts liquid-like properties to the particles and is in essence a single component fluid. However, it is also possible that residual MPTMS retained in solution after functionalization forms oligomers, which absorb onto the surface of nanoparticles, forming a large physisorbed corona. In this case the liquid properties observed would be from a two-component fluid. Several groups have observed and explored similar phenomenon. Luedtke and Landman used MD calculations in 1996 to predict that Au nanoparticles, passivated with long chain alkanethiols, take on ordered structures based on the passivating material and would undergo a melting transition upon heating *[1]*. This was followed by experimental observation of a melting transition for an Au-alkylthiol system and for an Ag-alkylthiol system by Sandhyarani et. al. in 2000 *[2]*. In 2003,

Fujii reported synthesis of layered alkylsilanes with organic modifiers that demonstrated a melting transition *[3]*. However, the material contained a large degree of unreacted silanol groups, which quickly reacted at temperature, converting the melt into an amorphous solid. Giannelis reported a layered nanoparticle structure with a reversible melting transition that was based upon the controlled condensation of octyldecyltrichlorosilane (OTS) *[4, 5]*. Giannelis has used covalent bonding of a charged silane species to the surface of silica nanoparticles to obtain nanoparticles functionalized with long-chain organic salts. These nanoparticles have been observed to maintain liquid-like properties upon drying. Using similar processes, these results have been extended to ZnO *[6]*. Star polymers with a large number of arms begin to have colloidal properties and may be used as an analogous system to stimulate understanding of the system properties of a one or two component nanofluid *[7]*.

4.2 Synthesis and Proposed Mechanism

To assist in understanding the observation of fluid properties in our nanoparticle system after complete removal of the ethanol solvent, functionalized silica nanoparticles were prepared using three different concentrations of MPTMS and compared to unfunctionalized silica nanoparticles as a baseline. The silica nanoparticles were synthesized by adding 500 mL of 200 proof ethanol (Aldrich) to a 1-liter round bottom flask with vigorous stirring using a Teflon coated magnetic stir bar. Ammonium hydroxide (28% solution, Aldrich) and de-ionized water were added to the stirring ethanol in the concentrations listed in Table 1.2. The solution

was stirred for 10 minutes before the rapid addition of tetraethoxysilane (TEOS, Geleste). The resultant solution was allowed to stir at room temperature for 24 hours before being divided into 4 equal aliquots. The first aliquot was set aside for later cleaning without functionalization. The remaining 3 aliquots were added to individual 250 mL round bottom flasks and stirred with magnetic stir bars. To arrive at the quantities, it was assumed that the density of hydroxyl groups on the surface of the silica nanoparticles was 2 groups per nm^2 *[8]*. Using 28 nm as the average diameter of the nanoparticles, the total surface area was used to determine the amount of MPTMS needed for 100% conversion of surface hydroxyls to functionalized silane groups (ignoring the steric hindrances of the hydroxyl groups by the characteristic diameter of the MPTMS). The amount of MPMTS used in experiments in Chapter 2 was typically 15 times this stiochiometric amount to ensure good coverage, which led to a powder upon cleaning by dialysis and drying. Here we exceeded the amount needed to stoichiometrically convert the hydroxyl groups by large excesses, specifically 40x, 75x and 112x, which leads to molarities of MPTMS of [.084], [.151], and [.236], respectively. These numbers were arrived at by empirically searching for the concentrations that lead to liquid-like qualities in the dried particles after cleaning. After stirring for 24 hours, all 4 aliquots were cleaned via 4 exchanges in a dialysis membrane (Fisher, 12,000-14,000 molecular weight cut-off) using 200 proof ethanol. After cleaning, the solvent was removed from the samples using a Buchi R-215 rotary evaporator followed by 12 hours under vacuum (1 mbar). The optical photograph in Figure 4.1 illustrates the change in physical properties of the dried particles with respect to increasing concentration of MPTMS.

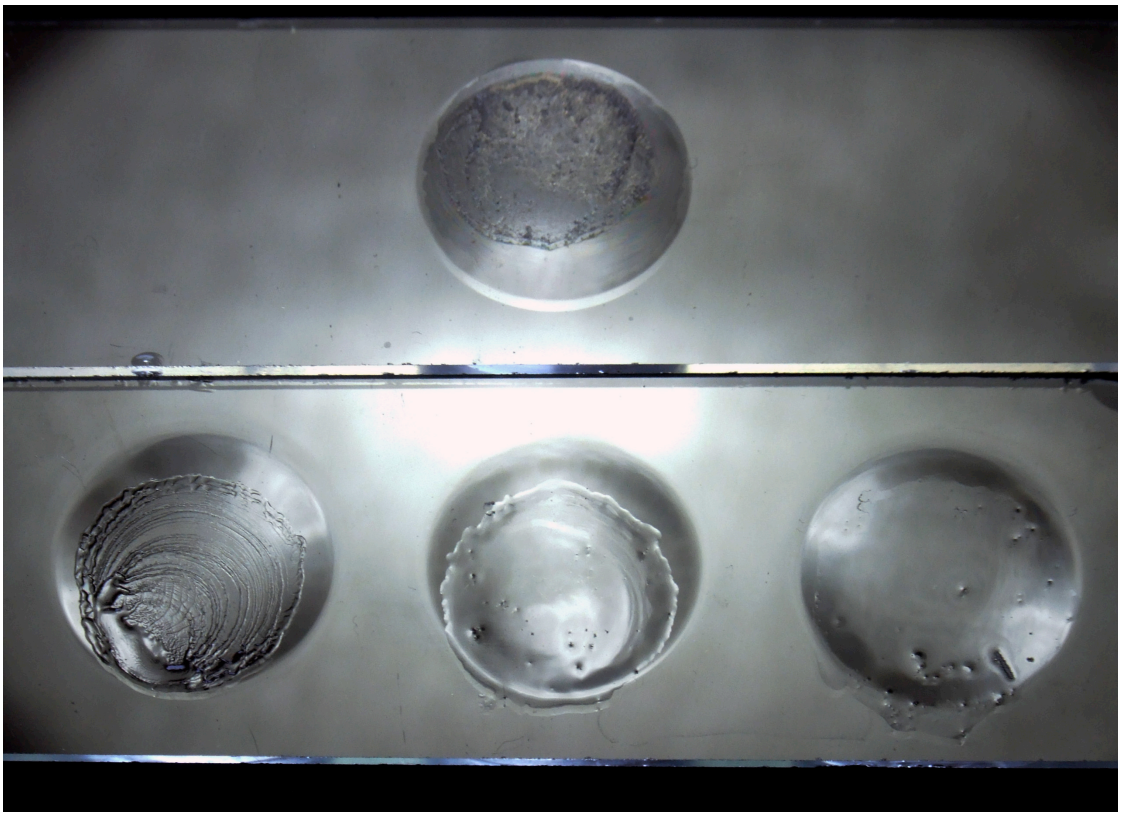

Figure 4.1 Optical photograph of dried SiO_2 nanoparticles. The top slide contains unfunctionalized particles, while the bottom slide contains nanoparticles functionalized using increasing concentrations of MPTMS. From left to right the concentrations of PTMS are [.084], [.151] and [.236],respectively (the black inclusions are dust particles).

As seen in picture, the dried, cleaned particles move from a dry powdery film (unfunctionalized) through a waxy liquid phase to a liquid that flows with a honey-like viscosity of honey at a molarity of [.236] MPTMS in the reacted Stöber solution.

4.3 Thermogravimetric Analysis of MPTMS functionalized Silica Nanoparticles

To begin to understand the change in the physical character of the dried nanoparticles as a function of MPTMS concentration, thermogravimetric analysis (TGA) was performed on all of the dried particle samples. The tests were performed using a TA Instruments TGA Q5000 equipped with an IR furnace. Each sample was run in air with a 25 mL/min flow rate. Each run started with a 20 minute isothermal

hold at 25°C followed by a temperature ramp of 10°C/min from 25°C to 850°C. The resultant data are displayed in Figure 4.2. For the sample containing the unfunctionalized nanoparticles the loss is mass before 250°C is approximately 4 %, which can be attributed to residual solvent and/or adsorbed water. The remaining loss indicates that the unfunctionalized particles are comprised of 7 % organic matter or reactive hydroxyl groups, either in the interior of the particle or adsorbed onto the surface. Examining the rest of the traces in Figure 4.2 we can see that all of the samples have roughly the same loss before250°C and increasing amounts of loss between 250°C and 850°C. Assuming that the 7% loss of the unfunctionalized particles indicates the amount of organic/reactive inclusions in all of the nanoparticles, the TGA analysis indicates that the corona of the nanoparticle contains 21%, 38% and 46% organic matter by weight for MPTMS functionalizations of [.084], [.151], and [.236], respectively. Additionally, the relative lack of variation in mass loss prior to 250°C would also appear to indicate that the fluidity observed in Figure 4.1 is not due the presence of residual solvent.

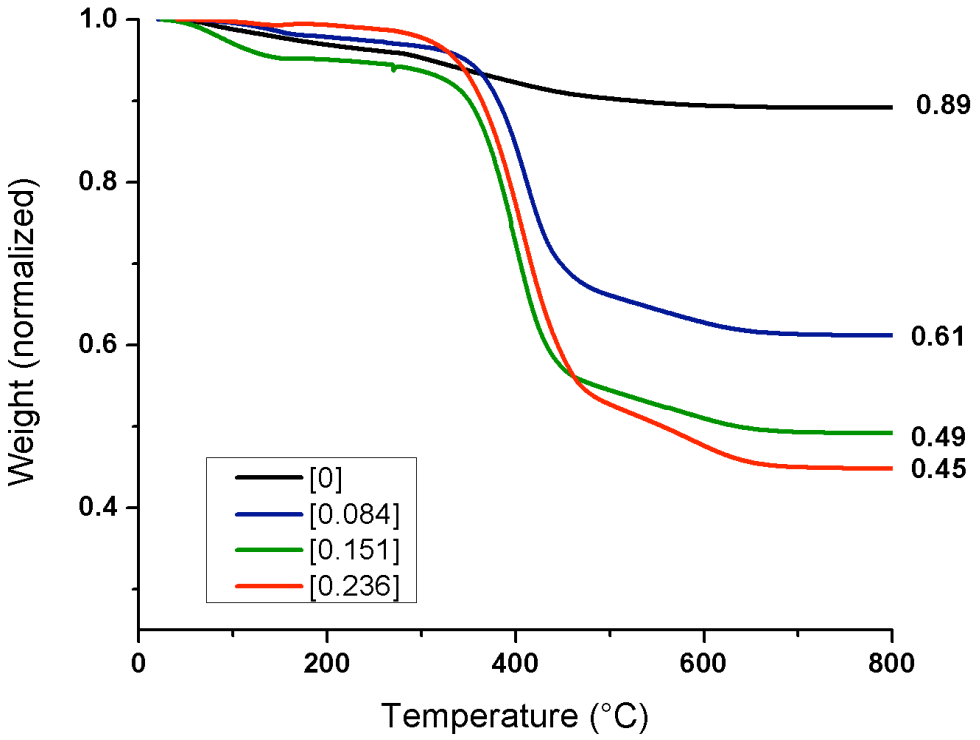

Figure 4.2 TGA of same samples of dried in Figure 4.1. TGA was conducted in air with a 10°C/min heating rate. Legend indicates the concentration of MPTMS used to functionalize the samples.

4.4 Nuclear Magnetic Resonance of MPTMS Functionalized Silica Nanoparticles

Nuclear magnetic resonance (NMR) spectroscopy is a powerful tool for the identification of chemical species and their corresponding structure. Here we use NMR help understand the chemical nature of the observed corona. ^{1}H NMR is used to determine that there are no free molecules of MPTMS remaining in the dried nanoparticles. A portion of the [.236] functionalized silica nanoparticles were dried using the same approach as mentioned in the section above, then re-dispersed in d-THF. The ^{1}H NMR spectra for the particles were taken twice, the first time as

prepared and the second time with a small amount of added MPTMS. The resultant data displayed in Figure 4.3 compares the proton spectra of the modified silica in the absence and presence of the surface-modifying methacrylate. In the blue trace, the pertinent features are the broad line for the methylene protons nearest the silica surface (0.8 ppm). Note that the methylene protons nearest the silicon shift from 0.7 to 0.8 ppm in the presence of the nanoparticles. Because there is a clear chemical shift difference between the two samples, these data show that any

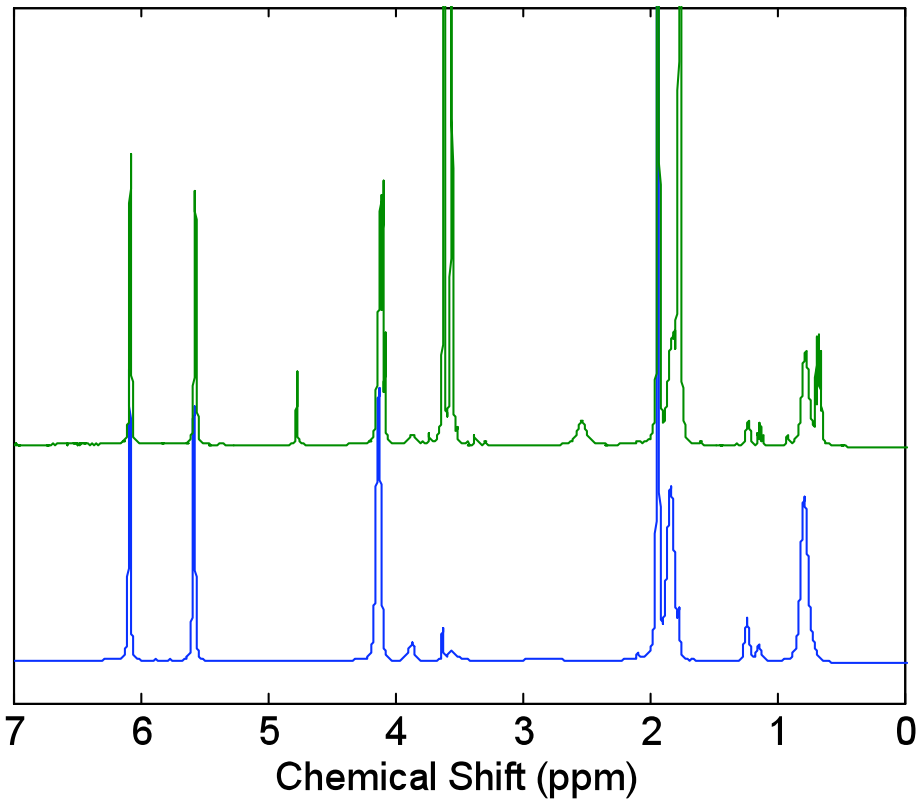

Figure 4.3. Comparison of the proton spectra for the 28 nm silica nanoparticles modified with MPTMS (blue) and the same sample with MPTMS added directly to the THF solution (green).

residual hydrolyzed MPTMS has been removed from the nanoparticle sample by the dialysis procedure used for cleaning.

To help determine the chemical nature of the nanoparticle corona created by the functionalization, solid-state, ^{29}Si NMR is utilized. In silicon NMR, the silicon chemical shift depends on the number of Si-O-Si bonds. For silicon structures with only Si-O bonds the chemical shifts are approximately:

- Q^2: -91 ppm
- Q^3: -101 ppm
- Q^4 : -111 ppm

For silicon bonded to a single carbon atom the chemical shifts are approximately:

- T^2: -57 ppm
- T^3: -67 ppm

Schematics of the chemical structures corresponding to these peaks are displayed in Figure 4.4. The silicon relaxation times can be very long, so special consideration must be given to quantitative spectra. The three pulse sequences in solids are*[9]*:

- 1-pulse—quantitative using very long relaxation delays and reduced angle pulses

• Cross Polarization—this pulse sequence methodology has good sensitivity, but is not quantitative. The signals are enhanced for those silicon atoms near protons (i.e. Q^2 and Q^3).

• Saturation Recovery—measures the signal recovery following saturation. This sequence is used to measure the relaxation times. This method was used to ensure sufficient time had passed between acquisitions so that all data were quantitative.

Quantitative 1-pulse spectra were obtained using the Ernst equation,

$$\cos(\alpha) = e^{-\frac{t}{T_1}} \tag{4.1}$$

where α is the pulse tip angle, t the time between experiments and T_1 the spin-lattice relaxation time. In the solid-state experiments used in this chapter, $\alpha=45^o$ and t=280 s, yielding quantitative spectra for samples with relaxation times shorter than 400s.

Performing solid-state, ^{29}Si NMR on both the unfunctionalized nanoparticles and the nanoparticles functionalized with [.236] MPTMS resulted in the spectra displayed in Figure 4.5. Reactions of Q^3 site (hydroxyl groups) with MPTMS converts them to Q^4 sites, changing the Q^3:Q^4 ratio, and indicating successful functionalization. As seen in Table 4.1, the Q^3:Q^4 ratio changes from 0.72 : 1 to 0.3 : 1, indicating that approximately 60% of the Q^3 sites have been converted to Q^4 sites. Integrating the T^2 +T^3 sites and the Q^3 +Q^4 sites gives us the ratio of silicon molecules in the nanoparticle versus the silicon derived from molecules of MPTMS. Using the data from Figure 4.5, this ratio is 1:0.94 (for the [.236] sample).

Due to the changing physical nature of the samples and due to the increasing organic content evidenced in the TGA data, it can be deduced that the corona surrounding the nanoparticle increases with increasing MPTMS concentration. NMR can help understand whether this growth mechanism is due to a continued condensation reaction with the silicon atoms in the MPTMS, or by polymerization of the methacrylate functional group on the MPTMS. Table 4.2 displays both calculated and observed peak values for the proton NMR data displayed in Figure 4.3 with the peak assignments for the MPTMS molecule displayed in Figure 4.4a. Reaction of the methacrylate group would change the relative intensities of the double-bonded protons relative to the propyl proton intensities. The table shows NO change in intensity relative to the propyl protons in the modified NP, indicating that the methacrylate group is largely intact. Because of this, we can eliminate methacrylate polymerization as the growth mechanism for the corona. This provides evidence that corona is comprised of siloxane chains (probably cross-linked) surrounded by organic groups.

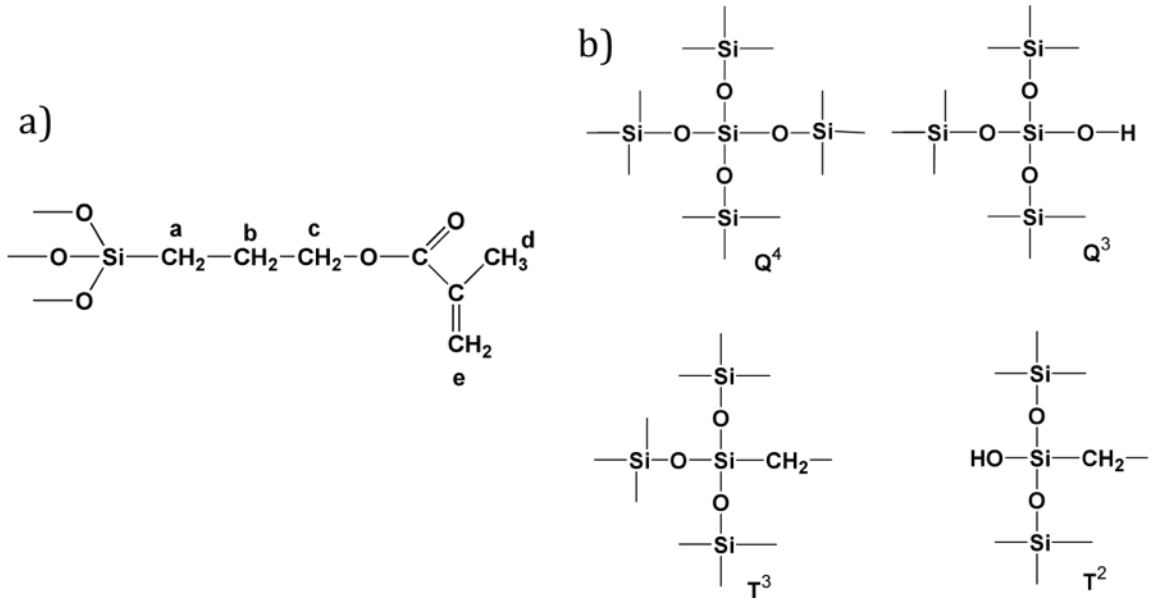

Figure 4.4 Schematic illustrating a) peak assignments for MPTMS using proton NMR, and b) the corresponding molecular structure of relevant peaks for ^{29}Si solid-state NMR.

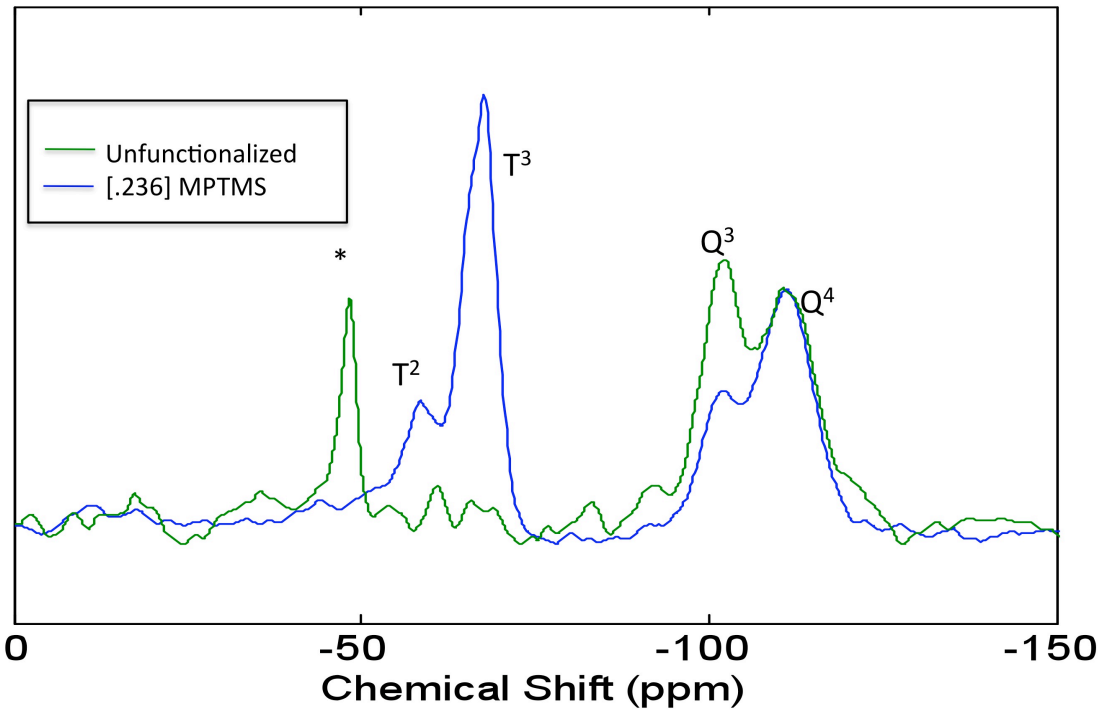

Figure 4.5 ^{29}Si NMR spectra of unfunctionalized and MPTMS functionalized silica nanoparticles. Concentration of MPMTS functionalized sample is [.236]. Starred peak is attributed to a background peak from the probe and should be ignored.

Table 4.1 Tabulated solid-state ^{29}Si NMR data for the same samples in Figure 4.5 T_1 times were measured using a saturation recovery pulse sequence

Sample	Q^3 peak	Q^4 peak	$T_{1,Q3}$(s)	$T_{1,Q4}$(s)
Unfunctionalized SiO2 NP	.58	.42	61	315
SiO2 NP functionalized w/ [.236] MPTMS	.23	.77	33	46

Table 4.2 Proton NMR data for [.236] MPTMS sample—tabulated from the spectra displayed in Figure 4.3 Peak assignments are displayed in Figure 4.4

Peak	d_H (ppm)	I(obs)	I(calc)
c	4.1	1.95	2.00
e1	6.1	1.00	1.00
e2	5.6	0.98	1.00
a	0.7	2.06	2.00

4.5 Small Angle X-Ray Scattering from MPTMS Functionalized Silica Nanoparticles

Small angle x-ray scattering (SAXS) is useful for inferring physical size, size distribution, and packing structure (crystallography) of nanoparticles []. SAXS spectra of the same samples used for TGA analysis were taken in both dried state and in the un-dried ethanol solution. SAXS data were taken on a Rigaku UltraX 18FB with a sample to detector distance of 1.27 m using power of 45 kV and 60mA and copper Kα radiation line at 1.54 angstroms. SAXS spectra were taken using the same samples used throughout this chapter—Sample A, unfunctionalized silica nanoparticles; Sample B, silica nanoparticles functionalized with MPTMS at [.084]; Sample C, silica nanoparticles functionalized with [.151] MPTMS; and Sample D, silica nanoparticles functionalized with [.236] MPTMS. SAXS spectra of these cleaned samples in the dilute ethanol solution (never dried) are presented in Figure 4.6. Because of the dilute solution, the spectra display minimal interference and the presence of two minima in the spectra indicates that the particles have a narrow sized distribution. Because the spectra of Samples B-D do not shift with respect to the spectra of Sample A, it can be concluded that either the majority of the scattering is coming from the core of the nanoparticles rather from the functionalized shell, or that the corona does not exist, thus providing no additional information about the corona. To quantify these observations, the scattering intensity, I(*Q)* was fit using a standard model for spheres in a dilute solution, given by

$$I(Q) = |\Delta\rho|^2 \int_0^\infty |F(Q,r|^2 V^2(r) NP(r) dr \tag{4.2}$$

where Δρ is the scattering length contrast between the silica spheres and the ethanol, *F(Q,r)* is the scattering form factor, *V(r)* is the volume of the sphere (particle), *N* is the number of particles, and *P(r)* is the probability of a particle of size *r*. The spherical form factor is given as

$$F(Q,r) = \frac{3}{Qr^3(\sin(Qr)) - (Qr\cos(Qr))} \tag{4.3}$$

The volume distribution, *V(r)P(r)*, which was found to best fit the data was log-normal and can be calculated using

$$P(r) = \frac{e^{-(\ln(r-r_{mean})^2/2\sigma^2)}}{(r-r_{mean})\sigma^2\sqrt{2\pi}} \tag{4.4}$$

These equation are used using a least squares fitting routine within IGOR Pro (Wavemetrics) in combination with code implemented by J. Havsky (APS) with the integral in Equation 4.2 replaced by a finite number of bins. There are three adjustable parameters used during the fit: r_{mean}, *N* and σ. The parameter r_{mean} is the mean particle radius, and affects the position of the minima in the oscillations, while N is directly proportional to the intensity. The shape parameter, σ, is equivalent to the polydispersity in the system. Figure 4.7a repeats the SAXS spectra for Sample A in an ethanol solution along with the associated curve fit and residuals. A good curve fit was found using r_{mean} of 14.45 nm and a shape parameter, σ, of .15 (narrow). This fit is plotted in Figure 4.7b.

SAXS spectra were also taken of Samples A-D that were dried using the same procedure outlined in section 4.2. These spectra are presented in Figure 4.8. As seen in the figure, the oscillations shift to lower Q vectors with increasing functionalization, until the spectra from Sample D no longer evidence in packing structure, but rather a broad curvature indicative of a glassy liquid. With the exception of sample D, the data was fit well with an interference form factor corresponding to FCC packing, and the resultant diameters were as delineated in the Table 4.3. In the figure, the measured diameter of the unfunctionalized particles was used as a baseline to calculate the corona thickness for the MPTMS concentrations of Samples B and C. Sample D could not be calculated due to the lack of structure. Corona thickness for each sample are also listed in Table 4.3.

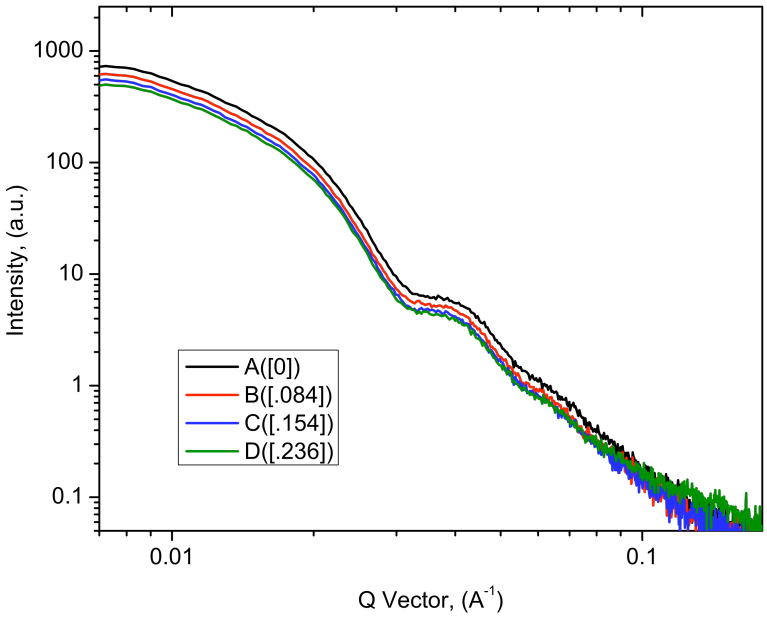

Figure 4.6 SAXS spectra of Samples A-D in a dilute ethanol solution. The numbers in brackets indicate the MPTMS molarity used in the Stöber solution for functionalization.

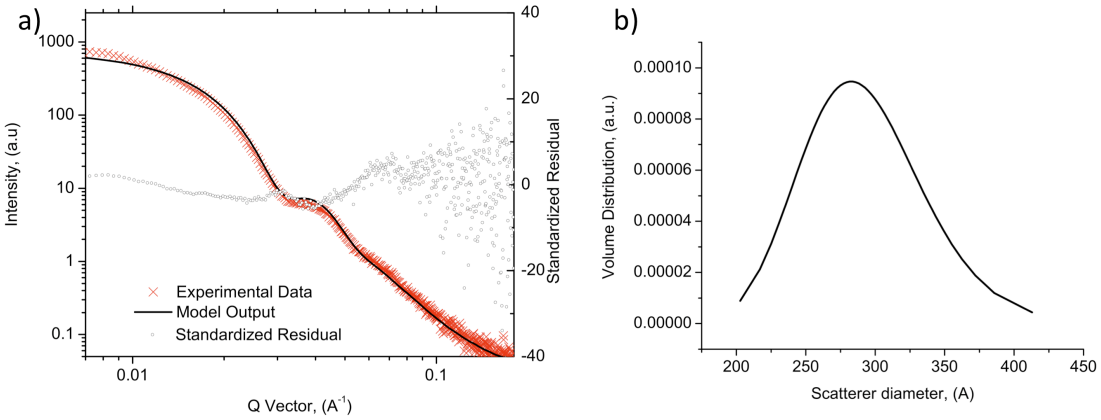

Figure 4.7 a) SAXS spectra superimposed with calculated fit of the unfunctionalized nanoparticles of sample A(in ethanol). b) Corresponding model distribution from calculated fit. Mean particle distribution is 28.9 nm.

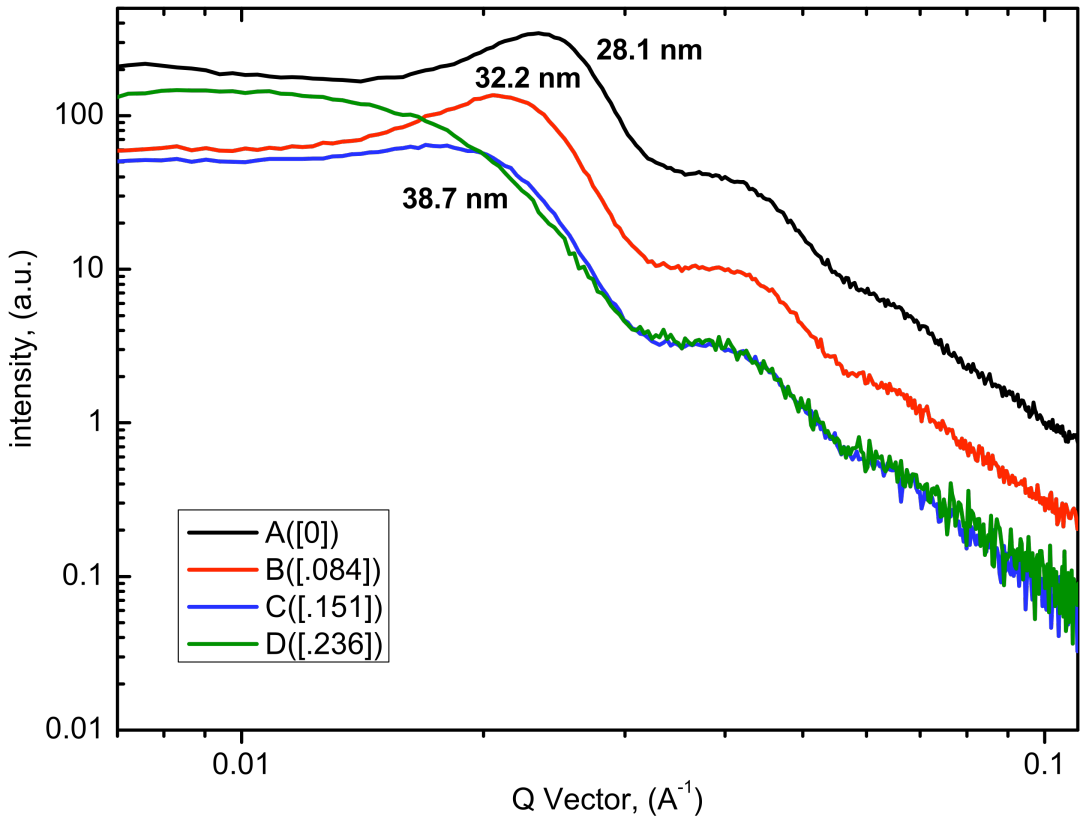

Figure 4.8 SAXS spectra of Samples A-D after drying. Data was curve fit using a interference factor corresponding to FCC packing in order to find listed particle-to-particle distaces for each spectra.

Table 4.3 Calculated diameters and corona thicknesses from SAXS spectra in Figure 4.8. Sample D could not be calculated because of the lack of structure peak in the specta

Sample	Nanoparticle Diameter (Calculated from FCC fit)	Calculated Corona Thickness (using Sample A as baseline)
A (unfunctionalized)	28.1 nm	N/A
B ([.084] MPTMS)	32.2 nm	2.05 nm
C ([.151] MPTMS)	38.7 nm	5.3 nm
D ([.236] MPTMS)	--	--

4.6 Transmission Electron Microscopy Analysis of MPTMS Functionalized Silica Nanoparticles

Figure 4.9 presents a TEM micrograph of nanoparticles from Sample B. To prepare the sample for TEM analysis one drop of the nanoparticles in ethanol solution was drop-cast onto a TEM grid coated with a 10 nm thick film of amorphous carbon. TEM anaysis was performed on a Phillips CM200 using a LaB_6 filament and an acceleration voltage of 200 kV. Examination of Figure 4.9a reveals a monolayer of particles clustered by the evaporative process. These particles, as is typical of Stöber particles in this size range, are roughly spherical with some degree of polydispersity. No corona is evident in the micrograph, possible indicating that the mass-thickness contrast of a semi-organic corona is not sufficient to be visible using traditional bright-field TEM. An optical analysis of the size distribution of the nanoparticles was performed using the ImageJ software developed at the National Institutes of Health. The TEM image was adjusted to a binary image using the built-in threshold and watershed separation tools along with visual adjustment. The outlined particles in Figure 4.9b illustrate the results of the image modifications which are used as the basis for analysis of the particle size distribution. The polydispersity of a system, σ, is given by the standard deviation of a property divided by the mean value of the property, or

$$\sigma = \frac{\delta}{\langle \varepsilon \rangle} \qquad (4.5)$$

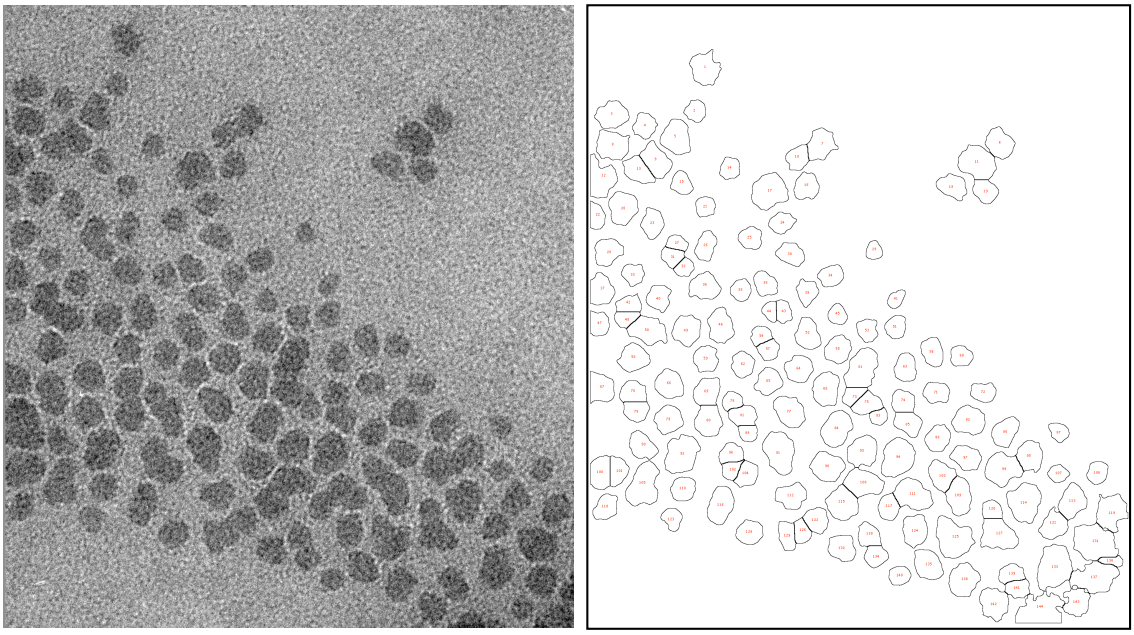

Figure 4.9 a) TEM micrograph of SiO2 nanoparticles functionalized with [.084] MPTMS and dried from solution on an amorphous carbon coated TEM grid. b) Particle outline of same image using a binary threshold in ImageJ software. The image is the basis of the optical analysis of particle diameters presented in the text.

where, in this case, δ is the standard deviation in the distribution of diameters and $\langle \varepsilon \rangle$ is the mean diameter of the nanoparticles. The ImageJ function, analyze particles, was used to determine the Feret diamater of each of the thresholded particles shown in Figure 4.9b. The Feret diameter is the largest chord distance across the circumference of the particle—as such it overestimates the average diameter somewhat for particles that are not perfect spheres. The distribution of particles in the figure yields a mean diameter of 28.9 nm with a standard deviation of 4.94. This yields a polydispersity of σ=.14, or 14%.

To gain a better understanding of the amount of corona that is present, a low-voltage tranmission electron microscope (LV-TEM) from DN American was used. At low voltages, as shown in Figure 4.10, the mass-thickness contrast is considerably

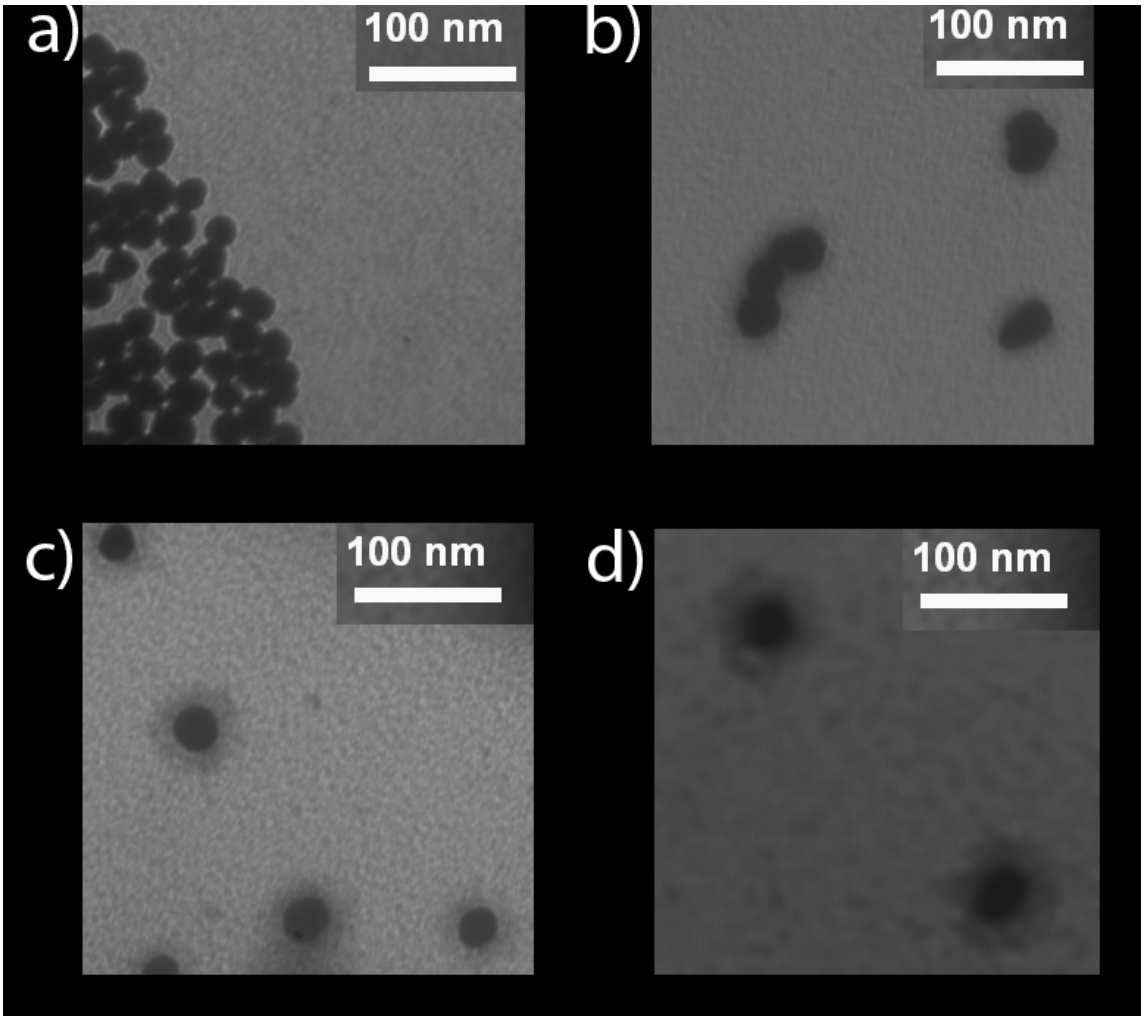

Figure 4.10 Low voltage TEM images of SiO_2 nanoparticles functionalized with increasing molarities of MPTMS. Images display an increasing thickness of lower density corona around the nanoparticles. a) Sample A: Unfunctionalized, b) Sample B: [.084] MPTMS, c) Sample C: [.151] MPTMS, d) Sample D: [.236] MPTMS

enhanced from high voltage machines, allowing thin-layers of organic to be visible in the resultant LV-TEM images. Figure 4.10 displays a series of LV-TEM images based upon Samples A-D, which have samples with increasing amounts of MPTMS functionalization. As can be seen in Figure 4.10a, the unfunctionalized particles show no evidence of a low-density corona (as expected). Careful examination of Figure 4.10b, shows a small evidence of a low density corona, but the corona does not appear to be uniform or consistent from particle to particle, which implies either inhomogeneous growth or that oligomers formed in solution are adsorbing onto the surface of the particles. However, as you progress to the nanoparticles in Figure

4.10c-d an increasing thickness of low-density corona (lighter color in the mass-thickness contrast) is clearly visible.

While the low voltage TEM images of Figure 4.10 clearly demonstrate that a lower density corona exists around the particles functionalized with MPTMS, the images yied no additional information about the chemical composition of the corona. To enhance the understanding of the composition, an EDAX linescan was taken of the functionalized nanoparticles while using the STEM imaging mode of a FEI Titan TEM. As seen in Figure 4.11, there are Si and O peaks in the EDAX linescan corresponding to the nanoparticle. The corona is clearly visible as well, with elevated levels of Si and O with respect to the background.

Because the particle and corona mask the underlying carbon, the C spectra are reduced in the section of the linescan that crosses the particle. Elevated levels of carbon in the corona region (as correlated with the STEM image) with respect to the core region would seem to indicate that there is organic content there as well (the presence of the carbon substrate prohibits any firm conclusions). Overall, the spectra of the corona, when compared to the spectra of the nanoparticle, yields higher carbon content, with lower silicon and oxygen content, which is consistent with what we would expect to find from a low density siloxane structure with intact methacrylate functional groups.

Examining the Si spectra in Figure 4.11b), we can infer that the nanoparticle is approximately 30 nm is diameter with corona thickness of approximately 20 nm.

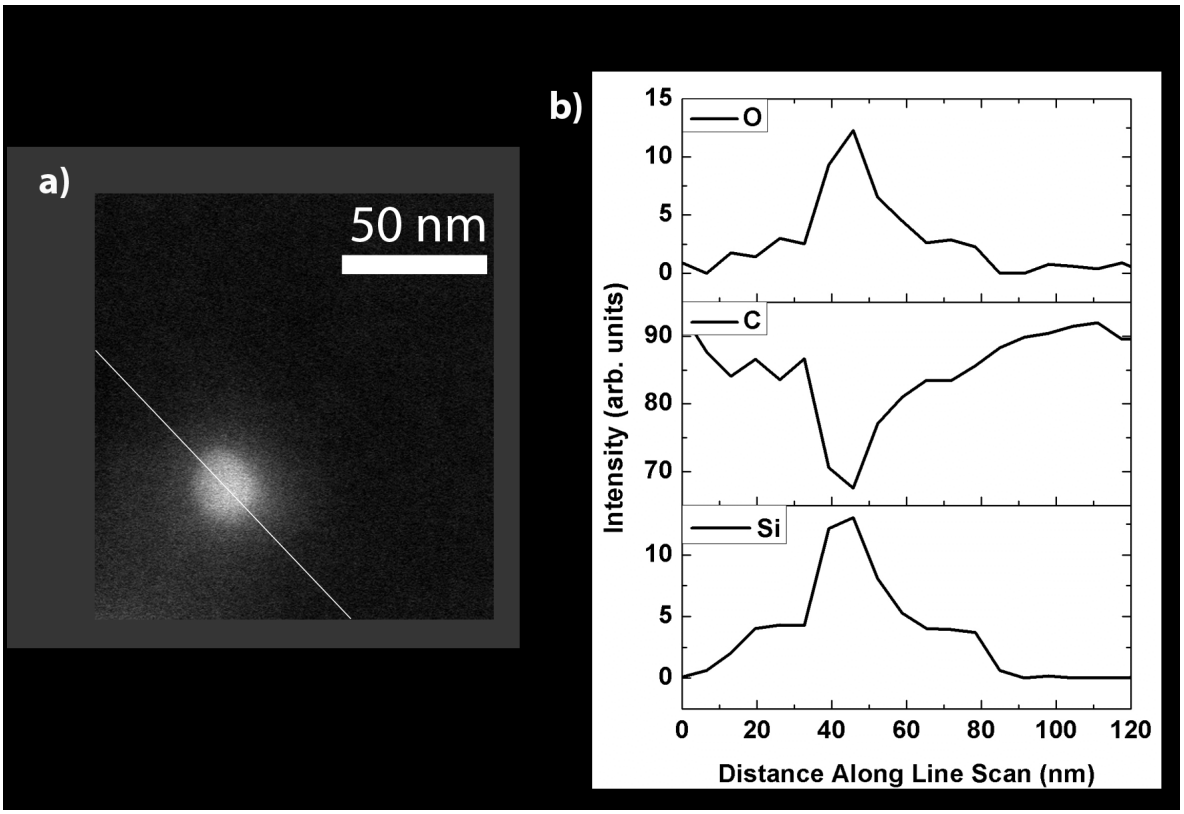

Figure 4.11 a) STEM image of silica nanoparticle functionalized with [.236] MPTMS. Diagonal line through image indicates location for EDAX scan. b) Si, O and C reduced EDAX data for linescan shown in a).

4.7 GPC Analysis of Solventless Nanofluids

In the previous sections of this chapter, we have shown strong evidence that the corona consists of a low-density siloxane structure. Because the silane monomer is tri-functional, it is reasonable to expect that this low-density, siloxane structure contains cross-links. However, there are two reasonable scenarios for the growth of the corona. The first is nanoparticle surface initiated hydrolysis reaction that extends the covalent bonding beyond a monolayer. This scenario would result in the nanofluid containing only one component, which could be considered a

"nanoparticle liquid." The second scenario would entail the excess MPTMS nucleating in solution to form oligomers, which then physisorb onto the surface of the nanoparticles, leading to a two-part nanofluid upon drying. Because a dialysis membrane with large pores cleans the particles, one would expect that any oligomers formed in the solution would be removed, but it is possible that the oligomers could interact with the dialysis membrane and not pass through the pores.

To assist in understanding which scenario is accurate, the solventless nanofluid samples were eluted through a gel permeation chromatography (GPC) column for analysis, as shown in Figure 4.12. To prepare for the GPC analysis, a small portion of sample D was dissolved into THF at the concentration of .1 mg/ml. Figure 4.12 shows both light scattering and refractive index of the material eluted from the GPC column over time. The light scattering data were detected using a *DAWN EOS* multi-angle light scattering detector with a 690 nm laser excitation. The refractive index detector was an *Optilab DSP* interferometric refractometer. In Figure 4.12a, the refractive index data only shows a single polymeric peak (the two smaller peaks are due to the nanoparticle and the shoulder on the polmeric peak is a solvent effect and should be ignored), which was fit to a Zimm model and found to have a molecular weight of 13,500. This number should be treated as a qualitative descriptor as it was calculated using a differential index of refraction (dn/dc) of .1g/mL, which is an estimated number. Examining Figure 4.12b, we see two separate nanoparticle peaks, with fitted radii of 18.9 and 33.9, respectively. Interpreting this data, we see a large nanoparticle peak that corresponds to

nanoparticles without a corona and a much smaller nanoparticle peak, which corresponds by size to nanoparticles which still retain their corona.

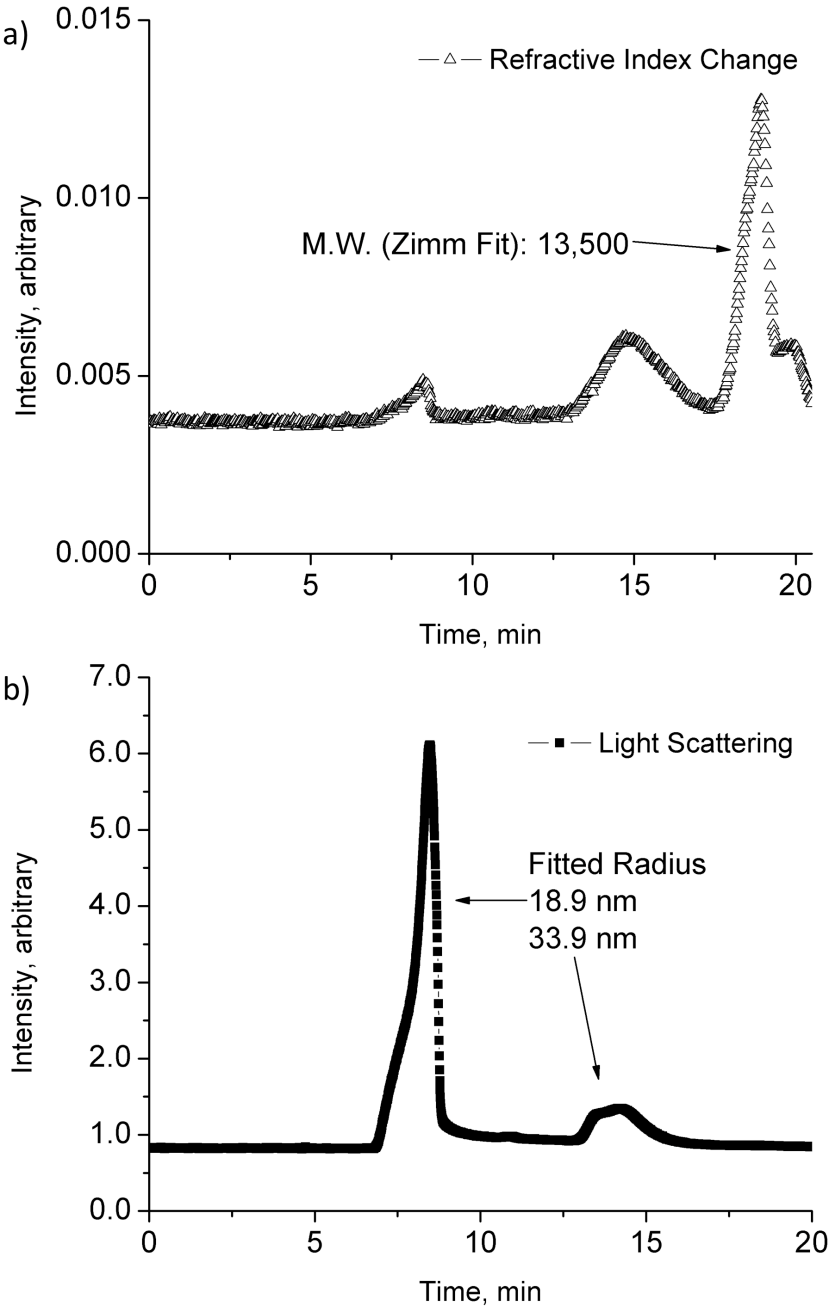

Figure 4.12 GPC data of silica nanoparticles, Sample D, [.236] MPTMS. a) Change in refractive index (from RI of THF) of eluted content versus time, and b) Laser scattering of eluted content versus time.

4.8 Discussion of Nanoparticle Characterization Data

The fact that we see, in the GPC data presented in Figure 4.12, a large, bare nanoparticle peak, combined with a polymeric peak that is eluted later probably indicates that the corona present on the nanoparticle in sample D is physisorbed rather than chemisorbed onto the surface of the nanoparticles. This in turn indicates that the large excess (above what is estimated to be needed to functionalize all of the surface hydroxyls on the nanoparticles) of MPTMS at [.236] is nucleating in solution to form oligomers, which are then absorbed onto the surface of the nanoparticles. All of the characterizations performed upon the dried, functionalized nanoparticles and presented in this chapter, taken in toto, show that when large excesses of MPTMS are used to functionalize the nanoparticles, a low density, siloxane corona containing reactive methacrylate groups is formed at the surface of the silica. Increasing thickness of the corona correlates with increased liquid-like properties of nanoparticles when solvent is removed from the system. There are several rough order analyses that can combine information from one or more of the characterization techniques presented above that can give us an enhanced understanding of the functionalized nanoparticles. For example, from Figure 4.2, the TGA data for sample D, we know that the organic content of the sample is 55%. By subtracting the amount of organic content in unfunctionalized particles (7%), we know that the aggregate amount of organic in the corona of the nanoparticles in this sample is 46%. Taking the mean particle diameter of 28.9 nm from the imageJ analysis of the TEM image (recalling that all samples were from the same synthesis of nanoparticles and only differ by the functionalization), we can

make the rough assumption of a spherical particle, yielding a mean particle volume of 1.264×10^{-16} cm^3. Examining isolated nanoparticles in Figure 4.10d) yields a corona thickness of ~22nm, which in turn leads to a shell volume of 1.828×10^{-16} cm^3. Assuming a density for the silica nanoparticles of $2.2 g/cm^3$ and utilizing the fact the functionalized particles are 48% organic, we can calculate a density for the corona of $.146 g/cm^3$ for isolated particles (which ignores the silicon content of the corona which is not captured by the TGA analysis). While there are undoubtedly systemic errors to this analysis, it does confirm that the corona is of very low density when in the isolated state. As a crosscheck, we can do a similar analysis starting from the ^{29}Si NMR data. By comparing the total integrated intensity of the T2 +T3 peaks to the Q3 + Q4 peaks we arrived at the ratio of Si atoms in the nanoparticle to the ratio of Si atoms in the corona, which was 1 : 0.94. Starting with the same assumption of spherical particles with a diameter of 28.9 nm and using a reported density of SiO_2 nanoparticles of $2.2 g/cm^3$, and taking the molecular weight of a hydrolyzed, cross-linked MPTMS molecule to be 171, we can arrive at an aggregate corona weight (that includes the silicon) of 7.45×10^{-17} g. This in turn yields a density of .407 when using the corona volume previously calculated. Using these same numbers, we can conclude that the nanoparticle makes up 40.8% of the volume of this hybrid structure. The density calculated from this method is considerable higher than the density calculated from the TGA analysis, but the difference, which cannot be completely accounted for by the inorganic content of the corona, still shows a trend in the right direction.

This low-density, adsorbed corona leads to a two-part nanofluid, which exhibits macroscopic flow at a very high loading of nanoparticles, yet remains stable of long-periods. Samples stored in clear vials at room temperature and exposed to room lights over a period of several months still maintained approximately the same viscosity. Because it was confirmed that the acrylate groups are un-polymerized, this nanofluid can be polymerized to form a silane nanocomposite with high loadings of silica particles.

4.9 Chapter Summary

This chapter explored, from an analytical chemistry perspective, silica nanoparticles functionalized with high concentrations of MPTMS. From the characterizations presented, we can conclude that, at the onset of liquid-like properties in the dried particles, the resultant corona is a low-density siloxane that is formed from oligomers in solution adsorbing onto the surface of the nanoparticles. The methacrylate groups of the siloxane remain intact, indicating that the fluid can be polymerized to form a nanocomposite with high loadings (~50% by weight) of dispersed silica nanoparticles. Additionally, at lower molarities of MPMTS, it has been shown that the waxy solid, which results from drying, orders into an FCC structure that can be polymerized via the methacrylate groups in the corona. Rough fusion of the characterization data presented indicates that resulting siloxane-organic network is a low density and deformable network than increases in thickness with increasing MPTMS concentration in solution.

This work is preliminary exploration of the physical structure/property relationships for this system—it establishes that a large, low-density, hybrid siloxane-organic corona that is absorbed onto the nanoparticle surface induces liquid-like properties in the absence of solvent. Further research needs to be conducted to determine 1) properties of nanocomposites made from this two-part nanofluid, 2) the evolution of rheological properties with increasing corona thickness, and 3) the quantified stability/aging properties of the liquid.

4.10 References

[1] W. D. Luedtke, U. Landman, *The Journal of Physical Chemistry* **1996**, *100*, 13323.

[2] N. Sandhyarani, T. Pradeep, J. Chakrabarti, M. Yousuf, H. K. Sahu, *Physical Review B* **2000**, *62*, R739.

[3] K. Fujii, Y. Jujita, N. Iyi, H. Kodama, K. Kitamura, *Journal of Materials Science Letters* **2003**, *22*, 1459.

[4] A. S. Athanasios†B. Bourlinos, Demetrios Anglos, Rafael Herrera, Spiros†H. Anastasiadis, Dimitrios Petridis, Emmanuel†P. Giannelis,, *Small* **2006**, *2*, 513.

[5] A. Bourlinos, S. Chowdhury, D. Jiang, Y.-U. An, Q. Zhang, L. Archer, E. Giannelis, *Small* **2005**, *1*.

[6] M. L. Gomez, V. Avila, H. A. Montejano, C. M. Previtali, *Polymer* **2003**, *44*, 2875.

[7] C. von Ferber, A. Jusufi, M. Watzlawek, C. N. Likos, H. Lˆwen, *Physical Review E* **2000**, *62*, 6949.

[8] D. Gorski, E. Klemm, P. Fink, H. Horhold, *Journal of Colloid and Interface Science* **1988**, *126*.

[9] T. Terao, *Journal of Molecular Structure* **1998**, *441*, 283.

CHAPTER 5

USE OF A REACTION-DIFFUSION EQUATION TO MODEL NANOPARTICLE TRANSPORT FOR HOLOGRAPHIC PHOTOPOLYMERIZATION USING STEP-GROWTH POLYMERS

5.1 Introduction

The step-growth, holographic photopolymerization system was modeled using a reaction-diffusion equation. While it is not possible to capture the exact physics of the system, our hope is to qualitatively capture the interplay of system variables to gain insight to in situ processes and to guide future research efforts in this area. Because we are dealing with a complex, multi-component system, which by nature is a non-equilibrium process, it is challenging to produce a realistic model without making assumptions that render quantitative analysis impossible. Without specific knowledge of the thermodynamic interactions between each molecular species, it is difficult to calculate chemical potentials for the system. These interactions are difficult to measure experimentally for multi-component systems, making it a challenge to design a model that can be tied to experimental results. The intent behind this specific modeling effort is to understand the qualitative effect of specific system variables on maximizing anisotropic nanoparticle transport into the regions of high exposure intensity in the holographic interference pattern. The system variables of interest are laser intensity, fringe visibility in the interference pattern, nanoparticle size and initial volume fraction of nanoparticles in the holographic syrup. While are main focus is on nanoparticle transport, we are also interested in the effects upon H-PDLC optical grating efficiency, although this will

only be examined in a qualitative fashion, without an attempt to specifically model the change in index of refraction.

5.2 Review of Prior Efforts

5.2.1 Review of Prior Work in Modeling Diffusion.

Diffusion has been broadly studied over a wide range of materials for well over a century, including more recently the studies of colloidal systems using hard spheres *[1]*, and studies upon polymeric systems based upon free energies derived using the Flory-Huggins lattice model *[2]*. Here in this review, we focus on the diffusion of low molecular weight molecules in polymers *[3]*, and diffusion in polymer blends *[4]*. While some efforts have tried to experimentally measure self-diffusion or tracer diffusion coefficients for colloid/polymer hybrid systems *[5]* and micellar systems *[6, 7]*, no papers have been found which model diffusion of colloids or nanoparticles in polymeric systems. There, however, several papers that report prediction of the phase diagram of a mixture of polymers and colloids based on free volume considerations *[8, 9]*, where the critical parameter was found to be the ratio between colloid radius and polymer radius of gyration. When dealing with macroscopic, phenomenological modeling of diffusion in polymer blends (in other words excluding *ab initio* or molecular dynamic methods), the Flory-Huggins lattice model has been used almost exclusively. Whereas for colloidal, hard sphere systems, Enskog's Theory has been frequently used to determine diffusion coefficients in conjunction with the Carnahan-Starling formula for approximating thermodynamic interactions *[1]*. For the purposes of this current model, the choice is faced of trying

to incorporate particles into a Flory-Huggins system or to insert polymers into a hard spheres calculation in a method that remains physically meaningful. Our initial bias is to base our theoretical system on a lattice model, which can represent both nanoparticles and polymers. On this basis, we examine previous lattice diffusion models, most of which were based upon polymer blends. Considering a particle (be it a molecule, nanoparticle or polymer) in a lattice model, movement is not possible unless there is a adjacent vacancy on the lattice into which the particle must move. After movement, a new vacancy is created in the previous position of the particle. So, when considering system diffusion, one must account for the flux of all of the different particle species, and the vacancy flux. Considering two particle types, A and B, the fluxes can therefore be written as:

$$\begin{aligned} J_A + J_B + J_V &= 0 \\ J_A &= \Lambda_A \nabla(\mu_A - \mu_V) \\ J_B &= \Lambda_B \nabla(\mu_B - \mu_V) \\ J_V &= -J_A - J_B \end{aligned} \tag{5.1}$$

where J_i, μ_I, and Λ_I represent the flux, chemical potential and Onsager Coefficient of component I, respectively. The Onsager Coefficients are chemical-specific phenomenological coefficients that relate the flux to the chemical potential *[2]*. In a system containing n components, there are n^2 Onsager coefficients which provide relationships between the chemical potential of each species to the flux of each species.

In Brouchard, et. al*[2]*., they assumed that the diffusion rate in the system was slow, such that J_v was considered to be zero and the fluxes of and A and B were

then equal and opposite, which led to mutual-diffusion Onsager coefficient, Λ, such that *[2]*

$$J_A = \Lambda_A \nabla \mu_A = \Lambda_A \frac{\partial \mu_A}{\partial \phi_A} \nabla \phi_A$$
$$D_A = \Lambda_A \frac{\partial \mu_A}{\partial \phi_A}, J_A = \Lambda \nabla \mu \tag{5.2}$$
$$\Lambda = \frac{\Lambda_A \Lambda_B}{\Lambda_A + \Lambda_B}$$

Using the Onsager coefficient, Λ, allows the mutual diffusion coefficient, D, to be written in terms of the intrinsic diffusion coefficients, D_A and D_B.

$$D = \frac{D_A \phi \cdot D_B (1-\phi)}{D_A \phi + D_B (1-\phi)}$$
$$\frac{1}{D} = \frac{1}{D_A \phi} + \frac{1}{D_B (1-\phi)} \tag{5.3}$$

In general, this has been called the slow mode theory of mutual diffusion. In contrast, Kramer, et. al. assumed, rather, that diffusion was fast enough that the chemical potential gradient of the vacancies, μ_V, could be considered everywhere 0 *[2]*. This yield the mutual diffusion coefficient, again in terms of the intrinsic diffusion coefficients of:

$$D = (1-\phi) D_A + \phi D_B \tag{5.4}$$

which has been called the fast mode theory of mutual diffusion. Which theory best fits experiment is system dependent, although the fast mode seems to work best for most systems *[10]*. These equations have been applied to identical polymer blends

as well as miscible blends of different molecular weights (both unentangled and entangled *[1]*. The basic equations have been expanded to include polydisperse polymeric systems using the Green-Kubo equations to determine the relationships of the multi-component Onsager coefficients to the mutual diffusion coefficients in both non-reactive and reactive cases *[10, 11]*.

5.2.2 Review of Holographic Photopolymerizaton Modeling Efforts

With an understanding of our basic approach to handling diffusion (the system will be further defined in following sections), we now examine previous efforts in modeling holographic photopolymerization to help guide how we construct our model. In 1994, Zhou and Mouroulis published the first comprehensive work modeling diffusion for a dry photopolymer system that is exposed holographically *[12]*. They assumed a reaction rate that was equal to some initial polymerization rate taken as proportional to the average irradiance, times a sinusoid that represents the spatially varying interference pattern. They also assumed that the diffusion coefficient was exponentially decaying as the reaction progressed. A Fickean equation was used to relate the change in monomer volume fraction in time to the gradient in monomer volume fraction. Vicki Colvin and her co-workers at Bell Labs greatly expanded this work for a liquid acrylate photopolymer system that was under development *[13]*. In this work, the diffusion coefficient was varied with monomer volume fraction, as fit by experimental data using free-volume theory coefficients first developed by Cohen and Turnbull *[14]*. The polymerization rate was varied in the same fashion as utilized by Zhou and

Mouroulis. Bowley and Crawford again expanded the body of work by applying the technique to an H-PDLC system (containing liquid crystals) *[15]*. They assumed that the diffusion coefficient of the monomer decayed with increasing polymer volume fraction and that, due to cross-linking and rapid gelation, there was no diffusion by the polymer. The latter was a key assumption as it allowed them to avoid any type of mutual diffusion coefficient. Given that the diffusion of the liquid crystal was several orders of magnitude faster than the monomer diffusion, they assumed that it was essentially instantaneous on the step size of the monomer diffusion. Therefore, the liquid crystal volume fraction was found by mass balance. Sutherland and co-workers at the Air Force Research Laboratory, completed a comprehensive, 1-D model based on the addition reaction for acrylate HPDLC and compared the results to experiment *[16]*. In this work, they accounted for mutual diffusion due to volume fraction gradients, and for the variation of polymerization and diffusion rates with increasing volume fraction, and found the liquid crystal volume fraction by mass balance. Additionally, they calculated free energy for the liquid crystal based upon Flory-Huggins theory to account for phase separation. Most recently, Meng et. al. expanded the Sutherland work by basing his diffusion equations upon gradients in free energy rather than volume fraction. He also used a binary mutual diffusion coefficient by assuming no polymer diffusion *[17]*.

5.3 Model Development for HPDLCs Containing Nanoparticles using Step-Growth Polymers

As mentioned in a prior section of the chapter, the initial system is set up using a lattice model construct. There are 4 basic species of importance here: the nanoparticles, the monomer, the resultant polymer and the non-reactive liquid crystal. Because we have a multi-component system where little is known of the thermodynamic interactions between components, we attempt to describe the system in terms of intrinsic diffusion coefficients and associated gradients in volume fractions of each component. Following the work of Colvin, we create the polymerization rate as exponentially decreasing with the reduction in monomer volume fraction. The challenge in this system, unlike the works described in the preceding section, is the difficulty in describing the system only in terms of monomer and polymer volume fraction. Because the polymerization mechanism is step-growth, the monomer volume fraction quickly disappears. Without accounting for the molecular weight distribution of the polymer, there does not appear to be a concentration gradient to drive diffusion. We solve this by assuming that all of the diffusion in the system can be described using Stokes-Einstein diffusion. From the real-time experiments in the preceding chapter, we have the volume fractions of remaining reactive groups versus time, which can be considered as (1-p) versus time, where p is the extent of reaction. In a step-growth polymerization, the volume fraction of an n-mer is given by

$$\phi_n = p^{n-1}(1-p). \tag{5.5}$$

Noting that for a monomer, n=1, yields a relationship between monomer volume fraction and extent of reaction.

$$\phi_m = 1 - p \tag{5.6}$$

To calculate Stokes-Einstein diffusion, knowledge of the viscosity is required. From the literature, we find a relationship between viscosity and weight average molecular weight for branched polymers *[18]*.

$$\eta = \left(\bar{X}_w\right)^{.75} \tag{5.7}$$

For step-growth polymerization, there exists a relationship between weight average molecular weight and extent of reaction, which is based upon Carother's equation *[19]*.

$$\bar{X}_w = \frac{1+p}{1-p} \tag{5.8}$$

In this way, the viscosity used to calculate diffusion captures the effect of the first moment of the molecular weight distribution for step-growth polymerization. With these assumptions, we can now proceed to construct the equations that will represent the model system. Additionally, nanoparticle reaction is initially neglected.

5.4 Lattice Model using Stokes-Einstein Diffusion

5.4.1 Equation Development

For the model lattice system, the component fluxes are given by:

$J_m \rightarrow monomer\ flux$

$J_p \rightarrow polymer\ flux$

$J_{np} \rightarrow nanoparticle\ flux$

$J_{LC} \rightarrow liquid\ crystal\ flux$

$J_v \rightarrow vacancy\ flux$

The total flux in the system must sum to zero:

$$J_m + J_p + J_{wp} + J_{cc} + J_v = 0 \tag{5.9}$$

which in turn yields

$$J_v = -J_m - J_p - J_{np} - J_{LC}\,. \tag{5.10}$$

The flux of each component can be represented by the intrinsic diffusion coefficient, here represented by Λ_i, multiplied by the volume fraction gradient of component i,

$$J_m = -\Lambda_m \frac{\partial \phi_m}{\partial x}, J_p = -\Lambda_p \frac{\partial \phi_p}{\partial x}, J_{np} = -\Lambda_{np} \frac{\partial \phi_{np}}{\partial x}, J_{LC} = \Lambda_{LC} \frac{\partial \phi_{LC}}{\partial x}\,. \tag{5.11}$$

It is here noted the all volume fractions considered in the model vary both spatially and temporally. Formally, the notation should be $\phi_i(x,t)$. However, for the sake of space and clarity, the (x,t) notation is dropped from the remainder of the discussions. Following the work of Kramer by using the assumptions that lead to

the fast mode theory, the diffusion flux of component i equals the flux J_i of that component, plus the vacancy flux of that component:

$$J_i^T = J_i + \phi_i[J_v] \tag{5.12}$$

Inserting (5.10) + (5.11) into (5.12) and expanding gives:

$$\begin{aligned}
J_m^T &= -(1-\phi_m)\Lambda_m \frac{\partial \phi_m}{\partial x} + \phi_m \Lambda_{np} \frac{\partial \phi_{np}}{\partial x} + \phi \Lambda_{LC} \frac{\partial \phi_{LC}}{\partial x} \\
J_p^T &= \phi_p \Lambda_m \frac{\partial \phi_m}{\partial x} - (1-\phi_p)\Lambda_p \frac{\partial \phi_p}{\partial x} + \phi_p \Lambda_{np} \frac{\partial \phi_{np}}{\partial x} + \phi_p \Lambda_{LC} \frac{\partial \phi_{LC}}{\partial x} \\
J_{np}^T &= \phi_{np} \Lambda_m \frac{\partial \phi_m}{\partial x} + \phi_{np} \Lambda_p \frac{\partial \phi_p}{\partial x} - (1-\phi_{np})\Lambda_{np} \frac{\partial \phi_{np}}{\partial x} + \phi_{np} \Lambda_{LC} \frac{\partial \phi_{LC}}{\partial x} \\
J_{LC}^T &= \phi_{LC} \Lambda_m \frac{\partial \phi_p}{\partial x} + \phi_{LC} \Lambda_{np} \frac{\partial \phi_{np}}{\partial x} - (1-\phi_{LC})\Lambda_{LC} \frac{\partial \phi_{LC}}{\partial x},
\end{aligned} \tag{5.13}$$

except here we insert $\phi_{LC}=1-\phi_m-\phi_p-\phi_{np}$ to ensure compressibility. It is worth noting here that the polymer diffusion is represented by Stokes-Einstein form as well. When the extent of reaction is low, the polymer volume fraction is low and the polymer is highly cross-linked (because most monomers used in the experimental systems have a degree of functionality higher than 2), so the polymer is treated as a particle with a radius given by the radius of gyration, R_G, based upon the number average molecular weight calculated using Carother's equation. We give the equation for viscosity as

$$\eta(x,t) = \eta_\circ (\overline{N}w)^{.75} = \eta_\circ [\frac{2-\phi_m}{\phi_m}]^{.75}, \tag{5.14}$$

where η_o is the initial monomer viscosity. While the model as stated does not explicitly account for changes in viscosity due to the functionality of the monomer, the functionality is captured in the initial viscosity term, as monomer viscosity increases with functionality. Using (5.14), we arrive at equations for intrinsic diffusion coefficients for each of the components.

$$\Lambda_m = \frac{\phi_m K_B T \phi_m^{.75}}{6\pi\eta_\circ R_m (2-\phi_m)^{.75}} = \frac{D_\circ \phi_m^{.75}}{(2-\phi_m)^{.75}}, D_\circ = \frac{K_B T}{6\pi\eta_\circ R_\circ}$$

$$\Lambda_p = \phi_p D_p = \frac{D_\circ \phi_m^{1.25}}{\ell_\circ (2-\phi_m)^{.75}}, D_p = \frac{K_B T}{6\pi\eta R_G}, R_G = \overline{N} n^{1/2} R_\circ \tag{5.15}$$

$$\Lambda_{np} = \frac{\phi_{np} K_B T R_\circ \phi_m^{.75}}{6\pi\eta_\circ R_\circ R_{np} (2-\phi_m)^{.75}} = \frac{D_\circ \phi_{np} \phi_m^{.75}}{R_{np} (2-\phi_m)^{.75}}$$

$$\Lambda_{LC} = \phi_{LC} \frac{K_B T \phi_m^{.75}}{6\pi\eta_\circ R_\circ (2-\phi_m)^{.75}} = D_\circ \phi_{LC} \frac{\phi_m^{.75}}{(2-\phi_m)^{.75}}$$

D_o is the initial monomer diffusion coefficient. From conservation of mass,

$$\frac{\partial \phi_i}{\partial t} + \nabla J_i = 0 \tag{5.16}$$

Combining with equations in (5.12), (5.13), and (5.14), yields Fick's second law of diffusion (in one dimension):

$$\frac{\partial \phi_i}{\partial t} = \frac{\partial}{\partial x}\left[-J_i - \phi_i J_v\right] \tag{5.17}$$

The reaction terms contain a rate constant that varies with polymer volume fraction ($1-\phi_m$) and contains the spatial variance due to the laser interference pattern:

$$\begin{aligned} F(x,t) &= F_\circ h(\phi_p)\left[f(x)\right] \\ f(x) &= \frac{1}{2}+\frac{1}{2}V\cos(kx) \\ h(\phi_p) &= e^{-\alpha\phi_p} \end{aligned} \tag{5.18}$$

where V is the fringe contrast of the interference pattern, F_o is the initial polymerization rate based upon laser irradiation intensity and $k=\frac{2\pi}{\omega}$ (ω is wavelength). Adding reaction terms to (5.12) and expanding into matrix form (with unit volume again set to unity for convenience) yields:

$$\frac{\partial}{\partial t}\begin{bmatrix}\phi_m\\ \phi_p\\ \phi_{np}\\ \phi_{Lc}\end{bmatrix}=\frac{\partial}{\partial x}\left\{\begin{bmatrix}(1-\phi_m) & -\phi_m & -\phi_m & -\phi_m\\ -\phi_p & (1-\phi_p) & -\phi_p & -\phi_p\\ -\phi_{np} & -\phi_{np} & 1-\phi_{np} & -\phi_{np}\\ -\phi_{Lc} & -\phi_{Lc} & -\phi_{Lc} & 1-\phi_{Lc}\end{bmatrix}\begin{bmatrix}\Lambda_m\frac{\partial\phi_m}{\partial x}\\ \Lambda_p\frac{\partial\phi_p}{\partial x}\\ \Lambda_{np}\frac{\partial\phi_{np}}{\partial x}\\ \Lambda_{Lc}\frac{\partial\phi_{Lc}}{\partial x}\end{bmatrix}\right\}+\begin{bmatrix}-F(x,t)\phi_m\\ F(x,t)\phi_m\\ 0\\ 0\end{bmatrix} \tag{5.19}$$

Non-dimensionalizing, and usig $z=kx$, and noting $\tau=tF_\circ$, we can now expand the first equation in (5.18) using:

$$R=\frac{K_B T K^2 D_\circ}{F_\circ} \tag{5.20}$$

Which is the parameter defined by Zhou and Mouroulis.

$$\frac{\partial \phi_m}{\partial \tau} = \frac{\partial}{\partial z}\left[R(1-\phi_m)\Lambda_m \frac{\partial \phi_m}{\partial z} \right] - \frac{\partial}{\partial z}\left[R\phi_m \Lambda_p \frac{\partial \phi_p}{\partial z} \right] - \frac{\partial}{\partial z}\left[R\phi_m \Lambda_{np} \frac{\partial \phi_{np}}{\partial z} \right] - \frac{\partial}{\partial z}\left[R\phi_m \Lambda_{LC} \frac{\partial \phi_{LC}}{\partial z} \right]$$

$$-h(\phi p) f(z) \phi_m \tag{5.21}$$

$$\frac{\partial \phi_p}{\partial \tau} = -\frac{\partial}{\partial z}\left[R\phi_p \Lambda_{np} \frac{\partial \phi_m}{\partial z} \right] + \frac{\partial}{\partial z}\left[R(1-\phi_p)\Lambda_p \frac{\partial \phi_p}{\partial z} \right] - \frac{\partial}{\partial \tau}\left[R\phi_p \Lambda_{np} \frac{\phi_{np}}{\partial z} \right] - \frac{\partial}{\partial z}\left[R\phi_p \Lambda_{LC} \frac{\partial \phi_{LC}}{\partial z} \right]$$

$$+h(\phi p) f(z) \phi_m \tag{5.22}$$

$$\frac{\partial \phi_{np}}{\partial \tau} = -\frac{\partial}{\partial z}\left[R\phi_{np} \Lambda_m \frac{\partial \phi_m}{\partial z} \right] - \frac{\partial}{\partial z}\left[R\phi_{np} \Lambda_p \frac{\partial \phi_p}{\partial z} \right] + \frac{\partial}{\partial z}\left[R(1-\phi_{np})\Lambda_{np} \frac{\partial \phi_{np}}{\partial z} \right] - \frac{\partial}{\partial z}\left[R\phi_{np} \Lambda_{LC} \frac{\partial \phi_{LC}}{\partial z} \right] \tag{5.23}$$

$$\frac{\partial \phi_{LC}}{\partial \tau} = -\frac{\partial}{\partial z}\left[R\phi_{LC} \Lambda_m \frac{\partial \phi_m}{\partial z} \right] - \frac{\partial}{\partial z}\left[R\phi_{LC} \Lambda_p \frac{\partial \phi_p}{\partial z} \right] - \frac{\partial}{\partial z}\left[R\phi_{LC} \Lambda_{np} \frac{\partial \phi_{np}}{\partial z} \right] + \frac{\partial}{\partial z}\left[R(1-\phi_{LC})\Lambda_{LC} \frac{\partial \phi_{LC}}{\partial z} \right] \tag{5.24}$$

Now, the system can be solved with a finite difference method using a forward time-central space scheme, where n is the n_{th} time (τ) step and j is the j_{th} interval of z.

Defining:

$\Lambda_m,_m = R(1-\phi_m)\Lambda_m$; $\Lambda_m,_p = -R\phi_m\Lambda_p$; $\Lambda_{m,np} = -R\phi_m\Lambda_{np}$; $\Lambda_{m,LC} = -R\phi_m\Lambda_{LC}$;

$\Lambda_{p,m} = -R\phi_p\Lambda_m$; $\Lambda_{pp} = R(1-\phi_p)\Lambda_p$; $\Lambda_{p,np} = -R\phi_p\Lambda_{np}$; $\Lambda_{np,m} = -R\phi_{np}\Lambda_m$;

$\Lambda_{np,p} = -R\phi_{np}\Lambda_p$; ; $\Lambda_{np,np} = (1-\phi_{np})\Lambda_{np}$; $\Lambda_{p,LC} = -R\phi_p\Lambda_{LC}$; $\Lambda_{np,LC} = -R\phi_{np}\Lambda_{LC}$

We can now rewrite (5.20) as

$$\frac{\phi_{m,j}^{n+1}-\phi_{m,j}^{n}}{\Delta\tau}\cdot\frac{1}{\Delta z^2}=\begin{bmatrix}\Lambda_{m,m;j+\frac{1}{2}}(\phi_{m,j+1}^{n}-\phi_{m,j}^{n})-\Lambda_{m,m;j-\frac{1}{2}}(\phi_{m,j}^{n}-\phi_{m,j-1}^{n})\\+\Lambda_{m,p;j+\frac{1}{2}}(\phi_{p,j+\frac{1}{2}}^{n}-\phi_{p,j}^{n})-\Lambda_{m,p;j-\frac{1}{2}}(\phi_{p,j}^{n}-\phi_{p,j-1}^{n})\\+\Lambda_{m,np;j+\frac{1}{2}}(\phi_{np,j+1}^{n}-\phi_{np,j}^{n})-\Lambda_{m,np;j-\frac{1}{2}}(\phi_{np,j}^{n}-\phi_{np,j-1}^{n})\\+\Lambda_{m,LC;j+\frac{1}{2}}(\phi_{LC,j+1}^{n}-\phi_{Lc,j}^{n})-\Lambda_{m,Lc;j-\frac{1}{2}}(\phi_{LC,j}^{n}-\phi_{Lc,j-1}^{n})\end{bmatrix}-h(\phi_{p,j}^{n})\phi_{m,j}^{n} \tag{5.25}$$

and (5.21) and (5.22) are rewritten in a similar fashion. Because the diffusion rate of the liquid crystal is approximately 3 orders of magnitude faster than any of the other components, it is found by mass balance instead of (5.23) when the model is computed. For this explicit finite difference scheme to be numerically stable, it must meet the Courant-Friedrichs-Lewy (CFL) condition, which states:

$$\frac{\Lambda_i\Delta\tau}{(\Delta z)^2}\le\frac{1}{2}\qquad\text{or}\qquad\Delta\tau\le(\Delta z)^2\cdot\min j\left[\frac{1}{1\Lambda_{i,k,j}+\frac{1}{2}}\right] \tag{5.26}$$

For all $\Lambda_{i,k}$

5.4.2 System Simulation and Results

The model was initially evaluated with the following conditions on a grid of 100 for z: $\phi_{np}=.1$, $\phi_{Lc}=.3$, $\phi_p=0$, $\phi_m=.6$. Periodic boundary conditions were used during computation. The adjustable parameters were initially set to: R=1, V=.9, α=4.5, ϕ_{npo}=.2 and the length set to z=4π. Note that the parameter R balances initial diffusion and polymerization rates and is inversely proportional to laser intensity. The parameter α was used as fit parameter to the experimental data from the previous chapter in order to assure realistic conditions. Figure 5.1 illustrates the

results of the simulations at a time, tF_o, of 4 seconds. In this figure, we can see that embedding the molecular weight distribution into the viscosity term appears sufficient, as the model shows polymer transport that seems qualitatively consistent with experimental results in that the polymer volume fraction was at a maximum in the bright regions of the interference patterns and at a minimum in the dark regions. Additionally, the liquid crystal is at a maximum in the dark regions, which is also consistent with experiment. The nanoparticles appear to have diffused much less than the monomers or polymers, which is not surprising since they are much

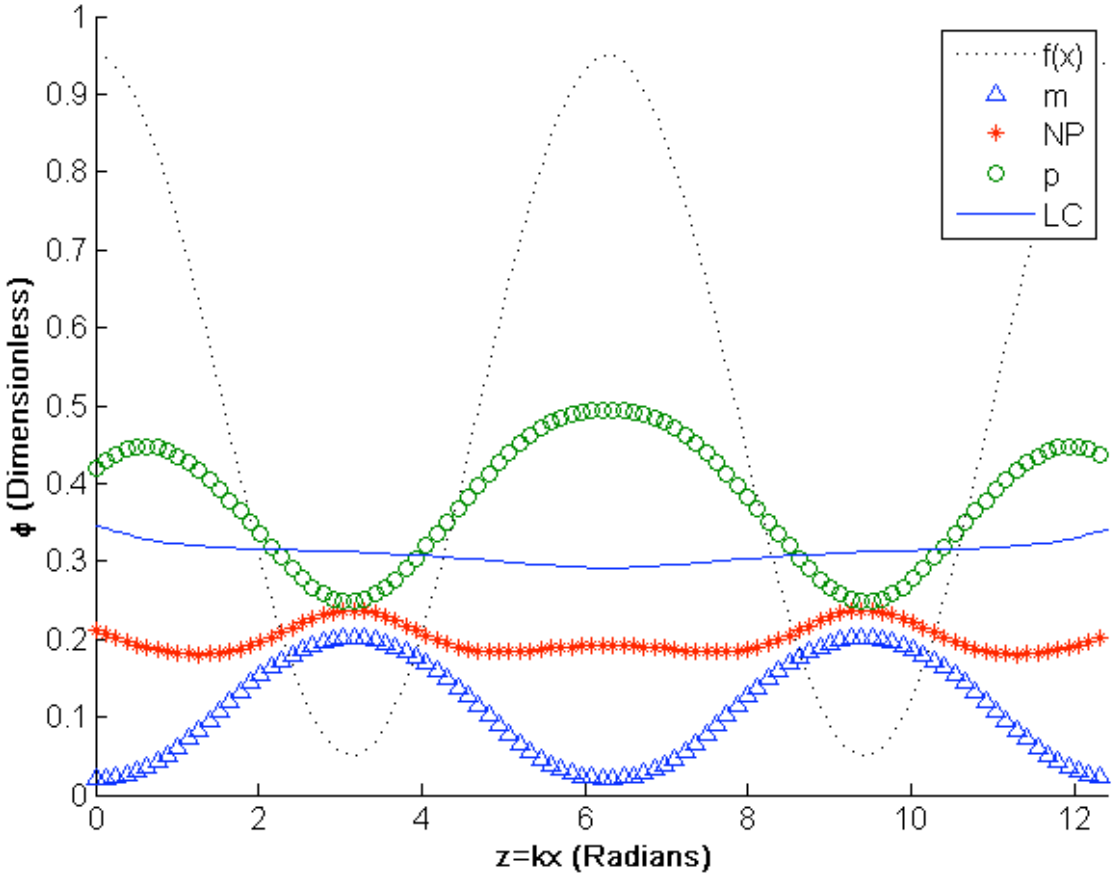

Figure 5.1 System simulation based upon the lattice model neglecting thermodynamic interactions. Adjustable parameters were set to R=1, V=.9, and α=4.5.

larger than any other species and Stokes-Einstein diffusion is inversely proportional to radius. However, upon close examination, diffusion of the nanoparticles is maximized in the dark regions and minimized and the bright regions, which is the opposite of what is demonstrated experimentally for methacrylated particles. A possible cause could be the lack of a nanoparticle reaction term—however, the model was rerun with the addition of this term with the same results. From this, we must consider using only volume fraction gradients without consideration of thermodynamic interactions to be insufficient method to qualitatively model our system. For this reason, the model was re-accomplished using Flory-Huggins interaction parameters.

5.5 Lattice Model using Flory Huggins Interaction Parameter Without Nanoparticle Reaction

There are two essential difficulties with using the Flory-Huggins interaction parameter, χ, in the development of the system free energy for the purpose of calculating chemical potential gradients. The first is that, as mentioned before, because the system is multi-component, there are essentially n-1 Flory interaction parameters and we have no simple way of estimating them independently. Because of the extremely fast diffusion of liquid crystal with respect to the rest of the system, we can treat the liquid crystal as the solvent in the system, allowing the use of Flory-Huggins free energies for a polymer-solvent system. Even with this assumption, there are still multiple interaction parameters. This is partially handled by

recognizing that both monomers and polymers are n-mers, which can be accounted for using Flory-Huggins. The last difficulty involves how to treat the nanoparticles within a Flory-Huggins free energy construct. The nanoparticles used in most of the experimental efforts in this work are functionalized with a dense coating of reactive groups. From the perspective of chemical interactions, then, it makes since to represent the nanoparticle as a polymer whose radius of gyration is equal to the nanoparticle radius (which also assumes a good solvent). From the radius of gyration, we can then calculate an assumed number-averaged degree of polymerization for our "polymer" nanoparticle. These assumptions leave us with liquid crystal as the solvent and all other components as polymer, allowing us to use a single interaction parameter in our model system. Since we want to use as simple of system as will qualitatively represent the system, we initially neglect any chemical reactions involving the nanoparticles.

5.5.1 Equation Development

Gibbs reduced free energy of mixing from Flory-Huggins theory of mixing for a polymer solution written in terms of liquid crystal volume fraction is given by *[16]*:

$$\Delta g(t) = \phi_{LC} \ln(\phi_{LC}) + \frac{(1-\phi_{LC})}{N(t)} \ln(1-\phi_{LC}) + \chi \phi_{LC}(1-\phi_{LC}) \tag{5.27}$$

For thiol-ene H-PDLC formulations with 30% volume fraction bi-phenyl liquid crystals, White et. al. experimentally discovered, using spectroscopic methods, that phase separation was primarily initiated at an extent of reaction of p=.5. Further, the gel-point for this system is calculated to be p=.71 based upon the gel point equation

[20]. Assuming a Flory distribution for step-growth polymers, we find that phase separation begins at

$$\overline{N}_n = \frac{1}{1-p} = 2\,. \tag{5.28}$$

Similarly, the gel point is found to occur at $\overline{N}_n = 3.45$. The knowledge of degree of polymerization at phase separation can be used to estimate χ. Using the equation

$$2\chi = (1 + \frac{1}{\sqrt{N_c}})^2\,, \tag{5.29}$$

we calculate that $\chi = 1.46$ for the thiol-ene system *[19]*. In general, accurately estimating diffusion is difficult for step-growth polymers because you must consider independent diffusion coefficients across all n-mers in molecular weight distribution. In this case, due to the low degree of polymerization at both phase separation and gelation, we assume that we can model with a reasonable degree of accuracy using a molecular weight distribution of only monomers, dimer and trimers and neglect all terms with a value of n higher than 3.

Using the assumed radius of gyration for the nanoparticle we calculate the effective number average molecular weight of the nanoparticle.

$$R_{np} = R_g = \overline{N}_n^{\frac{1}{2}} \ell_\circ \qquad \ell_\circ \cong 1.5 \text{ nm for thiol-ene monomers} \tag{5.30}$$

For a 20 nm diameter nanoparticle, this equation yields $\overline{N}_n \cong 45$. We can represent the polymer volume fraction as (with $\phi_{np}=\phi_4$):

$$1-\phi_{LC}=\phi_P=\phi_{1,n=1}+\phi_{2,n=2}+\phi_{3,n=3}+\phi_{4,n=45} \tag{5.31}$$

Using (5.30) we can rewrite Δg as,

$$\Delta g(t)=\phi_{Lc}\ln\phi_{Lc}+\frac{\phi_1+\phi_2+\phi_3+\phi_{np}}{N(t)}\ln(\phi_1+\phi_2+\phi_3+\phi_{np})+\chi\phi_c(\phi_1+\phi_2+\phi_3+\phi_4) \tag{5.32}$$

N(t) in (5.32) is taken to be N_n for the system extent of reaction. Using (5.32) we can now calculate the chemical potential of component i.

$$\mu_i=\frac{\partial\Delta g}{\partial\phi_i} \tag{5.33}$$

$$\mu_{LC}=\ln\phi_{LC}+1-\frac{1}{N_n}\ln(1-\phi_{LC})-\frac{1}{N}+x(1-2\phi_{LC}) \tag{5.34}$$

$$\frac{\partial\mu_{LC}}{\partial x}=\frac{\partial\mu_{LC}}{\partial\phi_{LC}}\frac{\partial\phi_{LC}}{\partial x}=\left[\frac{1}{\phi_{LC}}+\frac{1}{N(1-\phi_{LC})}-2\chi\right]\frac{\partial\phi_{LC}}{\partial x} \tag{5.35}$$

For the polymer components, we can rewrite as $1-\phi_{LC}=\phi_P=\sum_{i=1}^{4}\phi_i$. Using this notation allows us to write the equation for chemical potential for component i in a more compact form.

$$\mu_i=\frac{\Delta g}{\partial\phi_i}=\frac{1}{N_i}\phi_i+\frac{\phi_i}{N_i}\sum_{k=1}^{4}\phi_{k,k\neq1}+\chi\phi_{LC}\phi_i \tag{5.36}$$

for ϕ_P components:

$$\frac{\partial \mu_i}{\partial x} = \frac{\partial \mu_i}{\partial \phi_i}\frac{\partial \phi_i}{\partial x} = \left[\frac{1}{N_i \phi_i}(1 - \frac{1}{\phi_i}\sum_{k=1}^{4}\phi_{k,k\neq 1}) + \chi\phi_{LC}\right]\frac{\partial \phi_i}{\partial x} \tag{5.37}$$

For a one-dimensional system, the flux of each component can be written in terms of the Onsager coefficient as:

$$J_i = -\Lambda_i \frac{\partial \mu_i}{\partial x} \tag{5.38}$$

where we define $\Lambda_i = D_\circ \phi_i$ and where $D_\circ$ is the intrinsic-diffusion of the monomer.

But,

$$J_i = -D_i \frac{\partial \phi_i}{\partial x} \tag{5.39}$$

Where D_i is the intrinsic-diffusion of component i. Combining (5.35), (5.37-8), and (5.39) we can find the relationship between the Onsager coefficients and intrinsic diffusion coefficients for the polymer components. The initial liquid crystal diffusion is measured and ϕ_{LC} does not need to be calculated since it is found using the incompressibility condition and a mass balance.

$$D_i = \Lambda_i\left[\frac{1}{N_i\phi_i}\left(1 - \frac{1}{\phi_i}\sum_{k=1}^{4}\phi_{k,k\neq 1}\right) + x\phi_{LC}\right] \tag{5.40}$$

We can now rewrite the total diffusive flux for each component as

$$J_i^T = -(1-\phi_i)D_i + \phi_i\sum_{k=1}^{5}D_{k,k\neq i} \tag{5.41}$$

Fick's law in this case is given by:

$$\frac{\partial \phi i}{\partial t} = -\frac{\partial}{\partial x}(J_i^T) \tag{5.42}$$

The reaction term is unmodified from the previous model except

$$h(\phi_p) = h(\phi_2, \phi_3) = e^{-\alpha(\phi 2 + \phi 3)} \tag{5.43}$$

The reaction term for ϕ_2 (dimers) and ϕ_2 (trimers) is multiplied by (1-p) and p respectively to account for the molecular weight distribution of step growth polymers, where p is defined as $1/\ \phi_1$. The finite difference scheme used in the previous model was repeated, using the same periodic boundary conditions and same set of adjustable parameters.

5.5.2 System Simulation and Results

The model was run across a broad swath of the adjustable parameter space in an attempt to predict conditions that lead to maximizing nanoparticle transport. The best results were found with the following combination of parameters: R=.25, exposure time, tF_o=6, V=.9, R_{np}=2.5 nm. The results of this simulation are presented in Figure 5.2. Examining Figure 5.2 closely, we first see evidence that using the interaction parameter yield expected results. The monomer, with n=1, is below N_c and hence exhibits a similar profile as found in the simulation which only considered the concentration gradient. While the model does not explicitly address phase separation, one can see that the polymer, with $N_n > N_c$, exhibits sharply different behavior in the dark region of the pattern, with a sharply varying curve shape that is opposite to the curve of the liquid crystal and is assumed to be

evidence of phase separation due to thermodynamic interactions. Note that in this region ϕ_{Lc} is large and might possibly reside under the spinodal decomposition curve in the phase diagram (although this has not been calculated). However, it seems that the nanoparticles in the system have exhibited very little movement.

We can theorize that because the polymer, which is the only other component that should have strong interactions with the liquid crystal, diffuses much more rapidly, the free energy is minimized by polymer movement before much diffusion of the nanoparticles has occurred. So, once again, it appears

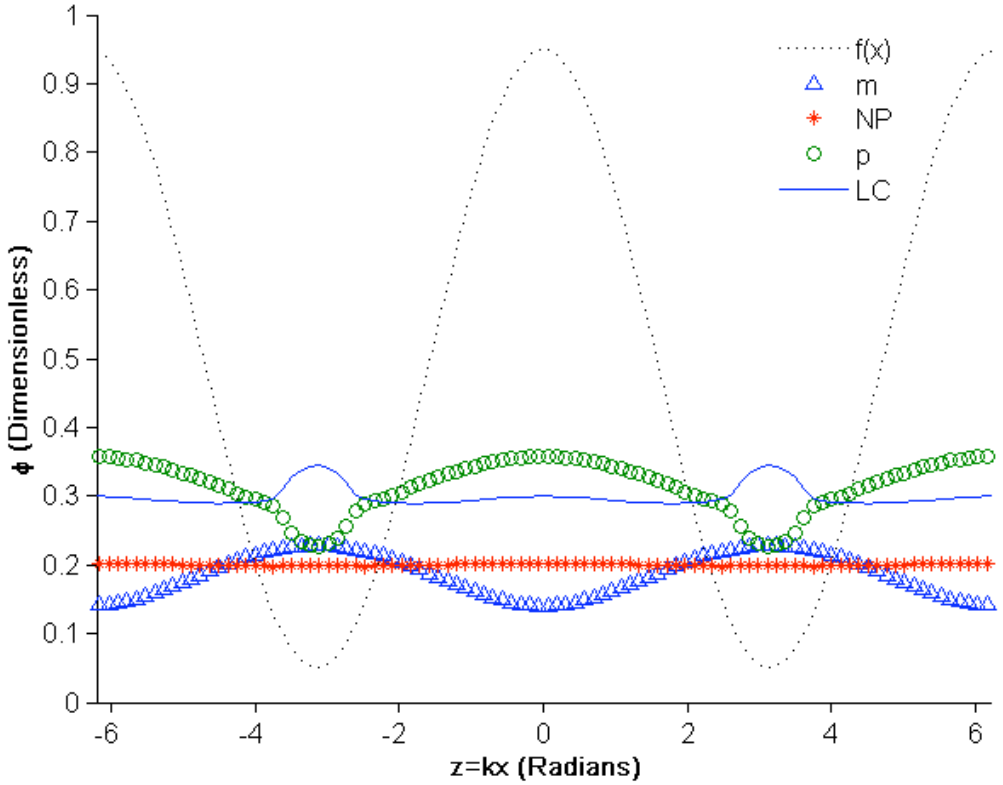

Figure 5.2 System simulation base on model using Flory-Huggins interaction parameter, χ=1.46. Adjustable parameter values used in the simulation were R=.25, V=.9, α=4.5, ϕ_{np0} =.2 and R_{np}=2.5.

necessary to include a nanoparticle reaction term to qualitatively capture system performance.

5.6 Lattice Model using Flory Huggins Interaction Parameter With Nanoparticle Reactions

To account for nanoparticle reaction in the system, the model was structured so that reacting nanoparticles were incorporated into polymer volume fraction. To accomplish this change, the same polymerization rate term F was used for the nanoparticle reaction. It was assumed that the nanoparticle only reacted with dimers and trimers, and that the reactions occurred in the same ratio as dimer and trimer addition based on the molecular weight distribution. Practically speaking, this was accomplished by multiplying the nanoparticle reaction term by p and (1-p) in the dimer and trimer reaction-diffusion equations, in a manner analogous to the monomer reaction. The change in free energy was accounted for by using an average N_n that is weighted by the respective volume fractions. When the model was coded into the finite difference program, the total amount of reacted nanoparticle was tracked so that the total nanoparticle volume fraction was unchanged at the end of the simulation. Running the revised simulation using the same values for the adjustable parameters as were used in Figure 5.2 yielded the results presented in Figure 5.3. From Figure 5.3, we can see that this model captures all of the qualitative trends as seen over the course of our experiments. Evidence of phase separations still appears to be present, but anisotropic nanoparticle transport into the bright regions of the interference pattern is

evidenced. From a modeling perspective, reacting nanoparticles initiates chemical potential gradients in that species which in turn promotes the transport.

Over the course of utilizing the model to explore the adjustable parameter space, results were obtained which may offer plausible evidence as to the cause of the delay in phase separation with increasing nanoparticle loadings as noted in Chapter 4. Figure 5.4 shows both the simulation without nanoparticle reaction and the simulation including the nanoparticle reactions run under identical conditions (all parameters identical).

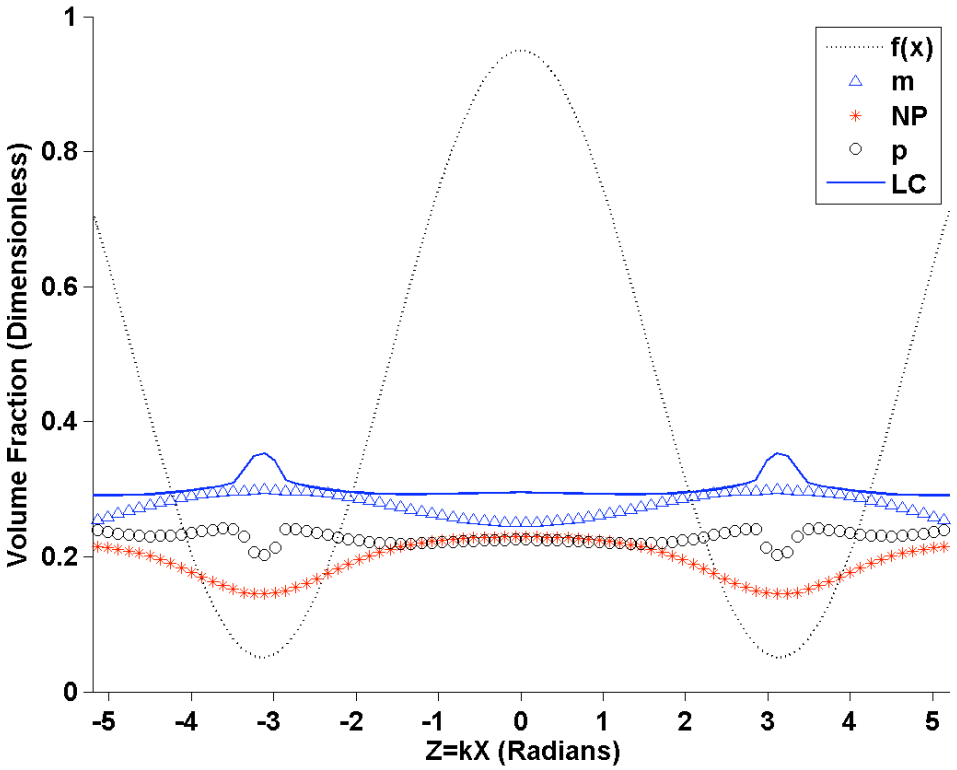

Figure 5.3 System simulation base on model using Flory-Huggins interaction parameter, χ=1.46 and including nanoparticle reactions. Adjustable parameter values used in the simulation were R=.25, V=.9, α=4.5, ϕ_{np0} = .2 and R_{np}=2.5.

As we see in Figure 5.4a, the simulation without nanoparticle reactions shows evidence of polymer-liquid crystal phase separation and very little nanoparticle movement, much as before. In Figure 5.4b however, the same conditions do not yield phase separation, although the nanoparticles do exhibit transport. Examining the differences in the models brings us toward a plausible explanation for the lack of phase separation in the second system. As mentioned before for the first system, the lack of a nanoparticle reaction and the unimpeded polymer diffusion allows the polymer to diffuse freely and for phase separation to occur. In the model that includes nanoparticle reaction, the polymer diffusion is slowed by the incorporated nanoparticles due to the weighted average degree of polymerization. We now theorize that because they do not diffuse as quickly, the liquid crystal-polymer volume fractions are delayed in crossing the spinodal curve in the phase diagram and phase separation is delayed. This assertion can be further supported by examining the evolution of ϕ_p at the minimum of the interference pattern for the same adjustable parameters, while varying R, as shown in Figure 5.5.

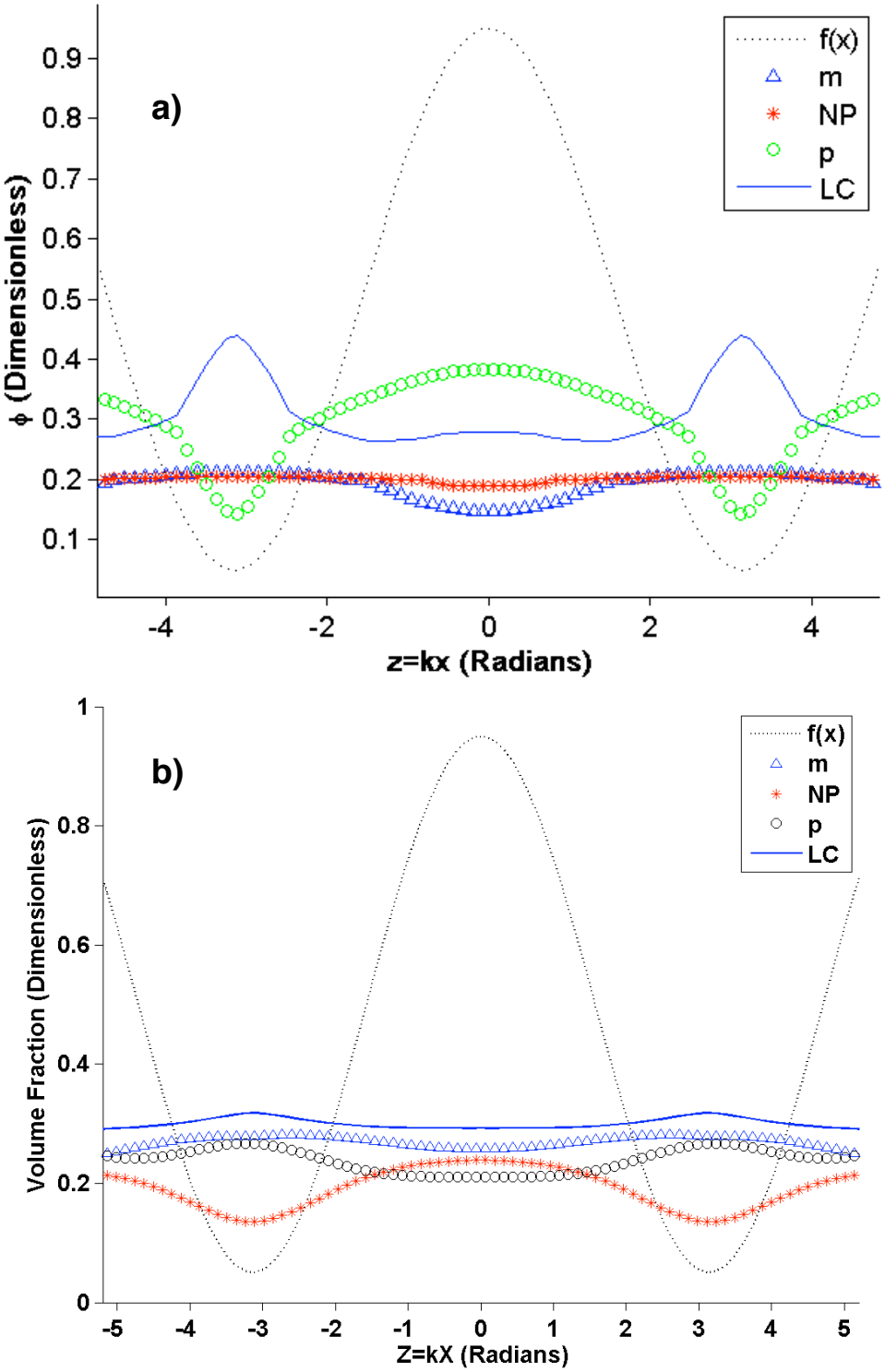

Figure 5.4 System simulation using Flory-Huggins interaction parameter a) without and b) with nanoparticle reaction. Parameter values for both simulations are R=.4, V=.9, ϕ_{np0} =.2, α=4.5 and R_{np}=2.5.

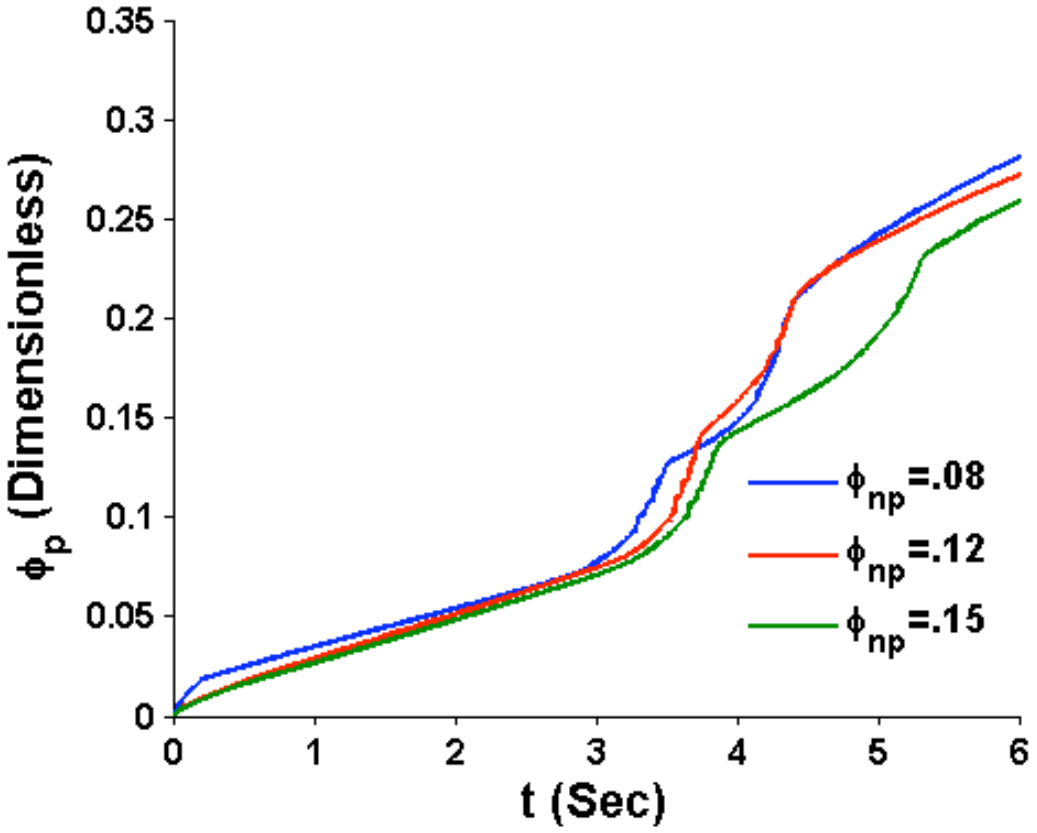

Figure 5.5 Extraction of the evolution of polymer volume fraction at interference minimum versus time for simulations with values of varied nanoparticle loading. All other parameters held constant at R=.25, R_{np}=.4, V=.9, ϕ_{np0} =.2 and α=4.5.

In Figure 5.5, the first inflection point is taken to be the time phase separation begins. This inflection point moves to longer times with increasing nanoparticle loading, which is again consistent with slower phase separation due to polymer viscosity increasing with reactive nanoparticle content.

It is instructive to examine how the variations in parameters affects the results of both nanoparticle and polymer transport to hopefully guide future experimental efforts to maximize either nanoparticle transport or holographic

grating performance. Figure 5.6 illustrates the effect of fringe visibility on volume fraction distribution. Figure 5.6a demonstrates that poor fringe visibility in the laser interference pattern (reduced amplitude of sinusoidal variation in intensity such that there is significant laser intensity in the dark areas) has a dramatic impact on the modeled ability to sequester the nanoparticle into the bright regions of the pattern. Figure 5.6b demonstrates that, in the model, poor fringe visibility greatly reduces phase separation between the polymer and liquid crystal. Figure 5.7 illustrates the impact of initial nanoparticle volume fraction upon the resultant final distribution of nanoparticle across the period. At the starting volume fractions of ϕ_{np0} = .12 and .15, the final nanoparticle distribution appears to have "higher harmonics" and is indicative of what has been termed "overexposure" in the literature *[13]*. This indicates that the reaction rate is dominating over diffusion rate, which is an indication that, with intensity held constant, that increasing ϕ_{np0} is slowing down diffusion. Finally, we note that the model has almost no sensitivity to nanoparticle radius. We attribute this to our assumption that the reacting nanoparticle is incorporated into polymer and that the change to the free energy is from a volume fraction weighted average. Because of this insensitivity, it is likely that nanoparticle transport is overestimated using this model.

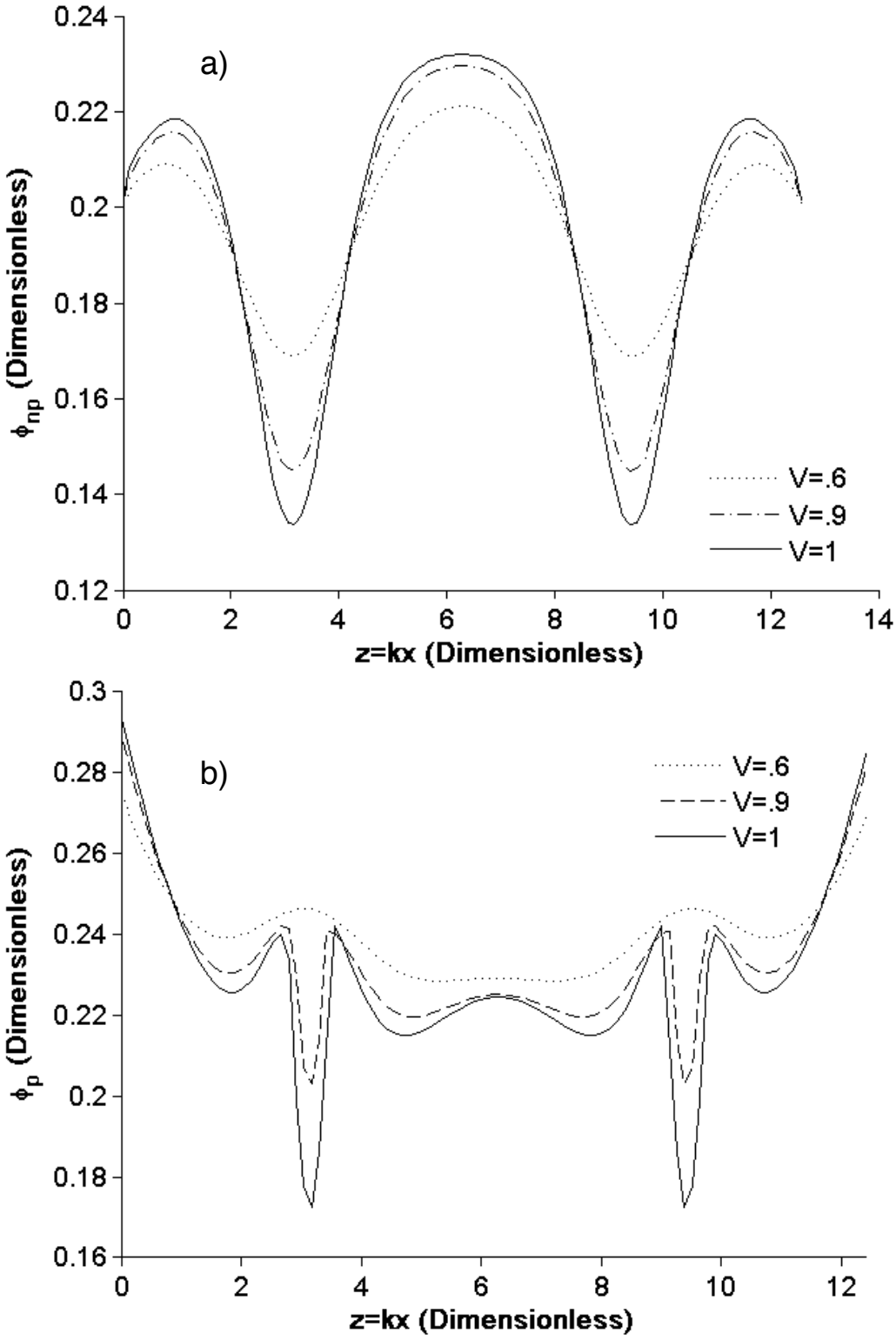

Figure 5.6 The effect of variation in fringe visibility on a)nanoparticle volume fraction and b) polymer volume fraction for V= .6, .9, and .1 All other parameters held constant at R_{np}=.25, ϕ_{np0} =.2, R=.25, and α=4.5.

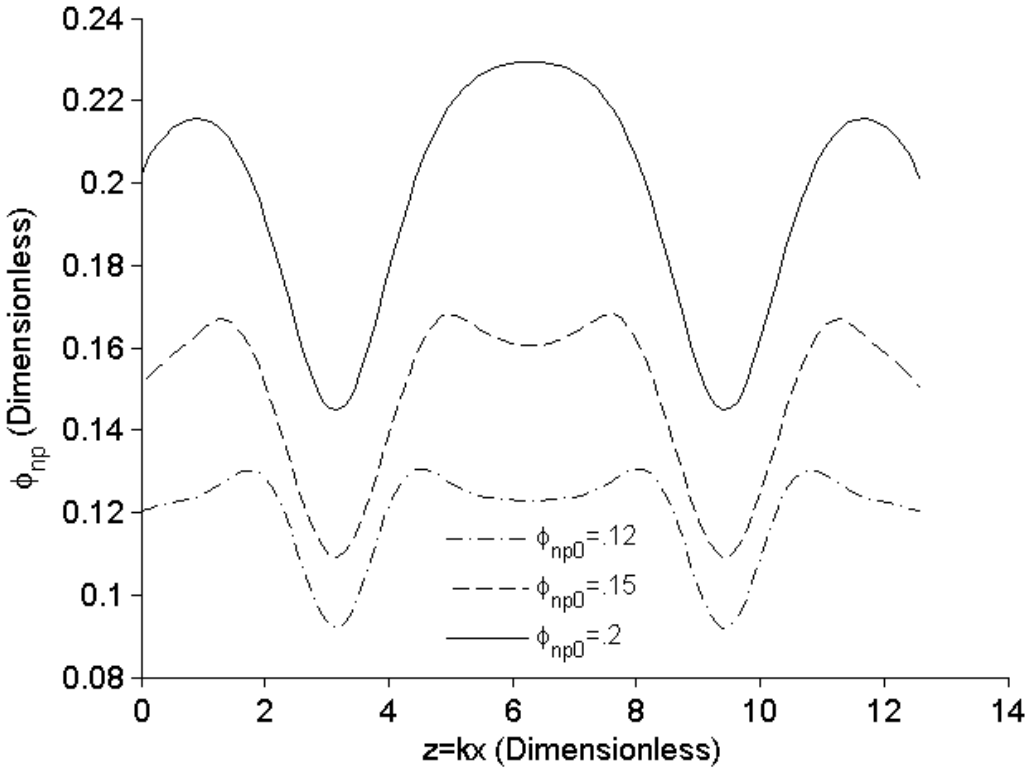

Figure 5.7 The effect of increase in initial nanoparticle volume fraction on the variation in nanoparticle distribution. Initial nanoparticle volume fractions were ϕ_{np0} = .12, .15 and .2. Other parameters held constant at R_{np}=.25, R=.25, V=.9 and α=4.5.

5.7 Chapter Conclusions

Initial modeling efforts attempted to describe a holographic, step-growth photopolymerization system with a monomer reaction equation coupled with diffusion equations using Stokes-Einstein derived mutual diffusion coefficients that were based solely upon concentration gradients without consideration to thermodynamic interactions. While this system predicted nanoparticle transport, it qualitatively failed to show nanoparticle volume fractions maximized in the bright regions of the holographic interference pattern as demonstrated experimentally in

Chapter 4. A nanoparticle reaction term was added to the system of equations, yet still failed to demonstrate nanoparticle transport into the bright regions.

A second model was based upon the Flory-Huggins lattice model for polymer-solvent systems. Based upon fast diffusion rates, the liquid crystal was chosen as the solvent. The system was reduced to a single Flory interaction parameter by assuming that all of the non-liquid crystal components could be treated as a single polymer that only varied by degree of polymerization, with the nanoparticle treated as a polymer in a good solvent with a radius of gyration equal to the nanoparticle radius. This parameter was calculated from experimental evidence presented in the literature for a similar system *[20]*. Noting that for phase separation occurred for our experimental system at N_n=2 and the gel-point occurred at N_n=3.5 led to neglecting all but the first three terms in the polymer distribution. These assumptions lead to a model that appeared to correctly predict phase separation, which was not treated explicitly, but failed to demonstrate sufficient nanoparticle transport. Adding a nanoparticle reaction term predicted correctly, in a qualitative fashion, nanoparticle transport into the bright regions of the interference pattern. Additionally, it appears to correctly predict the delay in phase separation due to increasing nanoparticle volume fraction as noted experimentally in Chapter 4. Because the nanoparticle reaction term incorporates the nanoparticle into the polymer, rather than treating the reacted polymer/nanoparticle system as a separate species, the model is not sensitive to nanoparticle radius. Also, because higher order terms in the polymer distribution are neglected, polymer diffusion in later experimental stages appears to be overstated.

For the developed model to be useful to experimentalist wishing to gain system insight, it is important to concisely list the conditions in which the model will yield quantitative information—outside of this regime should only yield qualitative insights. This model, based on the specific 3 terms included in the molecular weight distribution and lack of explicit treatment of phase separation, is only valid in the regime up until the extent of reaction where macroscopic phase separation occurs (experimentally this is ~p of .5 for thiol-ene systems). Any information gleaned from utilizing the model outside of this regime should be carefully considered. However, the system should be able to yield some qualitative trends outside the quantitative regime, as evidenced by the correct prediction of the delay in phase separation due to increased nanoparticle loadings and high laser intensities.

From the analysis of the adjustable parameters utilizing in the model, we can also draw some useful conclusions. The Zhou-Mourolis parameter, R, the fringe visibility, V and the nanoparticle loading are all parameters that have a significant effect on system performance. Enhanced system peformance and reduced variability could be achieved by careful system setup to maximize V. By changing the value of R as the effect of laser intensity upon the system, it was demonstrated that there is a distinct region of the parameter space in which the system becomes diffusion-limited and that the system evolves differently in this regime. The model suggested that better optical performance would be gained in the diffusion-limited regime, while maximum nanoparticle transport would be obtained outside of this regime. This suggests that optimum conditions for optical properties and nanoparticle sequestration are different—further experimental work is needed to

validate this assertion. The model also suggests that increased nanoparticle loading causes the system to enter the diffusion-limited regime, as well. This is most likely due to slower polymer diffusion due to incorporation of nanoparticles into the polymer matrix. Study of the system would additionally suggest that future research into nanoparticle transport via this system should focus on materials that can simultaneously reduce viscosity while raising polymerization rates.

5.8 References

[1] J. M. Kincaid, M. L. de Haro, E. G. D. Cohen, *The Journal of Chemical Physics* **1983**, *79*, 4509.
[2] E. J. Kramer, P. Green, C. J. Palmstr¯m, *Polymer* **1984**, *25*, 473.
[3] S. Kobuchi, Y. Arai, *Progress in Polymer Science* **2002**, *27*, 811.
[4] R. Bella, P. Cassagnau, F. Fenouillot, L. Falk, C. Lacoste, *Polymer* **2006**, *47*, 5080.
[5] C.-Y. Chou, B. C. Eng, M. Robert, *Journal of Chemical Physics* **2006**, *124*.
[6] Y. Nogami, M. Iwata, T. Tominaga, *Journal of Molecular Liquids* **2005**, *119*, 83.
[7] D. G. Leaist, L. Hao, *The Journal of Physical Chemistry B* **2001**, *105*, 7446.
[8] S. M. Ilett, A. Orrock, W. C. K. Poon, P. N. Pusey, *Physical Review E* **1995**, *51*, 1344.
[9] G. Oshanin, M. Moreau, S. Burlatsky, *Advances in Colloid and Interface Science* **1994**, *49*, 1.
[10] Y. K. Victor Yashin, Elena Govorun, Arkady Litmanovich,, *Macromolecular Theory and Simulations* **1997**, *6*, 247.
[11] V. V. Yashin, A. C. Balazs, *The Journal of Chemical Physics* **2004**, *121*, 2833.
[12] G. Zhao, P. Mouroulis, *Journal of Modern Optics* **1994**, *41*, 1929
[13] V. L. Colvin, R. G. Larson, A. L. Harris, M. L. Schilling, *Journal of Applied Physics* **1997**, *81*, 5913.
[14] D. Turnbull, M. H. Cohen, *The Journal of Chemical Physics* **1970**, *52*, 3038.
[15] C. C. Bowley, G. P. Crawford, *Applied Physics Letters* **2000**, *76*, 2235.
[16] R. L. Sutherland, V. P. Tondiglia, L. V. Natarajan, T. J. Bunning, *Journal of Applied Physics* **2004**, *96*, 951.
[17] S. Meng, H. Duran, J. Hu, T. Kyu, L. V. Natarajan, V. P. Tondiglia, R. L. Sutherland, T. J. Bunning, *Macromolecules* **2007**, *40*, 3190.
[18] C. P. Lusignan, T. H. Mourey, J. C. Wilson, R. H. Colby, *Physical Review E* **1995**, *52*, 6271.
[19] P. Hiemenz, *Polymer Chemistry*, Marcel Dekker, Inc., **1984**.
[20] T. J. White, L. V. Natarajan, V. P. Tondiglia, T. J. Bunning, C. A. Guymon, *Macromolecules* **2007**, *40*, 1112.

CHAPTER 6

CONCLUSIONS

This thesis studied nanoparticle transport through the use of holographic photopolymerization for the purposes of creating sub-micron structures with defined sequestration of nanoparticles. In general, the use of this technique as a general method of nanoparticle transport remains quite promising. However, their remains still yet to be defined variability in the system that has limited the promise of the technique. For this reason, the later chapters of this thesis were devoted to system understanding in an attempt to help define the forward research in this area.

Initial efforts were undertaking to demonstrate the viability of adding nanoparticles into holographic polymer dispersed liquid crystal systems. Multi-functional acrylate-based reflection Bragg gratings were created using a 532 nm doubled YAG laser as a basis for comparison with systems containing nanoparticles. Silica nanoparticles were chosen, created by the Stöber method, because they are easily made with defined sizes, have reasonably narrow polydispersities and are a well-characterized system. Particles that were unfunctionalized, that were functionalized with alkyl chains and that were functionalized with reactive methacrylate groups were added to the system to begin to understand the effect affinities would have on nanoparticle dispersion, domain confinement, and overall morphology of the HPDLC grating structures. As was expected, the charged surface of the unfunctionalized nanoparticles led to the particles residing in the liquid crystal domain of the HPDLC. While the hydrophobic particles, both reactive and

non-reactive, primarily resided in the polymeric domain of the phase-separated structure. However, the reactive particles were much more evenly dispersed, providing evidence that they were reactively trapped in the polymer matrix and inhibited from forming agglomerates. It was noted that the optical performance to the gratings were largely unchanged from results in systems without nanoparticles, indicating that, in general, the periodic, phase separated structure was unchanged. However, switching studies and morphological studies via TEM analysis indicated that while the periodic structure was intact, the liquid crystal droplet morphology was altered to a more lamellar structure. More studies are necessary to ascertain what the primary cause of this change.

It was evident from these early experiments that the chemical nature of the nanoparticle surface is important, so considerable attention was applied to understanding the nature and quality of the coating upon the nanoparticle surface. Analysis of the Q^3 and Q^4 peaks found using solid-state ^{29}Si NMR, indicated that a significant portion of the surface hydroxyls had been reacted with siloxane coupling agent, although a quantitative degree of surface coverage could not be obtained. Further analysis of the nanoparticle surface was spurred by the discovery that particles functionalized in the presence of a large excess of MPTMS (the functionalizing agent) retained a liquid-like state upon complete removal of the alcohol solution, which varied from a waxy solid to a flowing liquid based upon increasing molarity of MPTMS in the functionalizing solution. Low-voltage TEM analysis indicated a low-density corona surrounding the nanoparticles, and solid-state NMR analysis, as evidenced by the growth of a large T^3 peak, indicates the

corona is comprised in large part by a siloxane organic hybrid structure. Small-angle X-ray scattering indicated that the waxy solid samples exhibited a packing structure that was close to FCC, which is conceivable based on the polydispersity of the bare particles as measured by optical and SAXS analysis (σ=.14). Because proton NMR analysis indicated that the relative abundance of the double bounds in the methacrylate groups remains unchanged, the corona remains reactive and capable of polymerization. Despite the fact that GPC analysis indicates that the corona is comprised of physisorbed oligomers, it is still a system which can build ordered nanoparticle structures (in the waxy solids) with the packing dimensions defined by the corona thickness which can be controlled based upon the initial molarity of the functionalizing agent in solution. Because the polymerizible corona of this structure is comprised of ~45% siloxanes, cure shrinkage would be much less drastic than would be experienced by a nanoparticle functionalized by polymer brushes. While this structured nanocomposite research is outside the scope of the holographic research, it still meets the goal of another method capable of creating macroscopic structures with controllable, sub-micron periodicities.

After the initial demonstration of feasibility of sequestering nanoparticles in the polymeric domain of holographically defined acrylate structures, the research focus of this research effort was refocused upon thiol-ene polymeric systems. This shift had already occurred for researchers focused on HPDLCs for holographic optical elements because of a multitude of advantages, which for the most part focus upon the fact that the polymerization mechanism is shifted from addition to step-growth. For the purpose of maximizing anisotropic transport of nanoparticles into a

specified domain in the holographic structure, the slower evolution of polymer molecular weight reduces viscosity and delays gelation, which should slow the decay of in the value of diffusion coefficients for the nanoparticles. MPMTS functionalized nanoparticles were again utilized for all thiol-ene experiments with the expectation that the double bond would react as and '-ene' in the polymer system. Indeed experiments demonstrated excellent dispersion and sequestration in the polymer domain at nanoparticle loadings up to 20 wt%, although liquid crystal phase separation began to decrease at high loadings.

To help understand the effect of nanoparticle loading upon polymerization kinetics, real-time infrared spectrometry was performed upon a series of thiol-ene HPDLC formulations with increasing nanoparticle loadings. Surprisingly, there was very little effect upon polymerization rate, with a slight increase at high loadings. This provides indications that the system reaction rate is not diffusion limited. However, light intensity for the RTIR experiment was one to two orders of magnitude less than used for HPDLC experiments, and utilized flood exposures, which formed PDLCs with significantly larger domains (~5x) than typically formed using holographic methods. Therefore, caution must be used when utilizing the RTIR data as a basis of explanation for HPDLC experiments. Real-time monitoring of diffraction efficiency was also utilized to determine the effect of nanoparticle addition upon the grating dynamics. These experiments exhibited a delay in grating formation that increase linearly with nanoparticle loading and is attributed to a delay in phase separation. It was then posited that this delay was either due to increased system viscosity caused by addition of the nanoparticles, or due to a

confinement effect caused by the nanoparticles that shifted the phase diagram to increase solubility.

The step-growth, holographic photopolymerizaton system was modeled using a reaction-diffusion equation. The purpose of the model was not to capture the exact physics of the system, but to rather qualitatively capture the interplay of system variables for the purposes of guiding future research direction down fruitful avenues. Initial modeling attempts focused on using a lattice model combined with Stokes-Einstein diffusion of all components based upon concentration gradients (which was chosen due to the difficulty in capturing interaction parameters between all of the system components). As this model maximized nanoparticle volume fraction in the dark region, it failed to qualitatively capture system performance. This necessitated finding a method of expressing the system free energy so that chemical potential gradients could be used in place of concentration gradients. Several simplifying assumptions were made so that the system could be based upon experimental variables. The first was that the nanoparticle, whose surface is covered in reactive functional groups, could be treated as a polymer whose radius of gyration was equal to the nanoparticle radius. Another assumption was that the liquid crystal could be treated as a solvent, which is based upon the fact that the liquid crystal intrinsic diffusion coefficient is several orders of magnitude larger than any other component. These assumptions allowed the system to be represented as a Flory-Huggins polymer-solution so that a single interaction parameter could be used. This value of χ was calculated from experimental value presented in the literature for a thiol-ene HPDLC formulation. This same

formulation exhibited a gel point at 71% conversion, which yields an approximate value of degree of polymerization of 3.5. This low value was the basis of excluding all but the first three terms in the polymer distribution. Even the system is obviously not in equilibrium; it was assumed that local equilibrium existed on the size scale of the differential element used to conduct the simulations. To account for nanoparticle reactions, the reacted nanoparticle was incorporated into the polymer volume fraction by a reaction term that scaled the same as the monomer reaction term. Internal bookkeeping in the computer code kept track of the total system volume fraction of nanoparticles so that the end results were not skewed. This model qualitatively reproduced the system performance. The model appeared to qualitatively predict the delay in phase separation evidenced in the real-time experiments in Chapter 3 (although to be clear, phase separation was not explicitly addressed in the model), based upon the reacting nanoparticle slowing down the diffusion of the polymer. Through exercising the model across a range of system variables, it became clear that two dominant parameters were the fringe visibility of the interference pattern and the non-dimensional parameter R, which is a ratio of diffusion rate to reaction rate. This indicates that the interaction between these two, not surprisingly, dominates system performance. It was also clear through the use of the system, that the parameters that maximized nanoparticle transport were not the same parameters to maximize the optical properties of the grating. The model showed very little sensitivity to nanoparticle size, which is a major limitation, and also indicates that nanoparticle transport in the model is overestimated. Inclusion of only di-mer and tri-mer terms in the diffusion equations

underestimates the system viscosity a large extent of reactions, which causes the grating structure to eventually disappear due to diffusion. Future iterations of model should include more polymer species and account for the reacted nanoparticle polymer hybrid as a separate species, and should explicitly calculate phase separation. Because of the importance of the parameter R, future research efforts in this area should focus upon methods to drive phase separation in the system by something other than polymerization.

AUTHOR'S BIOGRAPHY

John D. Busbee was born in Dallas, Texas on Aug 15, 1968 to Jerry and Martha Busbee. He moved to Tyler, TX at the tender age of 1 and lived there until he left for college. John graduated from Chapel Hill High School in 1986 and then proceeded to join the Corps of Cadets at Texas A&M. At A&M, John majored in Aerospace Engineering, where he met his wife Michelle. Graduating in 1991, John joined was commissioned as a 2nd Lieutenant in the US Air Force and moved to Wright-Patterson Air Force Base in Dayton, Ohio. While on active duty in the Air Force, John spent two years a weapons system cost analysis and financial manager before leaving to join the Air Force Research Laboratory in the Materials and Manufacturing Directorate, first as a military member, and later as government civilian. In the labs, John has worked on a wide variety of projects including CVD for ceramic matrix composites, control systems for deposition of superconductors, SWNT nucleation and growth, optical coatings and other areas with a discipline focus in non-linear control systems and spectroscopic techniques. He has served as a researcher, Research Group Leader, Team Lead, Program Manager, and Branch Chief.

John has two additional degrees: a second Bachelor's in Electical Engineering From Wright State University in Dayton and a Master in Electrical Engineering from Wright State University.

John enjoys outdoors activities such as golf and scuba diving, and is an avid runner and exercise enthusiast.